



TECHNISCHE UNIVERSITÄT
CHEMNITZ

Graphene-Based Conductor Materials: Assessment of the Electrical Conductivity

Von der Fakultät für Elektrotechnik und Informationstechnik
der Technischen Universität Chemnitz

genehmigte

Dissertation

zur Erlangung des akademischen Grades

Doktoringenieur

(Dr.-Ing.)

vorgelegt

von M.Sc. Leo Rizzi
geboren am 14.9.1991 in Solingen

Tag der Einreichung: 06.06.2021

Gutachter:

Prof. Dr. Bernhard Wunderle

Prof. Dr. Stefan E. Schulz

Prof. Dr. Christoph Tegenkamp

Tag der Verteidigung: 12.07.2021

Bibliographic description

Graphene-Based Conductor Materials: Assessment of the Electrical Conductivity

Rizzi, Leo

188 pages, 62 figures, 21 tables, 190 references

Dissertation an der Fakultät für Elektrotechnik und Informationstechnik der Technischen Universität Chemnitz, Dissertation, 2020

Abstract

In the application as conductor materials, metals such as copper or aluminum represent the state of the art. This applies for example to high-voltage lines, motor windings or the infrastructure in cities. However, metals, and especially copper, are expensive and heavy. Graphene-based conductor materials (GCMs) represent a cost-competitive and highly conductive alternative to metallic conductors. GCMs are mechanically flexible, lightweight and corrosion-resistant. But in order to fully exploit the potential of their electrical conductivity, a systematic material optimization is required.

In this thesis, the electrical conductivity of GCMs is investigated in simulations and experiments. Using a simplified model of a GCM, the theoretical maximum value of the conductivity is derived mathematically. Furthermore, the dependence of the conductivity on microscopic material parameters is quantified. For a deeper insight, finite element simulations are used to study more realistic as well as defective geometries. The meaningful modeling of physical parameters as statistical distributions requires structures with tens of thousands of graphene flakes. To this end, an efficient network model is designed and implemented. The network model is further used to compare results with the literature, to consider surface contacts and to perform an exemplary material evaluation. From the simulation results, specific guidelines for the production of highly conductive GCMs are derived.

In order to validate the simulations and to evaluate the potential of GCMs experimentally, a process chain for the preparation of graphene films is set up. Liquid graphene or graphene oxide dispersions are chosen as the starting materials, since large amounts of graphene can be processed in this way. The sizes of the graphene flakes are varied via centrifugation. Hydriodic acid is employed and evaluated as a reducing agent, as is thermal treatment. Scanning electron microscopy, Raman microscopy and an eddy current measurement of the conductivity are used for material characterization.

Two studies on the dependence of the electrical conductivity on microscopic parameters are experimentally realized. The results show good agreement with the prediction by the network model and thus support the previously established theoretical description.

Keywords

Graphene, Graphene fiber, Graphene film, Electrical conductivity, Finite elements, microstructure simulation, material optimization, structure property relations

Referat

In der Anwendung als Leitermaterialien werden nach dem Stand der Technik Metalle wie Kupfer oder Aluminium eingesetzt. Dies betrifft beispielsweise Hochspannungsleitungen, Motorwicklungen oder die Infrastruktur in Städten. Insbesondere im Fall von Kupfer handelt es sich um ein teures und schweres Material. Graphen-basierte Leitermaterialien (GCMs, engl. graphene-based conductor materials) stellen eine potentiell günstige und hoch leitfähige Alternative dar, die metallische Leiter ersetzen kann. GCMs sind mechanisch flexibel, wesentlich leichter als Metalle und korrosionsbeständig. Um das Potential ihrer elektrischen Leitfähigkeit voll auszuschöpfen bedarf es jedoch einer gezielten Materialoptimierung. In der vorliegenden Arbeit wird die elektrische Leitfähigkeit von GCMs systematisch in Simulationen und Experimenten untersucht. Mit einem vereinfachten Modell eines GCMs wird der theoretische Maximalwert der Leitfähigkeit mathematisch hergeleitet. Weiterhin wird die Abhängigkeit der Leitfähigkeit von mikroskopischen Materialparametern quantifiziert. In Finite Elemente Simulationen werden realistischere sowie defektbehaftete Geometrien betrachtet und die Erkenntnisse aus dem analytischen Modell erweitert. Die sinnvolle Modellierung von physikalischen Eingangsgrößen als statistische Verteilungen erfordert Strukturen mit mehreren Zehntausend Graphenplättchen. Zu diesem Zweck wird ein effizientes Netzwerkmodell konzeptioniert und implementiert. Mit dem Modell werden darüberhinaus Ergebnisse mit der Literatur verglichen, Oberflächenkontakte betrachtet und eine beispielhafte Materialbewertung durchgeführt. Weiterhin werden konkrete Richtlinien zur Herstellung von hochleitfähigen GCMs abgeleitet.

Um die Simulationen zu validieren und das Potential von GCMs experimentell zu bewerten, wird eine Prozesskette zur Herstellung von Graphenfilmen aufgebaut. Dabei werden flüssige Graphen- oder Graphenoxiddispersionen als Ausgangsmaterial gewählt, da in dieser Art große Mengen Graphen verarbeitet werden können. Mittels Zentrifugierung werden die Größen der Graphenplättchen variiert. Iodwasserstoffsäure wird als Reduktionsmittel eingesetzt und bewertet, ebenso wie eine thermische Materialbehandlung. Zur Materialcharakterisierung werden Rasterelektronenmikroskopie, Raman-Mikroskopie und eine Wirbelstrommessung der Leitfähigkeit eingesetzt.

Zwei Studien zur Abhängigkeit der Leitfähigkeit von mikroskopischen Parametern werden experimentell realisiert. Die Ergebnisse zeigen gute Übereinstimmung zur Vorhersage durch das Netzwerkmodell und untermauern so die zuvor beschriebenen Wirkzusammenhänge.

Schlagworte

Graphen, Graphenfaser, Graphenfilm, elektrische Leitfähigkeit, Finite Elemente, Mikrostruktursimulation, Materialoptimierung, Struktur-Eigenschafts-Beziehungen

Contents

| | |
|---|-----------|
| List of Abbreviations | 8 |
| List of Symbols | 9 |
| 1 Introduction | 13 |
| 2 Fundamentals | 17 |
| 2.1 Allotropes of carbon | 17 |
| 2.1.1 Graphene | 17 |
| 2.1.2 Graphite | 23 |
| 2.1.3 Carbon nanotubes | 24 |
| 2.2 Macro-materials based on carbon nanostructures | 25 |
| 2.2.1 Graphite Intercalation Compounds | 26 |
| 2.2.2 Thin Films | 27 |
| 2.2.3 Fibers | 29 |
| 2.2.4 Assessment of the state of the art | 32 |
| 3 Electrical conductivity modeling of graphene-based conductor materials | 35 |
| 3.1 Introduction | 35 |
| 3.2 Analytical model | 36 |
| 3.2.1 Derivation | 36 |
| 3.2.2 Results and discussion | 38 |
| 3.2.3 Extension of the analytical model | 42 |
| 3.2.4 Summary | 43 |
| 3.3 Finite element analysis | 44 |
| 3.3.1 Introduction to the method | 44 |
| 3.3.2 Geometry Generation | 45 |
| 3.3.3 Mathematical formulation of the problem | 48 |
| 3.3.4 Results and discussion | 49 |
| 3.3.5 Computational challenges when modeling GCMs | 57 |

| | |
|---|------------|
| 3.3.6 Summary | 61 |
| 3.4 3D random resistor network model | 62 |
| 3.4.1 A simulation method optimized for GCMs | 62 |
| 3.4.2 Preliminary considerations | 63 |
| 3.4.3 Detailed description of the simulation method | 65 |
| 3.4.4 Results and discussion | 74 |
| 3.4.5 Top contacts | 85 |
| 3.4.6 Evaluating raw materials for GCMs | 91 |
| 3.4.7 Implications for the production of GCMs | 93 |
| 3.4.8 Summary | 96 |
| 4 Preparation and analysis of graphene-based thin films | 99 |
| 4.1 Introduction | 99 |
| 4.2 Preparation of graphene films | 100 |
| 4.2.1 Pre-treatment | 100 |
| 4.2.2 Centrifugation | 101 |
| 4.2.3 Deposition | 104 |
| 4.2.4 Post-Treatment | 107 |
| 4.3 Characterization | 113 |
| 4.3.1 Structural characterization | 113 |
| 4.3.2 Electrical characterization | 116 |
| 4.4 Comparison with the simulation | 124 |
| 5 Conclusion and Outlook | 129 |
| 5.1 Conclusion | 129 |
| 5.2 Outlook | 132 |
| 6 Appendix | 135 |
| 6.1 Convergence tests of the network simulation | 135 |
| 6.2 Different flake size distributions compared in section 3.4.4.1 . . . | 138 |
| 6.3 COMSOL Multiphysics® settings | 139 |
| 6.4 Derivation of the analytical expression for the resistance mea- surement with top contacts | 140 |
| 6.5 Graphene and GO dispersions | 143 |
| 6.6 Fitting parameters from the comparison of experiment and sim- ulation | 144 |
| 6.7 Process parameters for the preparation of graphene and GO films | 144 |
| 6.7.1 Standard procedures | 144 |
| 6.7.2 Preparation protocols | 146 |
| Bibliography | 152 |

| | |
|----------------------|-----|
| List of Figures | 175 |
| List of Tables | 177 |
| Versicherung | 179 |
| Theses | 181 |
| Curriculum vitae | 183 |
| List of publications | 185 |
| Danksagung | 187 |

List of abbreviations

| | |
|-------|---------------------------------------|
| 1D | one-dimensional |
| 2D | two-dimensional |
| 3D | three-dimensional |
| AC | alternating current |
| BP | buckypaper |
| CF | carbon fiber |
| CNT | carbon nanotube |
| CVD | chemical vapor deposition |
| DC | direct current |
| DI | deionized |
| EMA | effective medium approximation |
| FEA | finite element analysis |
| FEM | finite element method |
| GCM | graphene-based conductor material |
| GIC | graphite intercalation compound |
| GO | graphene oxide |
| HI | hydriodic acid |
| HOPG | highly oriented pyrolytic graphite |
| IPA | isopropyl alcohol |
| LC | liquid crystal |
| MCE | mixed cellulose ester |
| MD | molecular dynamics |
| PAN | polyacrylonitrile |
| PES | polyether sulfone |
| PTFE | polytetrafluoroethylene |
| SD | sediment |
| SN | supernatant |
| SEM | scanning electron microscopy |
| T-BLG | twisted bilayer graphene |
| TCR | temperature coefficient of resistance |

List of symbols

| | |
|---|---|
| a | graphene nearest-neighbor distance |
| a^* | graphene lattice constant |
| $\mathbf{a}_1, \mathbf{a}_2$ | graphene unit cell vectors |
| A | average graphene flake area |
| A_{flake} | individual graphene flake area |
| A_x, A_y, A_z | conductor cross-sectional area in x -, y -, z -direction |
| $A_{\text{in}}, A_{\text{out}}$ | in-plane, out-of-plane cross-sectional area |
| $\bar{A}_{\text{in}}, \bar{A}_{\text{out}}$ | effective in-plane, out-of-plane cross-sectional area |
| A_{ch} | channel cross-sectional area in the analytical model |
| A_{tot} | total cross-sectional area of a GCM |
| \AA | 1 Angstrom, $1 \text{\AA} = 10^{-10} \text{ m}$ |
| b | non-ideality factor for the analytical model |
| b_1, b_2 | baseline lengths of a trapezoidal resistor |
| $\mathbf{C}_{M,N}$ | CNT chiral vector |
| d | voltage probe distance in the network model |
| eV | electron volt, $1 \text{ eV} \approx 1.602 \cdot 10^{-19} \text{ J}$ |
| $E(k_x, k_y)$ | energy dispersion relation |
| f | flake size scaling factor |
| f_r | rotational speed |
| g | gravitational acceleration ($\approx 9.81 \text{ ms}^{-2}$) |
| G_{ch} | single channel conductance in the analytical model |
| (G_{ij}) | conductance matrix |
| $G_{\text{in}}, G_{\text{out}}$ | in-plane, out-of-plane conductance |
| G_{norm} | normalized conductance between two overlaps |
| G_{trap} | conductance of a trapezoidal resistor |
| γ_0 | carbon-carbon hopping parameter ($\approx 2.8 \text{ eV}$) |
| \hbar | reduced Planck constant ($\approx 1.05 \cdot 10^{-34} \text{ Js}$) |
| I | electric current |
| $I_{(x,y)}, I_z$ | current in (x, y) -direction, z -direction |
| I_{tot} | total current through a GCM |
| $I(X)$ | integrated intensity of the Raman X peak with $X \in \{D, G, S_{2D}, S_{3DA}, S_{3DB}\}$ |
| j | integrated and normalized current density |
| \mathbf{J} | current density vector |
| k | empirical parameter in the network model |
| $\mathbf{k} = (k_x, k_y)$ | electron wave vector in graphene |
| l | sample length |
| $l_{\text{in}}, l_{\text{out}}$ | in-plane, out-of-plane length |

| | |
|---|--|
| $\bar{l}_{\text{in}}, \bar{l}_{\text{out}}$ | effective in-plane, out-of-plane length |
| l_{tot} | total length of a GCM |
| l_x, l_y, l_z | conductor length in x -, y -, z -direction |
| L_D | mean distance between defects |
| λ | Raman laser wavelength |
| n | GIC staging |
| N | number of channels in the analytical model |
| \mathcal{O} | algorithm growth rate |
| p | packing density |
| Φ | electric potential |
| rpm | 1 revolution per minute |
| r_{eff} | universal effective resistance |
| R | four-point probe resistance |
| R^* | share of turbostratic stacking |
| R_{2D}, R_{3D} | four-point probe resistance in the 2D, 3D limit |
| R_{ch} | single channel resistance in the analytical model |
| $R_i^{\text{in}}, R_j^{\text{out}}$ | in-plane, out-of-plane resistance |
| $\bar{R}_{\text{in}}, \bar{R}_{\text{out}}$ | effective in-plane, out-of-plane resistance |
| R_{sq} | sheet resistance |
| RCF | relative centrifugal force |
| s | equidistant probe spacing of four-point probes |
| $s_{\text{in}}, s_{\text{out}}$ | standard deviation of the in-plane, out-of-plane conductivity |
| S | 1 Siemens, $1 \text{ S} = 1/\Omega$ |
| σ_{hi} | conductivity of the high-conductivity phase |
| $\sigma_{\text{in}}, \sigma_{\text{out}}$ | graphene flake in-plane, out-of-plane conductivity |
| $\bar{\sigma}_{\text{in}}, \bar{\sigma}_{\text{out}}$ | average in-plane, out-of-plane conductivity |
| $\sigma_{\text{min}}, \sigma_{\text{max}}$ | minimum, maximum conductivity of a GCM |
| σ_{tot} | total conductivity of a GCM |
| $\sigma_x, \sigma_y, \sigma_z$ | conductivity in x -, y -, z -direction |
| $\boldsymbol{\sigma}$ | conductivity tensor |
| t | thickness of a GCM |
| t_c | critical exponent |
| t_{gr} | average graphene flake thickness |
| $\mathbf{T}_{M',N'}$ | perpendicular vector along CNT axis |
| θ | share of non-conducting flakes in a GCM |
| θ_c | critical share of non-conducting flakes in a GCM |
| θ_{hi} | share of the high-conductivity phase |
| u | 1 unified atomic mass unit, $1 \text{ u} \approx 1.66 \cdot 10^{-27} \text{ kg}$ |
| v_F | Fermi velocity |

| | |
|-----------------|---------------------------------------|
| V | potential difference |
| w | width of a GCM |
| w_{ch} | channel width in the analytical model |

1 Introduction

In 2004 Andre Geim and Konstantin Novoselov discovered graphene, world's first two-dimensional (2D) material [1]. It is a monolayer of carbon atoms arranged in a honeycomb lattice and features impressive properties. Graphene is strong, corrosion-resistant, virtually transparent to light, and more conductive than any metal [2]. Additionally, graphene is able to transport enormous amounts of current without being damaged. It is robust to electromigration and retains its high conductivity at elevated temperatures [3, 4]. The discovery of graphene, once considered too unstable to exist [5, 6, 7], established a completely new field of research. The newly gained access to a 2D material, furthermore with such exceptional properties triggered a veritable “gold rush” mood in the scientific community [2]. For fundamental research, graphene provided access to phenomena previously known only in theory. For engineers, graphene promised an abundance of exceptional inventions. The popularity of graphene grew even further when Geim and Novoselov received the Nobel Prize in Physics in 2010 for their work on the material.

Especially in the years directly after the discovery of graphene, research was heavily focused on studying and exploiting its properties on the nanoscale. Graphene's ultimate thickness and its extraordinary electronic properties had quickly fueled hopes for an ultrafast and ultrasmall transistor that could revolutionize information technology [8]. However, opening a sufficiently large bandgap in graphene without sacrificing the favorable material properties turned out to be difficult. Efficiently integrating graphene into conventional transistor concepts proved to be equally challenging [8]. And although processing technology has evolved considerably since 2004, no competitive graphene transistor has yet been presented, let alone a concept for its mass production.

While there are many other micro- or nanoscopic graphene applications such as various types of sensors [9], more and more macroscopic applications are being developed as well. To name a few, graphene-based batteries [10], heat spreaders [11], or electric wires [12] are all based on macroscopic assemblies of graphene nanosheets. Furthermore, they cater to fast growing industrial

sectors. Batteries are vital to mobile electronics as well as for energy storage in electric cars. Heat spreaders dissipate heat in devices where increasingly fast circuits are operating. And electric wires are omnipresent in a multitude of sectors.

For most wiring applications, copper is the state of the art material. It is highly electrically and thermally conductive, combines a great tensile strength with a high ductility, exhibits a small coefficient of thermal expansion, and is rather resistant to creep. Copper is employed as the main conductor material in electrical machines, in power transmission and distribution, or in data cables in telecommunications. However, with a density of 8.96 gcm^{-3} and a price of 6165 USD per ton¹, copper is heavy and expensive. In the course of the electrification in the automotive industry, there is an increased demand for electrical machines so that alternatives to copper wiring become more and more relevant. Graphene-based conductor materials (GCMs) such as fibers or ribbons might evolve into such an alternative to copper.

GCMs try to transfer graphene’s extraordinary electronic properties to the macroscopic scale, with the ultimate goal of a highly conductive, ultralight and strong conductor. Currently, the bottleneck for the application of GCMs is the electrical conductivity. While it has increased from 0.025 MSm^{-1} in 2011 [12] to 17.3 MSm^{-1} in 2019 [13], it still remains below copper or aluminum (59 MSm^{-1} and 38 MSm^{-1} respectively [14, 15]). Several research groups are actively working on the experimental realization of an improved electrical conductivity, but little to no theoretical descriptions or modeling methods have been presented. Yet, simulations and theoretical descriptions are essential for the optimization process. They contribute to building knowledge and understanding while also restricting the parameter space that needs to be investigated experimentally. Simulations can save time and cost, and allow for the modeling of scenarios that are not accessible in experiments. This thesis is dedicated to the optimization of the electrical conductivity of GCMs using a simulative and an experimental approach. With the help of extensive simulations, the decisive material parameters for electrical conduction are identified, and the limit of the electrical conductivity is evaluated. In experimental studies, the simulation is validated, and the feasibility of a large-scale production is assessed. The outline of the thesis is as follows:

Chapter 2: Fundamentals

An introduction to the most important carbon allotropes for this work is given. Graphene, graphite and carbon nanotubes are presented in terms of

¹Average price at the London Metal Exchange in 2019

atomic and electronic structure, production methods, and applications. Subsequently, macro-materials based on carbon nanomaterials are introduced and the state of the art is assessed.

Chapter 3: Electrical conductivity modeling of graphene-based conductor materials

The electrical conductivity of GCMs is modeled with different methods. The first and most basic approach is an analytical description of a simplified model structure. Complexity increases in the second step, where finite element simulations are carried through. Finally, a simulation method based on a random resistor network optimized for large numbers of graphene flakes is proposed. The different methods are used to characterize GCMs in detail. The impact of the microscopic material properties on the macroscopic electrical conductivity is studied and the conductivity limit is identified. In the course of this chapter, the methods are continuously compared to each other and their strengths and weaknesses are discussed. As the most suitable approach, the network simulation method is applied to realistic scenarios. Experimental results from the literature are reproduced, top contact configurations are studied, and guidelines for the production of highly conductive GCMs are deduced.

Chapter 4: Preparation and analysis of graphene-based thin films

The theoretical description from chapter 3 is validated by fabricating and measuring graphene-based thin films. To this end, a process chain suitable for a potential upscaling is set up. Graphene is processed in the form of a dispersion, and several commercial products are tested and compared. Relevant characterization methods are identified and the results are compared to the state of the art in the literature.

Chapter 5: Conclusion and outlook

The findings of this thesis are summarized and the potential of GCMs as a material class is discussed. Follow-up activities to address remaining weak points are suggested.

2 Fundamentals

2.1 Allotropes of carbon

Carbon is one of the most abundant elements on Earth. It naturally occurs in its pure elemental form as well as in millions of stable chemical compounds. Carbon is the basis of organic chemistry and a common element of all known forms of life. It is found in Earth’s atmosphere as CO_2 and it is mined in the form of coal. Carbon can covalently bond with itself, and its ability to form several hybrid orbitals leads to a variety of allotropes such as diamond, graphite, graphene, carbon nanotubes, or fullerenes. The physical properties of these allotropes vary greatly among themselves, and they have different fields of application. In the following sections, graphene, graphite and carbon nanotubes are presented in detail since they represent the starting materials for the production of GCMs. As the fundamental building block of these three allotropes, graphene is presented first.

2.1.1 Graphene

Graphene is a monolayer of carbon atoms arranged in a honeycomb lattice. It is world’s first truly 2D material and was fabricated by Geim and Novoselov in 2004 [1]. They used a simple scotch tape to exfoliate single layers of graphene from thin graphite crystals. In 2010, they were awarded the Nobel Prize in Physics for their experimental work on graphene. Due to its extraordinary set of properties such as high mechanical strength and excellent electrical and thermal conductivity [2], graphene was quickly hailed as the next disruptive technology [16]. Fifteen years after its discovery, an abundance of novel physical phenomena have been reported [2], and the first large-scale applications are emerging (e.g. Samsung’s graphene-enhanced battery [10] in 2017, or Huawei’s graphene-based heat spreader in 2018 [11]). With increasingly industrialized production methods, large amounts of high-quality graphene become more and more accessible [17, 18], and scientists and engineers are constantly searching for the next major application.

2.1.1.1 Crystal structure

As the first element of the fourth main group, carbon has got four valence electrons in the $2s^2 2p^2$ configuration. In graphene, three of these form covalent bonds in sp^2 -hybridized orbitals. They are symmetrically aligned in the graphene plane, creating 120° angles between them. Consequently, the carbon atoms condense in a honeycomb lattice, which is equivalent to the union of two triangular sub-lattices A and B. Therefore, the unit cell of the graphene lattice contains two atoms separated by a distance of $a = 1.42 \text{ \AA}$ while the lattice constant is $a^* = 2.46 \text{ \AA}$. In reciprocal space, the lattice is hexagonal, which means that the first Brillouin zone is a hexagon as well. Its most important characteristic points are the high symmetry point Γ and the inequivalent points \mathbf{K} and \mathbf{K}' at the Brillouin zone corners. Figure 2.1.1 shows the graphene lattice in real space and in reciprocal space.

The geometric structure and the strong covalent bonds in graphene lead to exceptional physical properties. Graphene features a tensile strength of 130 GPa and a Young's Modulus (stiffness) of 1 TPa at a density of only 0.77 mgm^{-2} [19, 4].

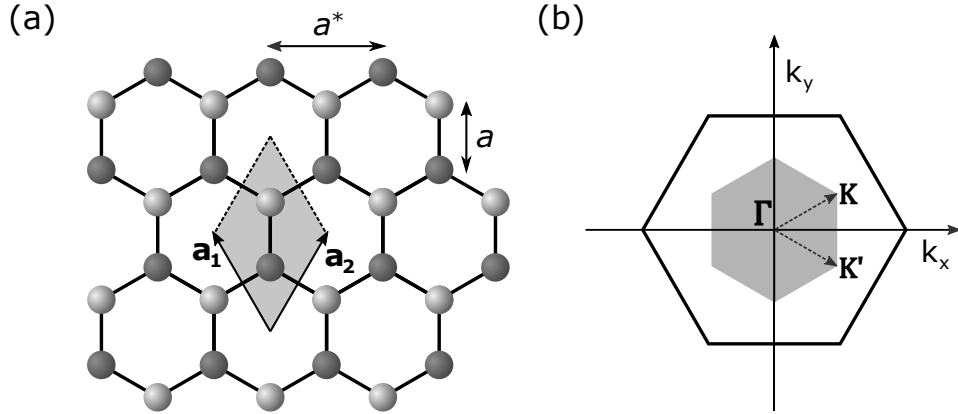


Figure 2.1.1: (a) Graphene structure in real space. The two sub-lattices A and B are distinguished by color. The shaded area is the unit cell, spanned by the unit cell vectors \mathbf{a}_1 and \mathbf{a}_2 . (b) Graphene structure in reciprocal space with the high symmetry point Γ in the center, and the characteristic points \mathbf{K} and \mathbf{K}' . The shaded area corresponds to the first Brillouin zone.

2.1.1.2 Electronic Structure

In graphene, the three electrons per atom required for the in-plane bonds are tightly bound and cannot contribute to electronic transport. The remaining electron occupies the p_z -orbital perpendicular to the graphene plane. In neighboring atoms, the p_z -orbitals overlap such that the so-called π -bands

emerge, where electrons are delocalized and free to move along the graphene plane. The corresponding dispersion relation can be computed within the tight-binding model considering nearest-neighbor interaction

$$E_{\pm}(k_x, k_y) = \pm\gamma_0 \sqrt{1 + 4 \cos\left(\frac{3}{2}k_x a\right) \cos\left(\frac{\sqrt{3}}{2}k_y a\right) + 4 \cos^2\left(\frac{\sqrt{3}}{2}k_y a\right)} \quad (2.1.1)$$

with the hopping parameter $\gamma_0 \approx 2.8 \text{ eV}$ and the electron wave vector $\mathbf{k} = (k_x, k_y)$. E_+ and E_- correspond to the conduction and the valence band energies respectively. At the points

$$\mathbf{K} = \frac{2\pi}{a} \left(\frac{1}{3}, \frac{1}{3\sqrt{3}} \right) \text{ and } \mathbf{K}' = \frac{2\pi}{a} \left(\frac{1}{3}, -\frac{1}{3\sqrt{3}} \right), \quad (2.1.2)$$

the conduction and the valence band meet, which makes graphene a zero-gap semiconductor. A visualization of the band structure and a close-up of the zero-gap is shown in Figure 2.1.2. In a perfect graphene lattice, E_F is located exactly in between the conduction and the valence band. Thus, equations (2.1.2) define the regime that is relevant for electronic transport. A first order Taylor expansion of equation (2.1.1) about the \mathbf{K} point yields the linear dispersion relation

$$E_{\pm}(k_x, k_y) = \pm\hbar v_F |\mathbf{k}'| \quad (2.1.3)$$

where $\mathbf{k}' = \mathbf{k} - \mathbf{K}$, \hbar is the reduced planck constant, and $v_F \approx 3\gamma_0 a (2\hbar)^{-1} \approx 10^6 \text{ ms}^{-1}$ the Fermi velocity in graphene. In the range of validity of this approximation, charge carriers are described by the Dirac equation for massless relativistic particles rather than by the Schrödinger equation. As a consequence, relativistic phenomena such as Klein tunneling become accesible in condensed-matter experiments [20]. More details on the electronic properties of graphene are discussed in Castro Neto's extensive review [21].

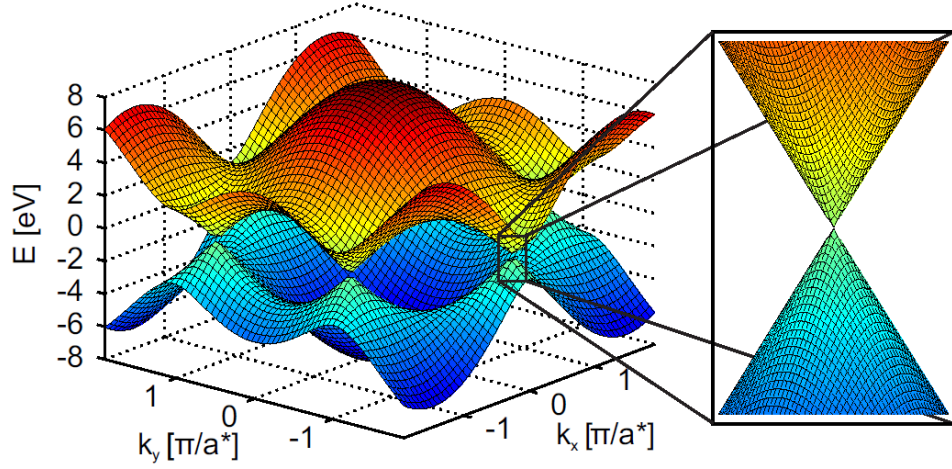


Figure 2.1.2: Electronic band structure of graphene with a close-up of the zero-gap.

Graphene exhibits a remarkably high carrier mobility. At a carrier density of 10^{12} cm^{-2} and at room temperature, the mobility is theoretically limited to $200000 \text{ cm}^2 \text{ V}^{-1} \text{ s}^{-1}$, which translates to a record-high electrical conductivity of 100 MSm^{-1} [22, 23]. For comparison, the most conductive metals are silver and copper with conductivities of 62 MSm^{-1} and 59 MSm^{-1} respectively [14].

2.1.1.3 Stacked layers of graphene

When individual layers of graphene are stacked, the physical properties change with every added layer, until the material is indistinguishable from a thin film of graphite [24]. During this evolution, the way of stacking plays an important role. If graphene layers are shifted with respect to each other, they can remain largely decoupled and behave similar to individual graphene layers [25]. When there is a relative twist between two layers, the behavior also changes. For small angles, superlattices form and new physical phenomena occur such as the recently observed superconductivity at twisting angles of 1.1° [26]. For larger angles, the layers decouple again and exhibit monolayer characteristics [27]. The energetically most stable form of stacking however, is AB-stacking, where the atoms of sub-lattice A in the upper sheet are positioned directly above the atoms of sub-lattice B of the lower sheet (Figure 2.1.3 (c)). In AB-stacked multilayers, the electrical conductivity decreases with increasing layer number [28, 29].

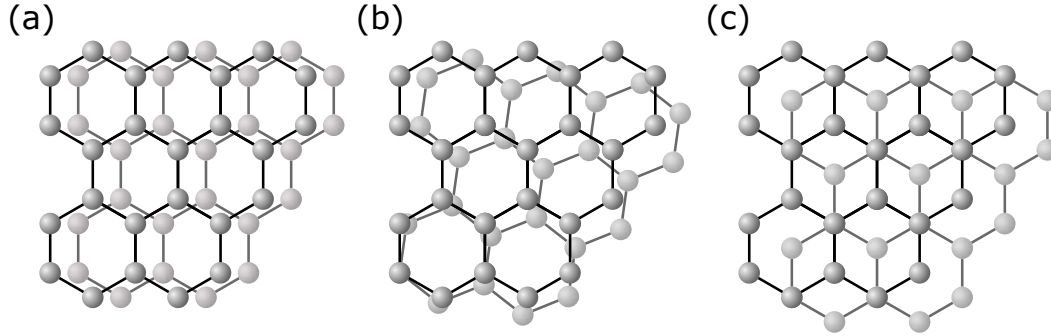


Figure 2.1.3: (a) Shifted, (b) twisted, and (c) AB-stacked stacked graphene layers.

Despite their extremely small thickness, stacked graphene layers are not strictly 2D anymore. In AB-stacking, layers are separated by the van-der-Waals distance of 0.335 nm. As soon as more than one layer is present, it is possible to distinguish between in-plane and out-of-plane properties. Stacked graphene layers exhibit anisotropic properties in many areas, independent of the layer number. Mechanically, the weak van-der-Waals forces which hold the individual monolayers together are orders of magnitude smaller than the strong covalent in-plane bonds. The out-of-plane electrical conductivity is far smaller than the in-plane conductivity [30], and the same holds true for the thermal conductivity [31, 32]. The word “graphene” is usually reserved for monolayers, two stacked layers are referred to as “bilayer graphene” and 3-10 layer correspond to “few-layer” or “multilayer graphene”. For layer stacks with 10 or more layers, the material can essentially be regarded as a thin piece of graphite [2]. In this work, the term “graphene” is used whenever mono-, bi-, or few-layer graphene are interchangeable. When the number of layers is decisive, it is specified precisely.

2.1.1.4 Production of graphene

The original method that led to the discovery of graphene, where monolayer flakes are manually exfoliated from graphite flakes with a scotch tape, is not scalable for mass production. The obtained flakes are of the highest quality [16], but the process is slow and inefficient.

A common alternative that yields large monolayer graphene crystals is chemical vapor deposition (CVD). In this method, a gaseous precursor decomposes at the surface of a substrate such that a solid material is deposited. The required energy for the reaction is supplied by e.g. directly heating the substrate or igniting a plasma in the reaction chamber. For graphene, methane is a common precursor gas, and deposition temperatures are in the range of

1000°C [33].

CVD is a reliable production method that guarantees high quality monolayers on a substrate. It has been refined to a stage where room temperature carrier mobilities $>50000\text{ cm}^2\text{V}^{-1}\text{s}^{-1}$ can be reproducibly obtained [33]. However, CVD still requires the transfer of graphene from the growth substrate onto the intended final location. So far, a precise, residue-free transfer that is scalable for mass production has not been established.

CVD is mainly of interest for micro- and nanoelectronics, exploiting the small thickness of graphene, its high carrier mobility, or its transmittance of light [33, 34]. For macro-materials with a high graphene content however, the method is not suitable.

An approach to obtain tons of graphene is liquid-based processing, where graphite or graphite oxide is exfoliated in a liquid environment [35, 36]. Such processes yield graphene or graphene oxide (GO) suspended in a dispersion medium and ready for further processing. Depending on the concentration of the dispersion, i.e. how much graphene or GO is suspended in which volume of the dispersion medium, large quantities can be processed efficiently.

In the originally proposed liquid phase exfoliation, pure graphite is dispersed in an organic solvent and exfoliated via sonication [17]. The same group later reported on high-shear mixing of graphite flakes for a higher yield at a lower input energy [37]. Another liquid exfoliation technique is based on an electrochemical approach. Two electrodes, one or both made of graphite, are placed inside a liquid electrolyte, and a current is driven through the system. At the graphite electrode, ions are intercalated between the graphite layers, which leads to structural expansion and ultimately the exfoliation of graphene flakes [38]. Recently, an efficient and non-destructive exfoliation of intercalated graphite with microwaves has been reported [39]. All of the liquid-based graphite exfoliation processes share the advantage of high-quality flakes, high yields, and solution processability at low cost. Drawbacks are the limited flake size and the low share of monolayers [36]. Commercially available graphene dispersions contain flakes with an average diameter of several micrometers (see Appendix 6.5). The products are often water-based, which is beneficial for the processability but limits the stability of the dispersions. The hydrophobic graphene flakes tend to agglomerate over time, reducing the overall monolayer share.

The second major route to produce large amounts of graphene dispersion is via synthesis and reduction of GO. In this method and its variants, graphite is first oxidized and then exfoliated in an aqueous solution [16]. The oxygen groups increase the spacing of the graphite layers and thus facilitate the subsequent exfoliation process. In an aqueous solution, the exfoliated GO sheets exhibit excellent stability due to their hydrophilic nature [40, 41]. Similar

to the graphite-based processes, the GO-based approach offers high yields and solution processability. Additionally, the flake sizes are larger by more than an order of magnitude. Commercial GO-dispersions with average flake diameters of several tens of micrometers are readily available (see Appendix 6.5). The downside is the need for reduction, either in the dispersion or after processing into the final product. GO is insulating, and only complete reduction in combination with defect healing can restore the electrical properties to the level of pristine graphene. Several graphene production methods are presented in Novoselov’s “roadmap for graphene” [16] and references therein. Reference [42] is a more recent review article with a focus on mass production.

2.1.2 Graphite

Graphite is one of the naturally abundant allotropes of elemental carbon. It represents the thermodynamically most stable carbon configuration and occurs worldwide. Graphite is composed of stacked graphene layers held together by van-der-Waals forces. There are several naturally occurring stacking orders, with the most common ones depicted in Figure 2.1.4. Graphite is highly relevant for industrial purposes, with a world-wide annual mining volume of natural graphite between 894000 and 1201000 tons in the years 2014 - 2018 [43]. It is mostly used for refractory applications, batteries, steel-making, or lubricants [43].

Compared to bi- or few-layer graphene, graphite exhibits a higher out-of-plane electrical conductivity [44], but a significantly lower in-plane conductivity [28], making it a worse conductor overall.

Apart from mining natural graphite, high quality synthetic graphite can be produced via pyrolysis. Under the exclusion of air, amorphous carbon is converted to crystalline graphite by heating to temperatures approaching 3000°C. If additional tensile stress in the in-plane direction is applied, highly

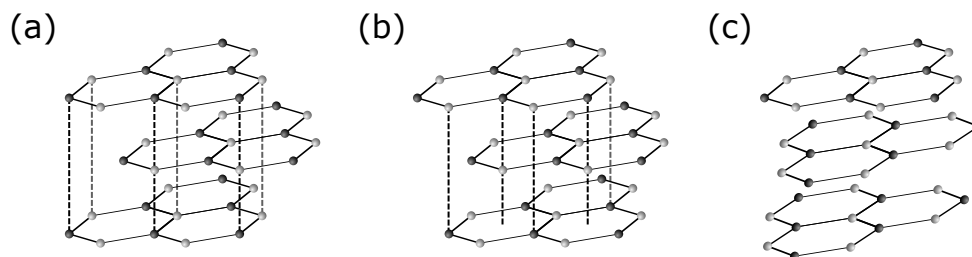


Figure 2.1.4: Different stacking sequences in graphite: (a) AB, (b) ABC, and (c) turbostratic stacking, where basal planes are parallel but layers have lost atomic alignment. Combinations of stacking orders are possible as well. Atoms of the different sub-lattices are distinguished by color.

oriented pyrolytic graphite (HOPG), the purest and most well-ordered form of synthetic graphite, is obtained [45]. With an electrical conductivity of 2.5 MSm^{-1} [46], HOPG is the most conductive form of graphite.

2.1.3 Carbon nanotubes

A carbon nanotube (CNT) can be regarded as a rolled-up sheet of graphene, making it a quasi one-dimensional (1D) object. The geometrical structure of a CNT is defined by the chiral vector of the corresponding graphene sheet $\mathbf{C}_{M,N} = M\mathbf{a}_1 + N\mathbf{a}_2$ with integer M and N (Figure 2.1.5 (a)). When the sheet is rolled-up, the chiral vector corresponds to the CNT circumference and thus defines its radius. The unit cell of a CNT is defined by $\mathbf{C}_{M,N}$ and the perpendicular vector along the tube axis $\mathbf{T}_{M',N'} = M'\mathbf{a}_1 + N'\mathbf{a}_2$ with integer M' and N' . $\mathbf{T}_{M',N'}$ is the smallest vector satisfying $\mathbf{C}_{M,N} \cdot \mathbf{T}_{M',N'} = 0$. In CNTs with $M = N$, the chiral vector runs along an edge that looks similar to an armchair, which is why these CNTs are also called armchair CNTs. Correspondingly for $N = 0$, CNTs are referred to as zigzag CNTs. The rest of the CNTs are classified as chiral. The construction of a CNT and the three chiralities are shown in Figure 2.1.5 (a).

CNTs do not only vary in terms of chirality, they can also exhibit a variable number of layers in the form of nested tubes as shown in Figure 2.1.5 (b). This leads to the distinction between single-wall, double-wall, or multi-wall CNTs respectively. Depending on the chirality and the number of walls, CNTs exhibit different properties [47, 48]. In general, approximately one third of possible CNTs is metallic and exhibits excellent electrical conductivity as well as current-carrying capacity. The other portion of the CNTs is semiconducting [49].

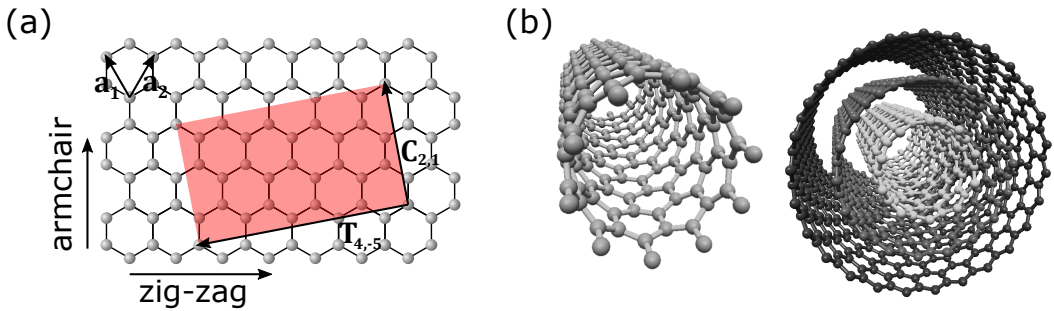


Figure 2.1.5: (a) Graphene sheet with the exemplary unit cell of the chiral (2,1)-CNT (red). The chiral vector $\mathbf{C}_{2,1}$, the perpendicular vector $\mathbf{T}_{4,-5}$, and the graphene lattice vectors \mathbf{a}_1 , \mathbf{a}_2 are indicated. The top and bottom edges of the graphene sheet are zig-zag edges, the left and right side are armchair edges. (b) Single- and multi-wall CNT.

The first multi-wall CNTs produced by Ijima were obtained in an arc discharge between graphite electrodes [50]. Although the production was accidental and only resulted in small amounts of CNTs, the method was quickly scaled-up [51]. In 1995, Smalley’s group reported on a laser ablation method to synthesize single-wall CNTs. They vaporized transition-metal/graphite composites with laser pulses, achieving high purities and a high yield [52]. Another very common production method of CNTs is CVD. Similar to the growth of graphene, a carbonaceous precursor gas is exposed to a substrate, commonly at temperatures of several hundred °C. The precursor reacts with the substrate such that carbon is deposited and CNTs start to grow. By utilizing suitable catalyst particles, the type of the grown CNTs can be tuned [53, 54]. Several production methods and their recent advances are presented in Reference [55].

Despite the variety of approaches, the type-selective production of CNTs on a large scale is still a heavily researched topic [56]. Although the majority of research groups work on the selective production of semiconducting CNTs for sensors and electronics [57, 58], metallic CNTs form the basis for conductor materials [47]. If they can not be selectively grown, it is possible to separate CNTs after the actual production, for example via centrifugation [59]. However, considering a large-scale production, this creates an enormous overhead and makes the production process highly inefficient.

Due to the remaining difficulties in producing metallic CNTs at low-cost, graphene currently appears to be better suited for macroscopic conductor applications. However, the research field is still evolving rapidly and further progress should be expected.

2.2 Macro-materials based on carbon nanostructures

In an effort to transfer the extraordinary properties of graphene or CNTs to the macroscale, various derived materials have been synthesized. This section introduces the macro-materials that are well-suited for electrical conduction. As a related and structurally similar material class, graphite intercalation compounds are presented. Porous materials such as foams or aerogels perform well in energy-storage applications [60, 10], but are less relevant as electrical conductors. The amount of current-carrying material per volume is insufficient for high-performance electrical conduction. Apart from their general structure and physical properties, important literature on carbon nanostructured macro-materials is reviewed, and the state of the art is reported.

2.2.1 Graphite Intercalation Compounds

Graphite intercalation compounds (GICs) are created by inserting non-carbon chemical species between the layers of a graphite crystal. The inserted species is called intercalant, while graphite represents the host material. The material system has been studied systematically since the 1930s, with particularly relevant results in the 1970s and 1980s. The comprehensive review by Mildred and Gene Dresselhaus [46] provides a detailed summary of theoretical and experimental findings.

GICs retain the anisotropic layered structure of graphite where in-plane binding forces are generally much stronger than out-of-plane binding forces. GICs are classified according to the intercalant and the so-called staging n . The staging phenomenon describes the periodic arrangement of intercalant layers separated by a fixed number n of graphite layers. An example is shown in Figure 2.2.1. Material properties vary heavily depending on both the intercalated species as well as the staging, i.e. a stage-1 GIC might behave differently from a stage-3 GIC with the same intercalant. Due to the intercalation, the interlayer spacing is increased, decoupling the individual graphite layers. The intercalant also acts as a dopant. It provides charge carriers to the host, without damaging the honeycomb carbon lattice. The most significant effect of intercalating foreign species into graphite is the boost in electrical conductivity. In 1977, Vogel et al. presented AsF_5 - and SbF_5 -GICs with in-plane conductivities of 63 MSm^{-1} [61] and $>80 \text{ MSm}^{-1}$ [62] respectively. In 1986, Shioya et al. measured in-plane conductivities of 90 MSm^{-1} in AsF_5 -intercalated graphite, and also transferred the concept to carbon fibers, where they reproducibly obtained 10 MSm^{-1} [63]. The enormous in-plane conductivity is often linked to an out-of-plane conductivity that is lower than in graphite. Anisotropy ratios of 10^6 have been reported [64]. It was found

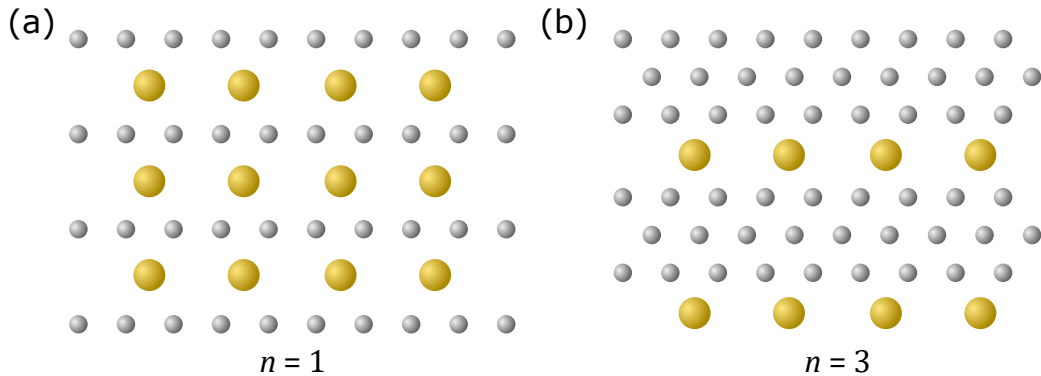


Figure 2.2.1: (a) Stage-1 GIC and (b) Stage-3 GIC. Grey balls represent carbon atoms, yellow balls represent the intercalant.

that donor-type intercalants commonly benefit the out-of-plane conductivity, while acceptor-type intercalants are detrimental to it [46].

The temperature-dependence of the electrical conductivity of GICs is similar to metals. The availability of charge carriers is largely temperature-independent, while electron-phonon scattering increases with temperature. Thus, the overall temperature coefficient of resistance (TCR) is positive around room temperature [46].

When GICs were first studied, graphene had not yet been discovered. From today's point of view however, GICs can be interpreted as stacked graphene layers, which are separated and potentially decoupled by the intercalants. This type of material is highly relevant for GCMs as it is structurally similar and thoroughly studied. Furthermore, it has been shown that in-plane conductivities in GICs can exceed copper, which also reveals the great potential of GCMs. GICs are a helpful starting point when dopants in GCMs are assessed, since for most GICs, the physical properties are well-known. Their densities, staging variations, thermal and electrical conductivities, and stability in air have often been reported by different groups. GICs are particularly relevant for graphene films, where the staging phenomenon has been reported as well [65].

2.2.2 Thin Films

Graphene films are assemblies of graphene flakes, which are stacked on top of each other to form a dense macroscopic material. In the literature, they are also referred to as "graphene paper" or "graphene foil". In 2007, Ruoff's group synthesized the first free-standing GO films [66] by vacuum filtration of a GO dispersion. Shortly thereafter, many research groups adapted the idea and reported on reduced GO or graphene films with thicknesses between 1 nm and 10 μm [67, 68, 69, 70]. Since then, the processes have been continuously improved and graphene films have become more and more performant. They exhibit an outstanding combination of properties such as a record-high thermal conductivity [71], a steadily growing electrical conductivity [65], high mechanical strength [69], flexibility [65], corrosion-resistance [13], and a low weight [72].

Graphene films are structurally similar to turbostratic graphite. They consist of individual graphene sheets, which are largely stacked without order or orientation. However, the individual layers overlap and interlock to create a unique structure that is both flexible and strong. They can be bent and folded repeatedly without affecting their physical properties [73]. Mechanical flexibility is one of the key features that separates graphene films from graphite films, which are usually produced by pressing expanded graphite

pieces into thin films [74, 75]. The internal structure of a graphite film consists of microscopic graphite blocks that cannot interlock as efficiently as individual graphene sheets. Consequently, graphite-based films are generally more brittle and break easily upon folding.

Due to the aforementioned combination of physical properties, graphene films are predestined to be high-performance GCMs. There is a variety of applications of graphene films, some of which have already been commercialized (e.g. the thermal management graphene film in Huawei’s Mate 20X and P30 [11, 76]). As conductors, the films are employed as flexible antennas [77, 78], radiofrequency filters [79], electromagnetic interference shielding [80, 65], transparent electrodes [81, 82], or heat spreaders [83, 71]. Their thickness varies with the specific application. For transparent electrodes, it ranges around 10 – 30 nm whereas the radiofrequency filters are 10 μm thick [79].

The highest reproducible conductivities of pure-carbon graphene films are on the order of 1 MSm^{-1} [79, 65, 73]. The record value of 5 MSm^{-1} presented in Reference [84] has not been reproduced so far, not even by the same group. The TCR of undoped graphene films is negative at room temperature [67, 71, 85], indicating thermally activated transport. For doped graphene films, a similar behavior as for GICs seems logical, but there is no systematic study on this topic.

Doping in graphene films is best performed in the same way as in GICs. Foreign species are intercalated in between graphene layers instead of substituting carbon atoms in the graphene lattice [86, 87]. Intercalants do not only provide carriers to the graphene layer system, they can also increase the layer spacing and decouple the layers electronically. Potassium-doped graphene films have attained conductivities of 12-15 MSm^{-1} [88, 65], surpassing the corresponding GIC at 10.9 MSm^{-1} [89]. Compared to GICs however, graphene films have most likely not been fully optimized in terms of conductivity, as the number of investigated dopants is far lower. Difficulties arise when doping is taken from the lab scale to real-world applications. The doping has to be stable in air, and potentially even at elevated temperatures. At the same time, the mechanical strength and flexibility need to be preserved. The first films, which fulfil these requirements were reported very recently by Gao’s group [13]. They used MoCl_5 as a dopant to produce a stage-4 intercalated graphene film with the record-high conductivity of 17.3 MSm^{-1} . The conductivity is stable in air and the doping does not degrade at elevated temperatures [13].

Graphene films can be produced by different methods, the most prominent ones being vacuum filtration and blade coating. Both methods are cheap and scalable and have been successfully used to produce high-performance

GCMs [72, 65]. They work with graphene dispersions as a starting material, which enables the efficient processing of large quantities. Furthermore, they are both suitable for pure graphene dispersions as well as for GO-based approaches as explained in section 2.1.1.4. Both methods are used in this work, and explained in more detail in section 4.2.3.

The first carbon nanostructured thin films were synthesized from CNTs and named buckypaper (BP) after US-American architect Richard Buckminster Fuller. They were produced in Smalley’s lab in 1998 to test the purity of their CNTs [90]. When the CNTs in BP are aligned, the in-plane electrical conductivity becomes anisotropic. The conductivity is high along the CNT length, and it is low perpendicular to it. For aligned CNTs, the film production process becomes considerably more difficult. Apart from selecting the appropriate CNTs, they need to be positioned and oriented in the right way. If the CNTs are not aligned however, the conductivity is much lower. Despite extensive research since its discovery, BP has not yet made it into a major application.

2.2.3 Fibers

Graphene fibers consist of stacked graphene flakes that are spun into textile fibers. Other names used in the literature are graphene “wire”, “cable”, or “yarn”. Graphene fibers are closely related to graphene films as they share the same or a similar microscopic structure, but differ in their macroscopic shape. The first graphene fibers were synthesized in a wet-spinning process, presented by Gao’s group in 2011 [12]: Under uniaxial flow, GO liquid crystal (GO LC, an ordered form of GO dispersion) is extruded through a nozzle into a coagulation bath. The flow and the shearing forces in the nozzle force the GO flakes into alignment along the resultant fiber axis. In the coagulation bath, a solvent exchange takes place. The dispersion medium of the GO LC is replaced by a solution with poor capability to disperse GO sheets so that GO gel fibers form. The gel fibers are then collected and dried, where they solidify and shrink in radial direction. The dried fibers are chemically or thermally reduced to become graphene fibers. The process and the final result are depicted in Figure 2.2.2.

In the years following the original publication, the process and the raw material were optimized for stronger and more conductive fibers [91, 41]. Gao’s group has presented pure graphene fibers with a stiffness of 282 GPa, a tensile strength of 1.45 GPa, electrical conductivity of 0.8 MSm^{-1} , and an ampacity of $2.3 \cdot 10^{10} \text{ Am}^{-2}$, while retaining a lower density than graphite [92]. In general, most groups have reported on fibers with an approximately round cross-section [93, 94, 95, 96], but it has been shown that a flat, belt-like

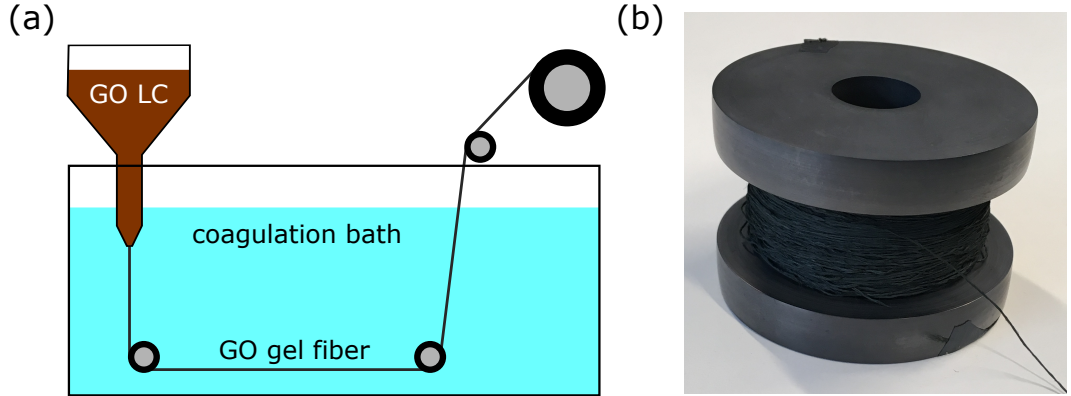


Figure 2.2.2: (a) Wet-spinning process as described in the main text. (b) Commercial wet-spun graphene fiber.

shape is advantageous for graphene fibers. It prevents the graphene flakes from being crumpled, and retains the flat arrangement that is also found in graphene films. With flat instead of tubular nozzles, the belt-like shape can be achieved [97]. Xin et al. were recently able to surpass the previous peak values for graphene fibres in this way, and created a material with a stiffness of 309 GPa, a tensile strength of 1.9 GPa, and an electrical conductivity of 1 MSm^{-1} [98].

Despite their high strength and stiffness, graphene fibers are fully flexible and can be tied into knots without degradation of the physical properties [99]. Just like the related graphene films, their unique set of characteristic features makes them excellent GCMs. Their shape is ideal for cables, and several reports of applications have been published. Demonstrators included a USB-cable and a power cable [100], a candescent bulb, bond wire, and a motor winding [92], as well as a lightweight stretchable circuit [101]. Other applications are actuators, wearable capacitors, batteries, and flexible solar cells. An overview of those is given in the reviews [91] and [41]. In contrast to graphene films, the first large-scale application is yet to come.

One of the remaining challenges before graphene fibers could replace metal wires is the electrical conductivity. Despite the great potential of individual graphene flakes (100 MSm^{-1} [22, 23]), the first fibers in 2011 were only able to reach 0.025 MSm^{-1} . Defect engineering and structural optimization led to a jump in conductivity to 0.22 MSm^{-1} [94] in 2015 and 0.8 MSm^{-1} in 2016 [92]. The record value of 1 MSm^{-1} for belt-like fibers was achieved in 2019 [98]. Studies on the TCR of graphene fibers show a behaviour similar to graphene films: Pure fibers generally exhibit a negative TCR at room temperature [100, 102], which is typical of semiconducting materials.

Analogous to graphene films, doping is required to achieve metallic levels of

electrical conductivity. Potassium-doped graphene fibers achieved conductivities of 22.4 MSm^{-1} , whereas bromine intercalation lead to 15 MSm^{-1} [100]. When exposed to air, humidity and temperatures up to 100°C , only bromine-doped fibers retained a high conductivity, which was stable at 7 MSm^{-1} . Air-stable metal-doped graphene fibers with a conductivity of 22 MSm^{-1} and a negligible temperature coefficient of resistance [102] were also reported. However, they fail to fully preserve their initial mechanical strength and flexibility. Additionally, a large part of the conduction takes place via the metal content of those fibers. Reports on fibers doped by intercalation show a positive TCR [100], with the exception of a Calcium-doped fiber in 2017 [103]. In metal-doped fibers, a tunable TCR depending on the metal content was reported [102].

Although the manufacturing process of graphene fibers is more complicated than with films, industrial textile technology makes an efficient upscaling possible. Spinning processes for polymer fibers are well established in the industry [104] and could be adapted to graphene fibers. Since the processing takes place in the form of liquid dispersions, a high-capacity production is feasible. Considering a replacement of metal wires, graphite would be a cheaper and much more accessible raw material than the respective metal ores. As with graphene films, these considerations hold true for both graphene-based and GO-based approaches.

Before the discovery of graphene in 2004, CNT fibers had already been developed [105, 106]. The 1D-nature of CNTs is better suited for tubular fibers than for films, and consequently, CNT fibers are far more advanced than buckypaper. There is no problem of anisotropic conductivity when the CNTs are aligned along the fiber axis either. Iodine-doped CNT fibers with conductivities up to 6.7 MSm^{-1} have been reported [107, 108], while commercial producers advertise similar values on their homepages (DexMat 7 MSm^{-1} , Miralon 1.7 MSm^{-1} , as of August 2019). The fiber densities are in the range of $0.33 - 1.3 \text{ gcm}^{-3}$, which is substantially lower than in the most conductive metals (Copper: 8.96 gcm^{-3} , Silver: 10.5 gcm^{-3} [109]). The values are similar to the current state of graphene fibers, but the production cost is still higher [108]. The problem of selectively producing high-quality metallic CNTs remains unsolved, and despite the 10 years lead compared to graphene fibers, CNT fibers have not made it into large-scale applications.

Nanostructured carbon-based textile fibers such as graphene or CNT fibers are the next evolutionary step in the long history of carbon fibers (CFs). The original CF dates back to the late 19th century, when Sir Joseph Swan pyrolyzed cellulose fibers for electrical light bulbs [110]. More than 100 years later, CFs are still produced by pyrolysis of carbonaceous precursor fibers made from cellulose, polyacrylonitrile (PAN), or pitch. They have evolved to

a high-tech material in terms of mechanical properties and can be tailored to specific applications [91]. Mechanically, commercial PAN-based fibers such as the TORAYCA® T1100G outperform graphene fibers with a tensile strength of 6.6 GPa and a stiffness of 324 GPa [111]. While they are mostly employed for their mechanical benefits, CFs are also electrical conductors, with conductivities approaching 0.14 MSm^{-1} [91]. This is however an order of magnitude below the record values obtained with graphene fibers. The reason for the discrepancy is found in the internal fiber structure: CFs are produced from precursors that are carbonaceous, but do not exhibit the honeycomb lattice that characterizes graphene and graphite. During the pyrolysis of the precursor fibers, graphitic domains are formed, which promote electrical conduction. However, the domains are uncontinuous and polycrystalline, with large grain boundaries [91]. Electron scattering is therefore much more pronounced than in a graphene fiber, where the honeycomb lattice of the building blocks is almost defect-free. The internal fiber structure of CFs is also the reason why they are brittle and not radially flexible like graphene fibers. For further information on the evolution from carbon to graphene fibers, consider Reference [91] and References therein.

2.2.4 Assessment of the state of the art

Given the current state of the art, GCMs already outperform metallic conductors in many respects such as low weight, flexibility, or a favorable TCR. However, the electrical conductivity still needs to be reliably improved, ideally to a value that rivals copper. All the additional extraordinary physical properties only become truly significant when the conductivity is high enough. Table 2.1 compares the electrical conductivities, densities, and TCRs of macroscopic GCMs and highly conductive metals.

For GCMs and related materials, experimental work is far more advanced than theoretical descriptions. While the first carbon-based conductors were synthesized decades ago, there is very little theoretical work published on the topic to date. Mildred and Gene Dresselhaus discuss several models of the conduction mechanisms in GICs in their review article [46], but this is even before the synthesis of the first monolayer graphene flakes. For modern GCMs like the thin films [65] and fibers [100] with metallic electrical conductivity, the imbalance remains. Many research groups have presented experimental results, but the materials have hardly ever been modeled or described theoretically. For an efficient and systematic conductivity optimization, a proper theoretical description is much needed.

| Material | Electrical conductivity in air [MSm^{-1}] | Density [gcm^{-3}] | TCR at 20°C [10^{-3} K^{-1}] | References |
|--|---|----------------------------------|---|----------------|
| Silver | 62 | 10.5 | 3.8 | [14, 109, 112] |
| Copper | 59 | 8.96 | 3.9 | [14, 109, 112] |
| Aluminum | 38 | 2.70 | 4.3 | [15, 109, 112] |
| Graphene film, undoped | 1.1 | 2.03 | -1 | [73, 13] |
| Graphene fiber, undoped | 1 | < 2.26 | -0.39 | [98, 100, 102] |
| Graphene film, MoCl ₅ -doped | 17.3 | 2.37 | 0.14 | [13] |
| Graphene fiber, bromine-doped | 15 | 1.6 | 0.57 | [100] |
| CNT fiber, iodine-doped | 6.7 | 0.33 | 0.82 | [107] |
| AsF ₅ -GIC | 90 | unknown | unknown | [63] |

Table 2.1: Overview of important properties of GCMs and selected metals

3 Electrical conductivity modeling of graphene-based conductor materials

3.1 Introduction

In this chapter, a theoretical description of electrical conduction in GCMs is developed and transferred into a simulation. Based on the micro- or nanoscopic raw material properties, the overall electrical conductivity of a GCM is predicted. The limits of the electrical conductivity are computed and evaluated in terms of competitiveness with state of the art technology. Since GCMs are macroscopic conductor materials, a quantum mechanical description is not required in the first instance. The expected operating point is at room temperature or above, and the lateral flake sizes of the raw material are in the range of several micrometers or more. Quantum effects are not expected in this regime. For comparison, three fundamentally different approaches are implemented. The simulation methods complement each other and help to identify key parameters in GCM optimization and production. Chapter 3 is divided into three sections. Each section covers a different approach to GCM modeling, with complexity gradually increasing. In the first part, an analytical description of electrical conduction in a GCM is developed and evaluated. Part two is an analysis of GCMs with the finite element method. In the third part, a random resistor network model is presented. As the most appropriate method for GCM simulation, it is used for detailed materials modeling with thorough parameter studies. In the course of this chapter, the results of the different methods are brought together. The connection to the technical implementation is discussed and conclusions for the practical realization are drawn. Parts of this chapter have been published in References [113] and [114].

3.2 Analytical model

3.2.1 Derivation

The simplest and most elegant mathematical description of a physical situation is an analytical expression. However, analytical descriptions normally only exist for simplified or restricted systems. But even in a simplified form, a substantial gain in knowledge is possible, since general dependencies and important trends can be identified. In the case of GCMs, an analytical model is desired as a first step from qualitative to quantitative analysis. Even if it does not yield accurate data for real-world materials, it helps in identifying limits and quantifying dependencies. As an example, the maximum achievable conductivity of an idealized material without defects is most likely greater than or equal to the maximum conductivity of a real-world material. As it is the case with highly conductive real-world GCMs, the simulation is focused on materials with packing densities of 0.7 or more. When packing densities are much lower, there is a high degree of porosity and a reduced amount of current-carrying material. This in turn leads to a severe reduction in electrical conductivity. Experimental data from the literature shows that GCMs with a packing density greater than 0.7 can be reliably produced [65, 100]. This also implies that graphene flakes can be modeled as rigid, and sagging across multiple layers is ruled out. Each flake is supported by a sufficient contact surface of the underlying flakes.

Since the electrical conductivity is a geometry-independent material property, the GCM is modeled as a finite cuboid. The cuboid comprises N identical but independent conduction channels. A single channel consists of a series of overlapping graphene flakes (Figure 3.2.1), described by a series connection of resistors. The resistors alternate between in-plane and out-of-plane connections. The resistance of a single channel R_{ch} is thus given as

$$R_{\text{ch}} = \sum_{i=1}^n R_i^{\text{in}} + \sum_{j=1}^m R_j^{\text{out}} \quad (3.2.1)$$

with n in-plane resistances R_i^{in} and m out-of-plane resistances R_j^{out} . It is assumed that there are effective resistances \bar{R}_{in} and \bar{R}_{out} such that

$$n \cdot \bar{R}_{\text{in}} = \sum_{i=1}^n R_i^{\text{in}} \quad (3.2.2)$$

$$m \cdot \bar{R}_{\text{out}} = \sum_{j=1}^m R_j^{\text{out}} \quad (3.2.3)$$

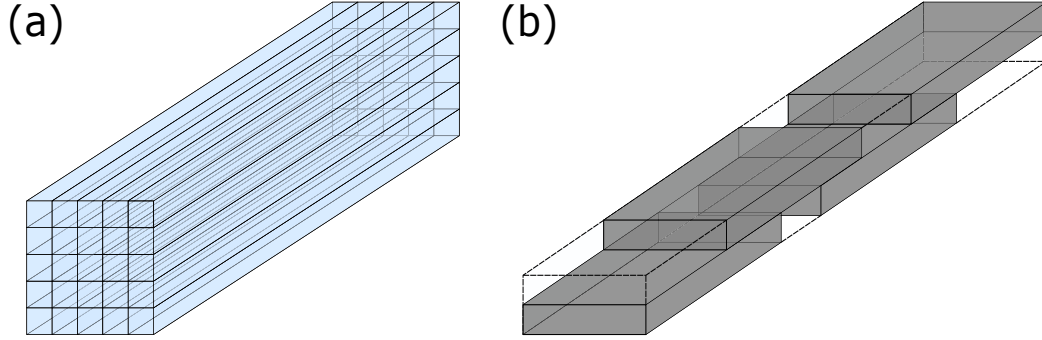


Figure 3.2.1: (a) Model of a GCM as a cuboid with identical but independent channels. (b) Details of a single channel. Overlapping flakes form the internal structure of a conduction channel and define its geometry. Reprinted with permission from [113]. Copyright 2018 American Chemical Society.

This is a suitable approximation for a large number of resistors, because in the limit of sufficiently large systems, self-averaging takes place [115]. Therefore, there is always an ordered effective medium with the same properties as the disordered one. Here, this corresponds to an effective resistance as described above. Accordingly, the representative mean quantities \bar{l}_{in} , \bar{A}_{in} , \bar{l}_{out} , \bar{A}_{out} are introduced. They describe the length and cross-sectional area of the in-plane and out-of-plane resistances such that

$$\bar{R}_{\text{in}} = \sigma_{\text{in}}^{-1} \cdot \frac{\bar{l}_{\text{in}}}{\bar{A}_{\text{in}}} \quad (3.2.4)$$

$$\bar{R}_{\text{out}} = \sigma_{\text{out}}^{-1} \cdot \frac{\bar{l}_{\text{out}}}{\bar{A}_{\text{out}}} \quad (3.2.5)$$

with the in-plane and out-of-plane conductivities σ_{in} and σ_{out} . With these quantities, the conductance of a single channel can be expressed as

$$G_{\text{ch}} = \left(n \cdot \sigma_{\text{in}}^{-1} \cdot \frac{\bar{l}_{\text{in}}}{\bar{A}_{\text{in}}} + m \cdot \sigma_{\text{out}}^{-1} \cdot \frac{\bar{l}_{\text{out}}}{\bar{A}_{\text{out}}} \right)^{-1} \quad (3.2.6)$$

The total conductance of the GCM is equal to the sum of the conductances of the N individual channels. To compute the total conductivity σ_{tot} , the length l_{tot} and cross-sectional area A_{tot} of the GCM are introduced.

$$\sigma_{\text{tot}} = \frac{l_{\text{tot}}}{A_{\text{tot}}} N \cdot G_{\text{ch}} \quad (3.2.7)$$

$$\sigma_{\text{tot}} = \frac{l_{\text{tot}}}{A_{\text{tot}}} N \cdot \left(n \cdot \sigma_{\text{in}}^{-1} \cdot \frac{\bar{l}_{\text{in}}}{\bar{A}_{\text{in}}} + m \cdot \sigma_{\text{out}}^{-1} \cdot \frac{\bar{l}_{\text{out}}}{\bar{A}_{\text{out}}} \right)^{-1} \quad (3.2.8)$$

The total length can be expressed as the sum of all the in-plane lengths $l_{\text{tot}} = n \cdot \bar{l}_{\text{in}}$. As each in-plane connection is followed by an out-of-plane connection, and a large number of flakes per channel is assumed, the total length can be rewritten as

$$l_{\text{tot}} \approx m \cdot \bar{l}_{\text{in}}. \quad (3.2.9)$$

For the out-of-plane length, the average graphene flake thickness $\bar{l}_{\text{out}} = t_{\text{gr}}$ is introduced. According to the construction of the model, the cross-sectional area is identical for each channel such that

$$A_{\text{tot}} = N \cdot A_{\text{ch}}. \quad (3.2.10)$$

With equations (3.2.9) and (3.2.10), the total conductivity is rewritten as

$$\sigma_{\text{tot}} = \left(\sigma_{\text{in}}^{-1} \cdot \frac{A_{\text{ch}}}{\bar{A}_{\text{in}}} + \sigma_{\text{out}}^{-1} \cdot \frac{A_{\text{ch}} \cdot t_{\text{gr}}}{\bar{l}_{\text{in}} \cdot \bar{A}_{\text{out}}} \right)^{-1} \quad (3.2.11)$$

Assuming rectangular graphene flakes with the same width as the conduction channel (Figure 3.2.1 (b)), the ratio of the average in-plane cross-sectional area and the channel cross-sectional area yields the packing density of the channel, which is equal to the packing density p of the GCM.

$$\frac{\bar{A}_{\text{in}}}{A_{\text{ch}}} = p \quad (3.2.12)$$

The height of the channel corresponds to the height of two graphene flakes. The width w_{ch} of the individual channels has not been specified any further, such that

$$A_{\text{ch}} = w_{\text{ch}} \cdot 2t_{\text{gr}}. \quad (3.2.13)$$

If quadratic overlap patches are assumed $w_{\text{ch}} = \sqrt{\bar{A}_{\text{out}}}$, the following expression for the total conductivity is obtained

$$\sigma_{\text{tot}} = \left((p \cdot \sigma_{\text{in}})^{-1} + \frac{2t_{\text{gr}}^2}{\bar{l}_{\text{in}} \cdot \sqrt{\bar{A}_{\text{out}}}} \cdot \sigma_{\text{out}}^{-1} \right)^{-1} \quad (3.2.14)$$

3.2.2 Results and discussion

Four main features of the microscopic material are included in the final formula: the in-plane and out-of-plane conductivities, the overall packing density, and the geometric properties of the individual flakes. By the description as a chain of resistors, they are divided into two groups:

$$(p \cdot \sigma_{\text{in}})^{-1} \quad (3.2.15)$$

and

$$\frac{2t_{\text{gr}}^2}{\bar{l}_{\text{in}} \cdot \sqrt{\bar{A}_{\text{out}}}} \cdot \sigma_{\text{out}}^{-1} \quad (3.2.16)$$

Expression (3.2.15) relates the packing density to the in-plane conductivity. The reason why those quantities should be connected might not be evident at the first glance. However, from the derivation it is obvious that the packing density contains the ratio of the average in-plane cross-section to the individual channel cross-section, an important figure for in-plane conduction. Expression (3.2.15) confirms mathematically what is intuitively clear: A high in-plane electrical conductivity and a high packing density are beneficial for overall electrical conductivity.

Expression (3.2.16) relates the geometric aspects of the graphene flakes to the out-of-plane conductivity. In this case, the connection is more obvious. The average overlap area and the graphene flake thickness correspond to the cross-sectional area and the distance in out-of-plane conductance. The in-plane distance on the other hand determines the number of flake transitions per unit length. Apart from a high out-of-plane conductivity, large overlaps and long in-plane distances favor the overall electrical conductivity. A particularly insightful representation is obtained when the total electrical conductivity is plotted with respect to the out-of-plane conductivity. It naturally allows for the investigation of the influence of all the quantities in equation (3.2.14).

In Figure 3.2.2 (a), σ_{tot} is shown as a function of σ_{out} for a fixed packing density $p = 0.8$ and a set of in-plane conductivities. When varying σ_{out} , three regimes can be identified: In regime I, for small σ_{out} , the total electrical conductivity is close to zero, irrespective of the in-plane conductivity. The different curves are indistinguishable. The small out-of-plane conductivity entirely dominates the total conductivity of the GCM. An increase in the in-plane conductivity alone cannot improve the overall performance. The second regime is a transitional range for medium σ_{out} where the total conductivity rises sharply. Here, the curves split up and the magnitude of the in-plane conductivity becomes decisive. For large σ_{out} , a saturation regime is reached. In this range, the exact value of the out-of-plane conductivity is not relevant any more. The limiting factors are the packing density and the in-plane conductivity, which define the limit of the total conductivity:

$$\sigma_{\text{tot}} \rightarrow p \cdot \sigma_{\text{in}} \equiv \sigma_{\text{max}} \quad (3.2.17)$$

This limit value is of practical importance. In expression (3.2.16), the size of the graphene flakes can compensate a low out-of-plane conductivity. Packing density and in-plane conductivity however, are clearly restricted, which is

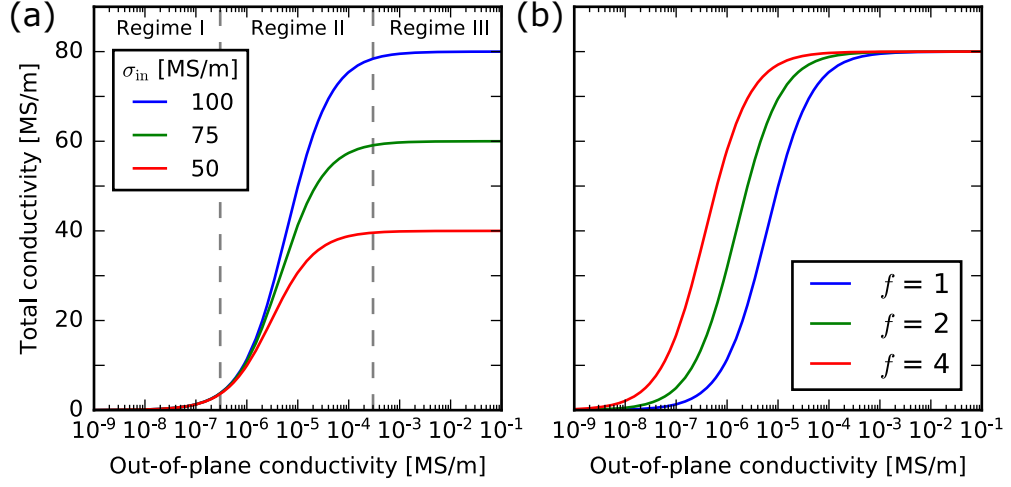


Figure 3.2.2: Total conductivity of a GCM as a function of out-of-plane flake conductivity for (a) different σ_{in} -values and (b) different flakes sizes.

why $p \cdot \sigma_{\text{in}}$ serves as a first approximation for the upper limit of the electrical conductivity of a GCM. The question how close the total conductivity gets to this theoretical maximum is determined by the out-of-plane conductivity and the geometric properties of the flakes, as will be shown in the following.

In Figure 3.2.2 (b), the size of the flakes is varied. They are scaled by multiplying the in-plane dimensions by a factor f while the thickness is kept constant. Thus, the overall structure and packing density remain constant while the side lengths increase by f . In terms of the analytical description, \bar{l}_{in} increases by f and \bar{A}_{out} by f^2 . Consequently, expression (3.2.16) has to be multiplied by the pre-factor f^{-2} if the flakes are scaled by a factor f . When the flake size is altered, the shape of the $\sigma_{\text{tot}}(\sigma_{\text{out}})$ -curves does not change. The saturation limit also remains identical as it only depends on the packing density and the in-plane conductivity. However, the curves shift along the x -axis. For larger flakes, the curves shift towards lower σ_{out} values and vice versa. This leads to an important conclusion: To achieve a certain desired total electrical conductivity in a GCM, flake size can be exploited to compensate an unsatisfactory out-of-plane conductivity. With the considerations from above, the effect is quantified in a simple relation: Increasing the lateral flake dimensions by a factor f has the same effect as increasing the out-of-plane conductivity by the factor f^2 . This is also the reason why the limit value σ_{max} can be reached even when σ_{out} is smaller than σ_{max} by orders of magnitude.

Figure 3.2.3 shows σ_{tot} as a function of the lateral flake size for various values

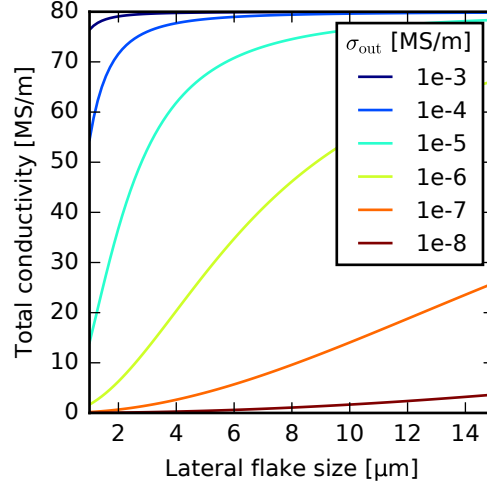


Figure 3.2.3: Total conductivity of a GCM as a function of the lateral flake size for various σ_{out} and fixed $p \cdot \sigma_{\text{in}} = 80 \text{ MSm}^{-1}$.

of σ_{out} . For any combination of σ_{in} and σ_{out} , an increase in flake size leads to an increase in total electrical conductivity until overall saturation is reached. In theory, even the lowest values of σ_{out} can be compensated in this way. In fact, several publications show that large graphene flakes in a GCM lead to a higher overall conductivity [116, 117, 80, 72]. But so far, there has not been a mathematical relation which connects the two aspects.

In the transition regime, the clear separation of expressions (3.2.15) and (3.2.16) is lost. In a physical interpretation, the transition regime is located around the point where both expressions are equally influential on the total conductivity. Mathematically, this is expressed as follows:

$$(p \cdot \sigma_{\text{in}})^{-1} = \frac{2t_{\text{gr}}^2}{\bar{l}_{\text{in}} \cdot \sqrt{\bar{A}_{\text{out}}}} \cdot \sigma_{\text{out}}^{-1} \quad (3.2.18)$$

$$\Leftrightarrow \sigma_{\text{tot}} = \frac{1}{2} \cdot \sigma_{\text{in}} = \frac{1}{2} \sigma_{\text{max}} \quad (3.2.19)$$

The different influencing factors compete, and the dominance of individual parameters gradually shifts with the change in out-of-plane conductivity. To visualize the effect, Figure 3.2.4 depicts the total conductivity of a GCM as a function of (a) in-plane conductivity and (b) packing density for various σ_{out} . Figure 3.2.4 (a) shows that in general, a larger in-plane conductivity always leads to a larger total conductivity. But the smaller σ_{out} , i.e. the further away from the saturation regime, the more the total conductivity levels off and eventually stagnates. Physically, this corresponds to decreasing conductances between individual flakes. At some point, even infinitely

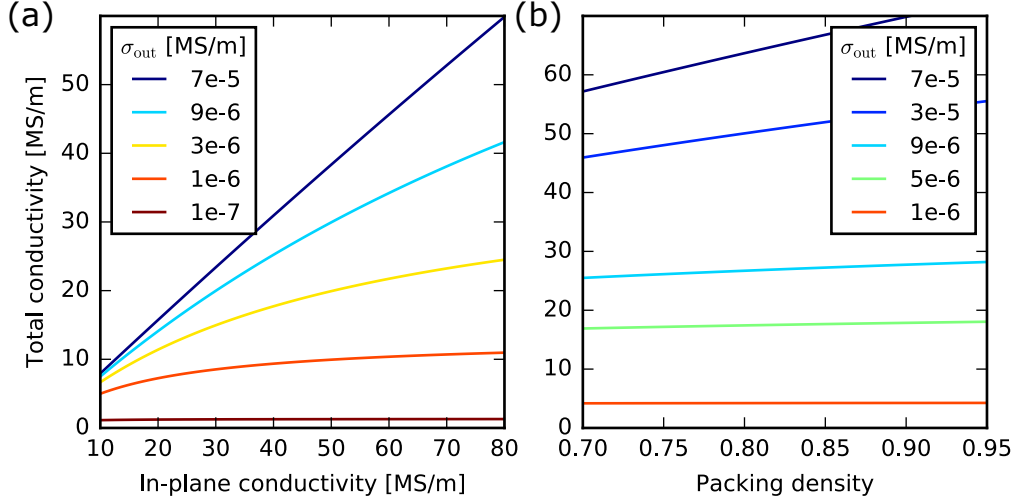


Figure 3.2.4: Total conductivity of a GCM as a function of (a) in-plane conductivity and (b) packing density for various σ_{out} .

large in-plane conductances cannot compensate the small out-of-plane conductances anymore.

The four upper curves in Figure 3.2.4 (a) are located in the transition regime as indicated in Figure 3.2.2 (a). Here, a small increment in out-of-plane conductivity has a strong impact on the total conductivity. Since expression (3.2.15) is simply the product of p and σ_{in} , their individual influence in the transition regime is identical. It is evident that a higher packing density always corresponds to more current-carrying material and should thus lead to a higher total conductivity. But a minimum out-of-plane conductivity is required in order to exploit the material to full extent. Hence, the impact of the packing density decreases for smaller σ_{out} . This is reflected by the slopes of the curves, which decrease continuously with decreasing σ_{out} .

3.2.3 Extension of the analytical model

Going beyond the basic analytical description given by equation (3.2.14), the model can be extended to fit more realistic and more complex systems. Presumably, the most important difference between the model and a real-world structure is the degree of order. A real-world system is expected to be disordered, with a wide distribution of different flake shapes and sizes. Moreover, flakes are arranged randomly, which leads to more complex current paths. These aspects mainly affect expression (3.2.16) of the analytical formula, which suggests that a non-ideality factor might be sufficient to compensate for the simplifications of the model. Such a non-ideality factor b would change

equation (3.2.14) to

$$\sigma_{\text{tot}} = \left((p \cdot \sigma_{\text{in}})^{-1} + b \cdot \frac{2t_{\text{gr}}^2}{\bar{l}_{\text{in}} \cdot \sqrt{\bar{A}_{\text{out}}}} \cdot \sigma_{\text{out}}^{-1} \right)^{-1}. \quad (3.2.20)$$

In the following chapters, it will be analyzed whether this adaptation suffices for a better description of realistic, disordered systems.

Note that the approach differs from the typical effective medium approximation (EMA). In EMA for random resistor networks, a disordered system is mapped onto an ordered system by utilizing a universal effective resistance r_{eff} . An ordered resistor network is generated where all the resistances are equal to r_{eff} . The value of r_{eff} is computed such that the overall resistance of the ordered network equals the overall resistance of the disordered network. Hence, in a typical EMA approach, a non-ideality factor as introduced above would already be integrated in the effective resistance r_{eff} . However, the advantage of equation (3.2.20) is the direct comparison of a disordered system to an ordered system with the same average geometric features. In this case, the non-ideality factor b becomes a measure of how much the disordered network differs from the ideal state. The larger b , the greater the difference between the ordered and the disordered system.

Apart from the comparison of ordered and disordered GCMs, the analytical model can also be extended to different conductor materials. A variation of the input parameters allows for the investigation of building blocks other than graphene mono- or multilayers. This includes entirely different atoms and molecules, as it would be the case for transition metal dichalcogenides. But it also covers graphene platelets decorated with dopant atoms. Thicknesses and conductivities would become effective quantities, which are valid for the new building blocks. For those cases, the chain of resistors still provides a useful description of the electrical characteristics of the system.

Another extension of the analytical model would be the consideration of multiphysical properties. For any multiphysics extension, the input parameters presented above become dependent on new quantities: strain, temperature, fields, etc. If a mathematical description of the dependence is provided, it can be easily integrated into equation (3.2.20).

3.2.4 Summary

Despite the simplicity of the analytical description, the model yields useful guidelines and limits. The examined dependencies provide a conclusive picture that is in line with preliminary considerations. Furthermore, it is a first step towards a comprehensive quantitative description of electrical conduction in a GCM. At this point, the principal findings from the analytical

model can be summarized as follows: There is an upper limit of electrical conductivity of a GCM, which is determined by packing density and in-plane conductivity. Geometric flake properties as well as the out-of-plane conductivity dictate how close the total conductivity gets to the theoretical maximum. Flake sizes and out-of-plane conductivity can compensate each other. If a certain total electrical conductivity is desired, the interplay of the microscopic parameters has to be considered. The analytical model and its suitability for realistic systems will be further tested and constantly reviewed in the following chapters. In the course of this, it will become clear to what extent the simplifications assumed in this section are valid.

3.3 Finite element analysis

3.3.1 Introduction to the method

In a step towards more realistic geometric arrangements, the finite element method (FEM) is used. A detailed explanation of the method beyond the scope of this work can be found in References [118] and [119]. FEM is a numerical method to solve differential equations that is applicable to various physical problems. A physical system is subdivided into many smaller and less complex parts, the so-called “finite elements” that give the method its name. The finite elements are characterized by simple algebraic equations, which are evaluated at discrete points in space. To obtain the physical behavior of the complete system, the equations are combined into a larger system of equations, which is subsequently solved with numerical methods. The discrete representation of the complete geometry is called “mesh”. The term “finite element analysis” (FEA) is used when a problem is studied with FEM.

Compared to the analytical description, there are major changes in geometric modeling, because FEM allows for disordered systems. Here, polygonal shapes are used to model graphene flakes as accurately as practically possible. They are randomly distributed and oriented within the GCM. Due to that, overlaps vary in size and shape. As before, each flake features an anisotropic electrical conductivity. However, by using FEM, the spreading resistance within the flakes is inherently taken into account. Due to the higher degree of complexity, FEM is computationally far more expensive than an analytical description. Therefore, the systems investigated in this section are limited in size, which has to be compensated by employing statistical methods. In the course of this section, the FEA results are compared to the analytical model. Thus, important conclusions for the validity of both methods are drawn.

For the FEA performed here, a combination of self-written code and commercial software is used. The flakes and the geometric structure of the GCM are generated with a specifically developed algorithm [114], implemented in Python. The geometry is imported into the commercial software COMSOL Multiphysics® for FEA.

3.3.2 Geometry Generation

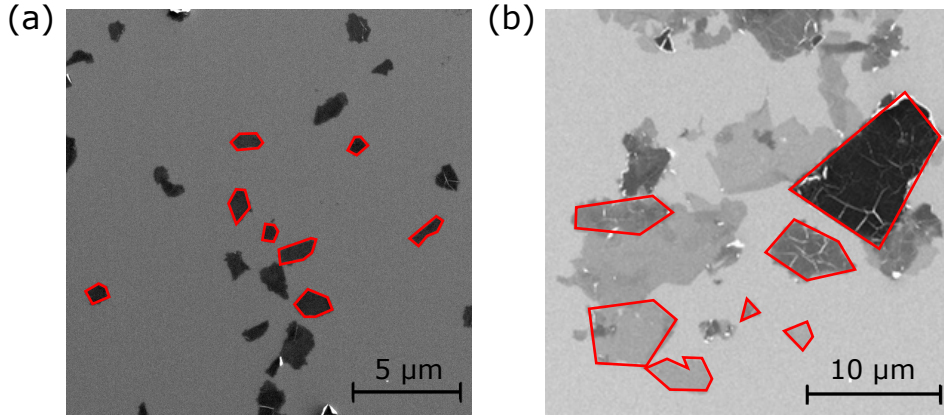


Figure 3.3.1: Scanning electron micrographs of (a) graphene flakes and (b) few- and multilayer GO flakes with exemplary outlines.

Before FEM is applied, an algorithm which models the geometry of a GCM is devised. It has to meet various criteria: (i) The generated graphene flakes have to be randomly oriented and need to feature a large number of different shapes. (ii) The overall packing density needs to be adjustable in a range from 0.7 to nearly 1.0. (iii) The statistical distribution of flake sizes needs to be adjustable. (iv) The spatial distribution of flakes should be manipulable. These requirements demand a combination of randomness (i) and control (ii)-(iv). Control is necessary to perform meaningful parameter studies in a well-defined range while a realistic degree of randomness is required to adhere to real-world production scenarios.

From various publications on GCMs, the appearance of graphene or GO flakes processed in aqueous dispersions is known. As shown in Figure 3.3.1, polygons are particularly suitable for describing their shapes. In most cases, five to six edges are sufficient to model a coarse flake outline.

The geometry generation is conducted as follows: As the first step, 2D layers are filled with graphene flakes represented by polygons. Each layer is filled with M randomly positioned points as shown in Figure 3.3.2 (a). The points are selected one after the other to create polygons around the respective

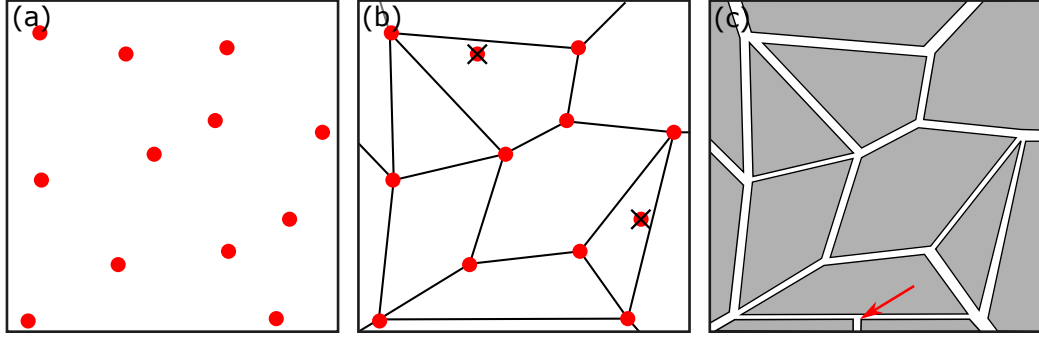


Figure 3.3.2: Illustration of the geometry algorithm. (a) Randomly positioned points are generated. (b) Polygons are constructed from the points. Excess or leftover points are discarded. (c) Polygons are shrunk to obtain the desired packing density. A long and thin polygon is divided in the middle as indicated by the red arrow. Reprinted with permission from [114].

positions. At each selected point P , the N nearest neighboring points are chosen to form the convex hull, i.e. a polygon with a maximum of $N + 1$ edges. With the remaining points, the process is repeated until every point has been considered to become part of a polygon. If a new polygon P_{new} intersects with existing polygons P_{old} , only the difference $P_{\text{new}} \setminus P_{\text{old}}$ is added. Since the original points are positioned at random, it is possible that some are located inside their corresponding convex hull. Those excess points are discarded (Figure 3.3.2 (b)). Furthermore, voids and leftover points can remain inside the 2D layer when no more neighboring points are left to form a polygon. The leftover points are discarded as well and the voids are filled to form additional polygons. This yields a 2D layer which is completely filled (packing density = 1.0) with randomly shaped and oriented polygons. At this stage, the geometry is refined to match real-world production scenarios more closely. In the manufacturing process of highly conductive GCMs, sub-micrometer sized graphene flakes are often undesirable and are thus removed [73]. Large graphene flakes on the other hand are limited in size due to the raw material choice or due to further processing. A prominent example is sonication, which is sometimes used to separate graphene multilayers but which is also known to reduce lateral flake size [120]. To allow for these boundary conditions, the geometry algorithm removes flakes with an area below a predefined lower threshold and splits polygons that are larger than a predefined upper threshold. Depending on the manufacturing and processing techniques, flake appearance may vary. Some flakes exhibit long and thin shapes while others feature similar side lengths. By restricting the ratio of flake perimeter to flake area, the amount of long and thin flakes can be con-

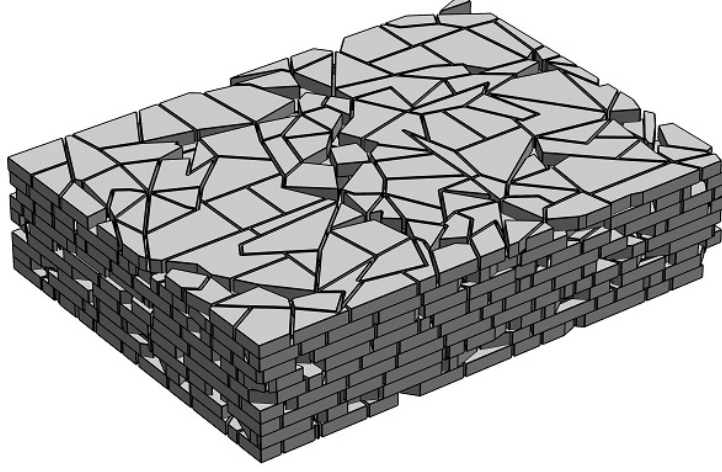


Figure 3.3.3: 3D view of the geometric structure of a GCM.

trolled (Figure 3.3.2 (c)). The fine tuning of the geometric flake distribution slightly reduces the packing density p in each layer but it still remains close to 1. To finalize the geometry, p is adjusted to a desired value \hat{p} . There are two main options to achieve this goal. All polygons can either be uniformly shrunk until $p = \hat{p}$ as depicted in Figure 3.3.2 (c). Alternatively, randomly chosen flakes from each layer can be resized or eliminated. The first approach leads to a homogeneous spatial distribution of the polygons while the second one results in spatially clustered graphene flakes. If necessary, the algorithm can combine both methods.

In this work, the focus is on GCMs which are optimized in terms of electrical conductivity, a property that necessitates high packing densities (see sections 3.2.1 and 3.2.2). When going to more realistic geometries than in the analytic model, it still makes sense to model flakes as rigid because of the high packing density. Due to graphene's exceptional stiffness, it is reasonable to assume that the flakes sufficiently support each other to prevent sagging. Furthermore, it has been shown in Reference [98] that arranging flakes in a flat layered way is both feasible and also beneficial for overall conductivity. All these aspects are taken into account in the geometry generation.

When the 2D layers are completed, the self-written code translates the geometric objects from Python into a COMSOL file. They are assigned a finite thickness and stacked on top of each other to form a three-dimensional (3D) object. Figure 3.3.3 shows an example of a structure designed by the geometry algorithm and imported into COMSOL Multiphysics®. It features a

spatially homogeneous flake distribution with flakes larger than $1\text{ }\mu\text{m}^2$, and a packing density of $p = 0.8$. The out-of-plane axis is displayed 3000 times larger than it would actually be the case for graphene flakes.

The geometry algorithm described here fulfils the initially defined requirements. It offers control over the different material properties and can be used efficiently to tailor a large variety of flake distributions. At the same time, the generated flakes are randomly shaped and distributed as it is expected in real-world scenarios. Due to the multitude of fine tuning parameters, boundary conditions set by production methods and raw materials can easily be respected.

3.3.3 Mathematical formulation of the problem

The target quantity of the analysis is the electrical conductivity in a steady state: the direct current (DC) electrical conductivity σ_{tot} . A constant potential difference V is applied to the side faces of the GCM, which leads to a static electric field inside the conductor material. Assuming that no extra charges carriers are generated or eliminated, a time-independent stationary current emerges. The electric potential Φ inside the GCM is computed to describe the system mathematically and to obtain the overall electrical conductivity σ_{tot} . Due to the steady-state situation, Laplace's equation for the electric potential is employed

$$\Delta\Phi = 0. \quad (3.3.1)$$

The boundary conditions are the fixed potential values on the side faces of the GCM. When the electric potential is known, the current density \mathbf{J} can be computed with the generalized version of Ohm's law

$$\mathbf{J} = -\boldsymbol{\sigma}\nabla\Phi \quad (3.3.2)$$

where the conductivity tensor $\boldsymbol{\sigma}$ allows for anisotropic conductivity. In the case of graphene flakes, the same differentiation between σ_{in} and σ_{out} as in chapter 3.2 is reasonable, such that in a cartesian coordinate system

$$\boldsymbol{\sigma} = \begin{pmatrix} \sigma_{\text{in}} & 0 & 0 \\ 0 & \sigma_{\text{in}} & 0 \\ 0 & 0 & \sigma_{\text{out}} \end{pmatrix}. \quad (3.3.3)$$

The equations above are mapped onto the discrete lattice, the mesh, provided by FEM. A new system of equations emerges which is transformed into a matrix equation. The solution of the matrix system yields the value of Φ and thus \mathbf{J} at every point of the mesh. By integrating the current density

over one of the side faces S of the GCM, the total current I_{tot} is obtained. Due to current conservation, the amount of current which enters one side face equals the amount of current flowing through the other side face.

$$I_{\text{tot}} = \int_S \mathbf{J} \cdot d\mathbf{A} \quad (3.3.4)$$

with the surface element $d\mathbf{A}$ of the surface S . Employing the length l_{tot} and cross-sectional area A_{tot} of the GCM, the overall electrical conductivity is computed according to

$$\sigma_{\text{tot}} = \frac{I_{\text{tot}}}{V} \frac{l_{\text{tot}}}{A_{\text{tot}}}. \quad (3.3.5)$$

3.3.4 Results and discussion

In contrast to the analytical model, finite size effects and numerical stability are of great importance in the application of FEM. For the model systems investigated here, a minimum of 8 stacked 2D layers and approximately 100 flakes per layer are required to produce results that are independent of the system size. Homogeneous flake distributions can be modeled with smaller systems while inhomogeneities usually require a larger system size. For all the analyzed systems presented in this section, convergence and stability are adequately tested.

The FEA starts with the investigation of the simple model system depicted in Figure 3.3.3. Figure 3.3.4 (a) shows a $\sigma_{\text{tot}}(\sigma_{\text{out}})$ -curve as discussed in section 3.2.2 while Figure 3.3.4 (b) depicts the color-coded voltage drop across the corresponding structure for a given parameter set. The $\sigma_{\text{tot}}(\sigma_{\text{out}})$ -curve computed with FEM exhibits the same prominent features as the curve computed with the analytical model. The same three regimes can be identified and as expected, the overall conductivity saturates for large values of σ_{out} . Figure 3.3.4 (c) shows a smooth and even voltage drop across the whole structure. For better comparability, Figure 3.3.5 (a) compares a $\sigma_{\text{tot}}(\sigma_{\text{out}})$ -curve computed with FEM to the respective $\sigma_{\text{tot}}(\sigma_{\text{out}})$ -curve computed with the analytical expression. For the latter, the packing density, the average flake diameter and the average overlap area are extracted from the geometry used for the FEA. Apart from the general similarity, two noticeable differences stand out. First, the curves are shifted on the x -axis against each other and second, the FEM-curve is smeared out. Considering that two methods with different degrees of complexity are compared, the smearing is easily explained: In the analytical model, all the overlaps have the same surface area and consequently the same out-of-plane conductance. Thus, they exceed the threshold where the out-of-plane conductance becomes large compared to the

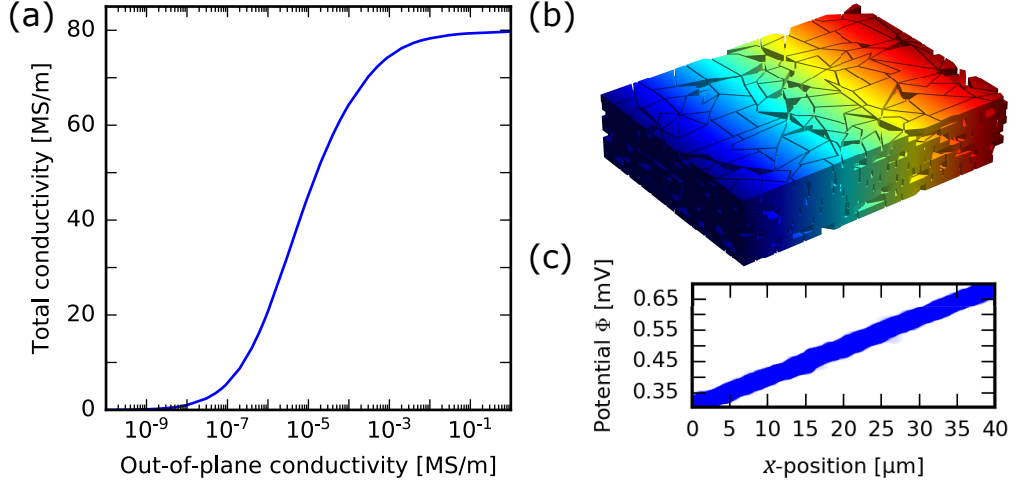


Figure 3.3.4: (a) Exemplary $\sigma_{\text{tot}}(\sigma_{\text{out}})$ -curve from FEA. (b) Color-coded voltage drop for $\sigma_{\text{out}} = 1 \text{ Sm}^{-1}$ and (c) corresponding electric potential along the current direction (x -direction of the structure). The seemingly thick curve results from the individually plotted potentials of all the finite elements at the respective x -positions.

in-plane conductance at the same time. As a result, the transition regime is rather narrow in the analytical model. In contrast, the geometry used for FEA features differently sized overlap areas and meandering current paths. Due to that, the threshold at which an overlap can be considered highly conductive varies from overlap to overlap. Therefore, the overall conductivity curve rises earlier because of comparatively large overlaps and saturates later because of comparatively small overlaps. This broadens the transition regime and smears the curve. The slight displacement of the curves on the x -axis is a geometry-specific effect that varies from structure to structure. The variation decreases for larger and more homogeneous structures but it does not disappear completely for all geometries. However, it can be mitigated by employing the non-ideality factor b introduced in equation (3.2.20). Taking the curve from FEA as a reference, a least squares fitting routine determines b , and the dashed curve in Figure 3.3.5 (a) emerges. In that specific case, b is determined to be 1.33, and in general, it ranges between 1 and 1.5. The value depends on the exact flake configuration, but it is always larger than 1. The non-ideality parameter indicates how much the disordered system (the system used for FEA) differs from the idealized system (the analytical model with $b = 1$) with equivalent average parameters. Here, the deviation is rather small. Despite the difference in the curves' slopes, the fact that they are both centered around a similar out-of-plane conductivity indicates

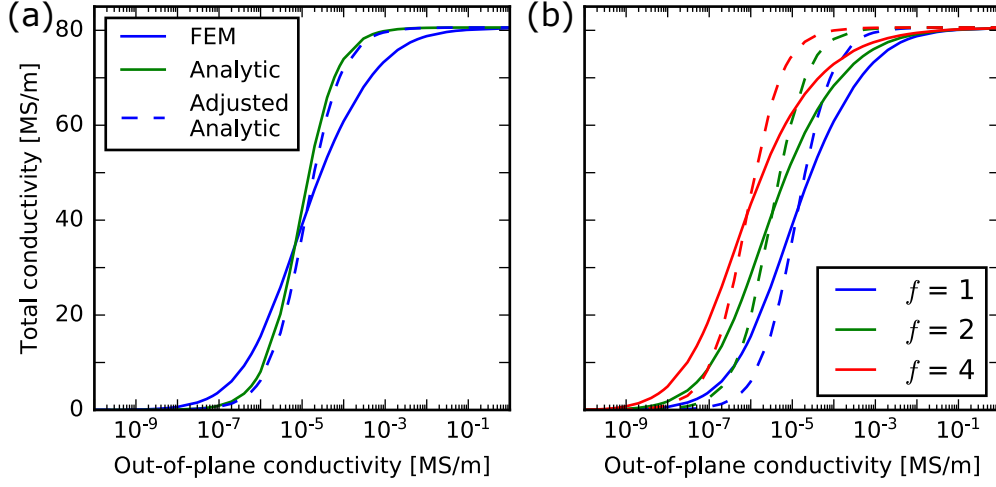


Figure 3.3.5: (a) Comparison of FEM, the analytical model, and the adjusted analytical model with $b = 1.33$. (b) Scaling for increased flake sizes in FEM (solid lines) and in the analytical model (dashed lines).

a degree of accordance.

However, there are far more significant similarities between the two methods. For the model system investigated here, the saturation value of the conductivity is the same as the ideal saturation value computed with the analytical model. This is a non-trivial observation with strong implications. The fact that arbitrarily shaped and oriented flakes, which compose a disordered system, can achieve the same electrical conductivity as an idealized ordered system, is not evident. A more in-depth analysis of this phenomenon will follow in the next section.

The second similarity between the FEA results and the analytical model concerns the effects of different flake sizes. In section 3.2.2, it was found that when the lateral flake sizes are scaled, the $\sigma_{\text{tot}}(\sigma_{\text{out}})$ -curve shifts on the x -axis accordingly (Figure 3.2.2 (b)). The same holds true for the FEM case. Even more, the shift observed for the two methods is identical. Figure 3.3.5 (b) shows the results for an FEM model system where the geometry is scaled. The flake thickness is retained while the in-plane dimensions are multiplied by a factor f . This leaves the 2D shapes, the packing density p and the conductivities unaltered. Thus, the effect of the flake sizes can be investigated independently from other influences. For direct comparison, the corresponding analytical curves are also displayed in the same plot. It is immediately visible that for the various values of f , the shift is the same for both computation methods. The non-ideality factor is constant $b = 1.38$ for all the analytical curves. The accordance of both methods in this context supports

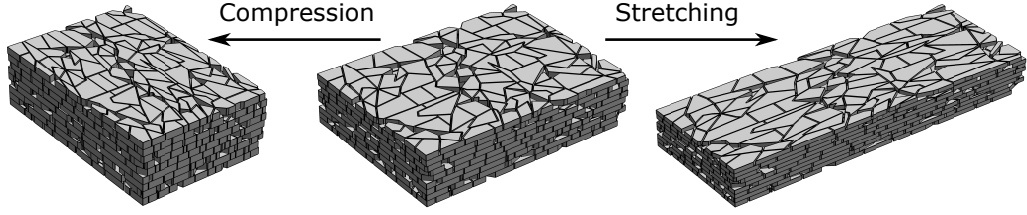


Figure 3.3.6: 3D visualization of anisotropic flake orientation, modeled by deformation of the flakes. Compression results in short edges in current direction. Stretching leads to long edges in current direction.

the mathematical relation that was found in section 3.2.2: An increase in the lateral flake size by a factor f has the same effect as an increase of σ_{out} by a factor f^2 .

A similar effect is found for an anisotropic arrangement of graphene flakes. Since most of the flakes are not round or perfectly square-shaped, there are long and short edges. From the considerations above, it stands to reason that an orientation with the long edge along the direction of current flow is beneficial for the total electrical conductivity. To model an anisotropic arrangement, the flakes are rescaled as shown in Figure 3.3.6. Starting from a regular structure created with the geometry algorithm from section 3.3.2, the flakes are either stretched or compressed in the current direction. The deformation automatically results in a more anisotropic flake arrangement than in the initial geometry. The degree of anisotropy can be adjusted by choosing the appropriate scaling factor. The $\sigma_{\text{tot}}(\sigma_{\text{out}})$ -curves of the structures with anisotropically arranged flakes are shown in Figure 3.3.7. Just like for the in-plane-scaled flakes before, the curves shift on the x -axis. The physical explanation is similar: When the flakes are oriented with the long edge in the direction of current flow, there are fewer overlaps per unit length. Thus, fewer flake-to-flake transitions are required and the path within each flake is maximized. This leads to an earlier increase and saturation of the conductivity. In contrast, when the short edge is oriented in the direction of current flow, the out-of-plane conductivity needs to be larger to compensate the higher number of flake-to-flake transitions.

Note that the anisotropic scaling does not preserve the 2D flake shapes. A deformation of the flakes as well as of the overlaps occurs. Thus, the spreading resistances vary with the orientation of the flakes. In most cases, the spreading resistances increase when the short axis of the flakes is in line with the current flow since larger distances perpendicular to the current direction have to be covered to get from overlap to overlap. Analogously, the spreading resistances tend to decrease when the long axis of the flakes is in

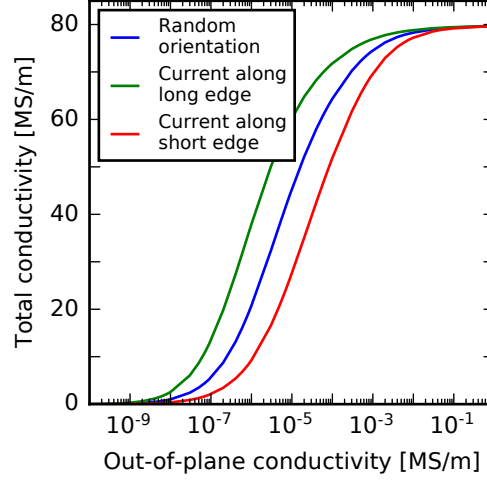


Figure 3.3.7: $\sigma_{\text{tot}}(\sigma_{\text{out}})$ -curves for GCMs with anisotropically arranged flakes computed with FEM.

line with the current flow. Since the effects are difficult to separate, it is hard to attribute a certain shift of the curves on the x -axis to either the variable number of overlaps per unit length, the different overlap areas, or the geometric distortion and thus the spreading resistance. Consequently, a quantitative evaluation of the shift does not make sense here. A qualitative assessment, however, is appropriate.

Homogeneity

Apart from being able to create complex shapes and differently sized flakes, FEM allows for the investigation of the influence of structural homogeneity, an aspect that is of particular importance in a disordered system.

Here, homogeneity is used in the following sense: A geometric structure is considered “homogeneous” when the probability P to find a flake at a given position is constant across the whole structure. When this condition is fulfilled, it follows that P is equal to packing density $P = p$. In contrast to that, in an inhomogeneous structure, the probability P to find a flake at a given position is dependent on the position $P = P(x, y, z)$. Figure 3.3.8 visualizes the concept by comparing three different geometric structures. They are all shown in the top-view perspective, which means that the individual flakes lie in parallel to the paper plane.

Let x and y be the in-plane coordinates and z be the coordinate in the out-of-plane direction of the graphene flakes. The first structure (a) is the model system shown in Figure 3.3.3, which was analyzed in the previous sec-

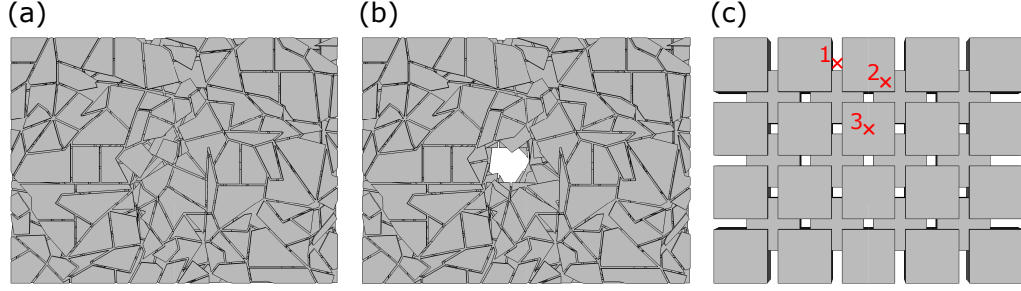


Figure 3.3.8: Top view of a (a) homogeneous structure, (b) inhomogeneous structure, (c) checkerboard structure with three marked positions as described in the main text.

tion. Due to the random nature of the geometry algorithm, the homogeneity requirement is automatically fulfilled and $P = p$. There are no designated regions or positions where the flake coverage is precisely predictable or different from other regions in terms of coverage probability. The second structure (b) is a modified version of structure (a) where the flakes in the middle are removed. Here, the resulting hole is a severe inhomogeneity. It is inherent to the creation process of this structure that in the region around the center position $P = 0$. Most importantly, this does not only affect a single layer, but the whole stack. The larger the volume where by construction $P = 0$, the more severe is the inhomogeneity. The third structure (c) is not disordered but an ordered example of a highly inhomogeneous case. The layers are filled with square flakes arranged in a checkerboard structure. The flakes of neighboring layers are shifted for maximum overlap with as many flakes as possible. Thus, the structure repeats itself after two layers, i.e. it is periodic. However, despite order and periodicity, it is inhomogeneous according to the definition that is used here, because the coverage probability P is position-dependent by construction. In Figure 3.3.8 (c), three (x, y) -positions are indicated. Across all layers (integrated over the z -axis), the coverage probability is $P = 0$ for position 1 in between flakes; $P = 1$ for position 2 on the overlaps, and $P = 0.5$ for position 3 on flakes between overlaps.

In most cases, the degree of homogeneity has a direct effect on the overall conductivity σ_{tot} of a GCM. Macroscopic inhomogeneities such as holes and cracks are expected to degrade the conductivity by interrupting the optimum current path, and this is confirmed by FEA. Figure 3.3.9 shows the limit value of the conductivity in the saturation regime σ_{max} with respect to the packing density. For comparability, it is normalized to the in-plane conductivity of the flakes $\sigma_{\text{max}} \rightarrow \sigma_{\text{max}}/\sigma_{\text{in}}$. In total, 30 systems with varying degrees of homogeneity are investigated. As a reference, the theoretical

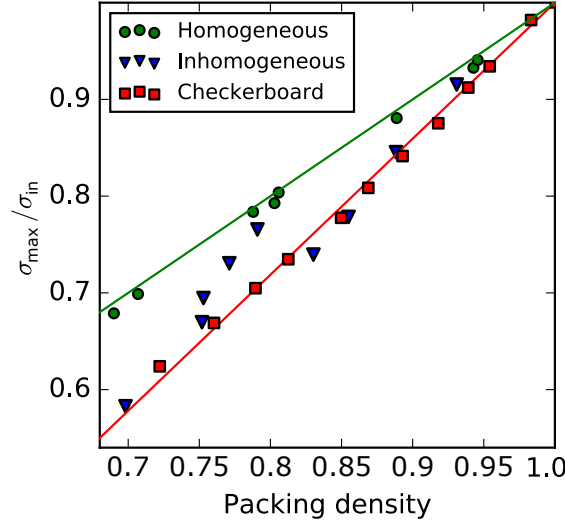


Figure 3.3.9: Normalized limit value of the conductivity in the saturation regime $\sigma_{\max}/\sigma_{\text{in}}$ as a function of packing density. The symbols represent FEA results, the green line corresponds to the theoretical maximum, the red line is a fit for a checkerboard system. Adapted with permission from [114].

maximum given as

$$\sigma_{\max}/\sigma_{\text{in}} = p \quad (3.3.6)$$

is indicated as the green line. The green circles represent homogeneous structures generated with the geometry algorithm. They closely match the idealized conductivity which suggests a refinement of the statement from the previous section: Arbitrarily shaped and oriented flakes can achieve the same electrical conductivity as an idealized ordered system if they are homogeneously distributed. This in turn raises the question, at which point a system can no longer be considered homogeneous enough for optimum conductivity. From the homogeneous model systems, individual flakes are systematically removed to evaluate the robustness to inhomogeneities. It is found that clusters of up to four flakes in two neighboring layers can be removed without a visible reduction in conductivity beyond the effects of the reduced packing density. This corresponds to 4% of the flakes in 20% of the layers, and 0.8% in total. Structures with more or larger defects, including more flakes or spanning more layers are represented by blue triangles in Figure 3.3.9. They clearly deviate from the optimum conductivity. The same holds true for the checkerboard geometries represented by the red squares in Figure 3.3.9. The physical interpretation is straightforward: The inhomogeneities lead to constrictions in the current path. If the current can avoid these constrictions without long detours, there is no visible conductivity reduction. If however

the current path is extended significantly, an additional spreading resistance will result from the geometry alone. The checkerboard geometry is an example of such a case. The systematic spatial flake distribution leads to periodic constrictions, which in turn lead to longer effective current pathways. On top of the geometric effects, current crowding and excessive heating can affect the conductivity, which could be analyzed in electrothermal simulations. The resulting consequences heavily depend on the exact material system and the temperature coefficient of resistance.

The phenomenon of current crowding, i.e. a spatially inhomogeneous current density distribution in the material, is observed even in simple electrostatic FEM computations. Figure 3.3.10 shows the color-coded current density of two GCMs with a similar flake size distribution. They differ in that a single inhomogeneity, a hole, is inserted in one of the two structures. While the geometry in Figure 3.3.10 (a) is homogeneous and consequently exhibits a homogeneous current density distribution, the geometry in Figure 3.3.10 (b) is inhomogeneous. As a result, the current density is varying, with peak values left and right of the hole in the center. The peak values occur as the current is forced to evade the hole, while still trying to take the shortest path. Around the hole, the overall cross-section is reduced, but the amount of current remains the same, which is why current crowding occurs. The minimum current density is found directly in front of and directly behind the hole. The flakes in these locations become less important for current transport as they directly lead up to or follow a region that is blocked for the current. This corresponds to an effective loss of current-carrying material. In some cases, inhomogeneous geometries can be optimized for electrical conductivity, as it would be the case for the flake arrangement used for the analytical description. In this particular case, the periodic structure does not lead to constrictions. But it is an artificially constructed theoretical optimum. The

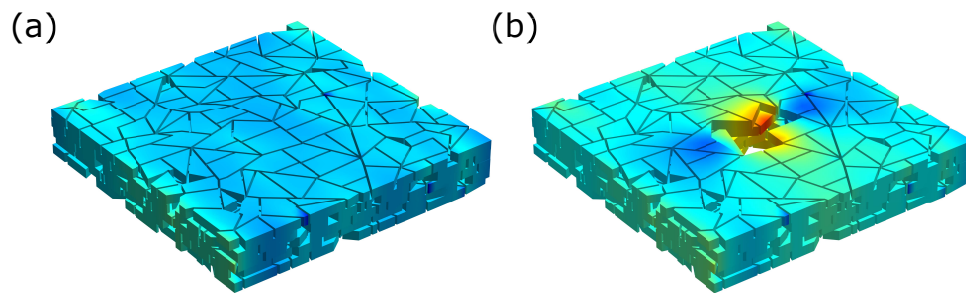


Figure 3.3.10: Color-coded current density distribution in a (a) homogeneous structure and in an (b) inhomogeneous structure. Red color corresponds to the highest current density, dark blue to the lowest.

vast majority of the inhomogeneous geometries is not optimized for electrical conductivity. When it comes to the homogeneous structures on the other hand, FEA suggests that they are all optimized for electrical conductivity. In fact, during the analysis, not a single structure with a homogeneous flake distribution exhibited a conductivity limit that was far off the theoretical maximum.

3.3.5 Computational challenges when modeling GCMs

The majority of the conclusions drawn in the last section is based on the analysis of the electrical conductivity in the saturation regime. This regime is numerically favorable since the extreme conductivity anisotropy between in-plane and out-of-plane values is somewhat mitigated. The computations are thus robust and the results are stable.

Extreme anisotropies however pose a problem for finite element simulations. Since the method is numerical, an increasing instability and lack of convergence is observed for more and more anisotropic systems. This concerns both the geometric anisotropy as well as the anisotropy of physical quantities. Some of the difficulties can be worked around, others are unavoidable. A high-quality mesh is required to achieve convergence and avoid erroneous results. For the geometries in this work, the mesh is generated by an adaptive algorithm implemented in COMSOL. It has been found to be more suitable than the open-source meshing algorithm by FiPy [121] that was also tested. In an adaptive mesh, the resolution is not uniform but tailored to the different parts of the geometry: In geometrically complex regions, the mesh is extremely fine and in simpler regions, e.g. bulky parts, the mesh is rather coarse.

Since GCMs can be disordered, a tetrahedral mesh has to be used. Due to the anisotropy of the geometries, the tetrahedra are anisotropic as well. It is thus unavoidable that some of the tetrahedra are heavily skewed, which is usually a sign of low quality meshing elements. Here however, it is the only possibility to create a suitable mesh. The problem is aggravated by the requirement that the out-of-plane axis of a single graphene flake is covered by more than one layer of tetrahedra – despite the fact that graphene is an atomically thin layer. Otherwise, the steps in electric potential between individual flakes leads to numerical instability or failure of the solving algorithm. An example of an adaptive mesh that meets the aforementioned demands is shown in Figure 3.3.11 (a). It is an enlarged side view of the mesh of the model system depicted in Figure 3.3.3. Each flake is covered by at least three layers of tetrahedra.

To further increase the robustness of the computations, the investigated ge-

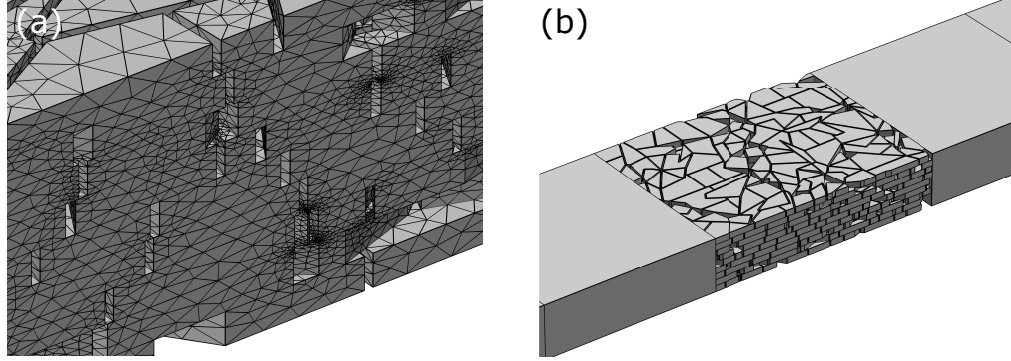


Figure 3.3.11: (a) Meshed layered side-view from the model system. (b) Geometry with attached contacts.

ometry is embedded between long, uniform contacts as shown in Figure 3.3.11 (b). Inside the contacts, current can spread evenly and no spatial inhomogeneities impede the even voltage drop, which provides numerical stability. During the evaluation of the results, the resistance originating from the bulk contacts is subtracted. In addition, the contact length is chosen so large that the spreading resistance caused by the transition from contact to geometry disappears. For the first part of the contacts, a structured mesh is used, which then becomes tetrahedral to adapt to the mesh of the investigated geometry in the center. This has been found to be the most stable and the most efficient meshing technique.

Apart from the geometric anisotropy, there is an anisotropy in electrical conductivity as well. Since $\sigma_{\text{tot}}(\sigma_{\text{out}})$ -curves are of particular interest in FEA, the whole range of this anisotropy is covered. For very small values of σ_{out} , the unphysical phenomenon of surface currents occurs, which is depicted in Figure 3.3.12. If it is favorable, current can pass on the surfaces between flakes of adjacent layers, thus completely avoiding any flake-to-flake transitions and strictly following a 2D path. Surface currents occur for σ_{out} -values below a certain threshold $\hat{\sigma}_{\text{out}}$. At this point, a change in σ_{out} does not have an effect anymore since there is no current flow in the out-of-plane direction. Consequently, the overall conductivity saturates at $\sigma_{\text{tot}}(\hat{\sigma}_{\text{out}})$, which is unphysical (Figure 3.3.14). Figure 3.3.12 shows cross-sections (y - z -plane) of the model system for three different σ_{out} -values. In (a), $\sigma_{\text{out}} < \hat{\sigma}_{\text{out}}$, so that surface currents between the stacked layers are dominant. For $\sigma_{\text{out}} > \hat{\sigma}_{\text{out}}$ as shown in (b), large parts of the current are spread across several flakes. In the saturation regime, depicted in (c), the out-of-plane conductance is so large that the current spreads along the full out-of-plane axis of the layer stack. Since the focus of this work is the electrical conductivity, a volume-related

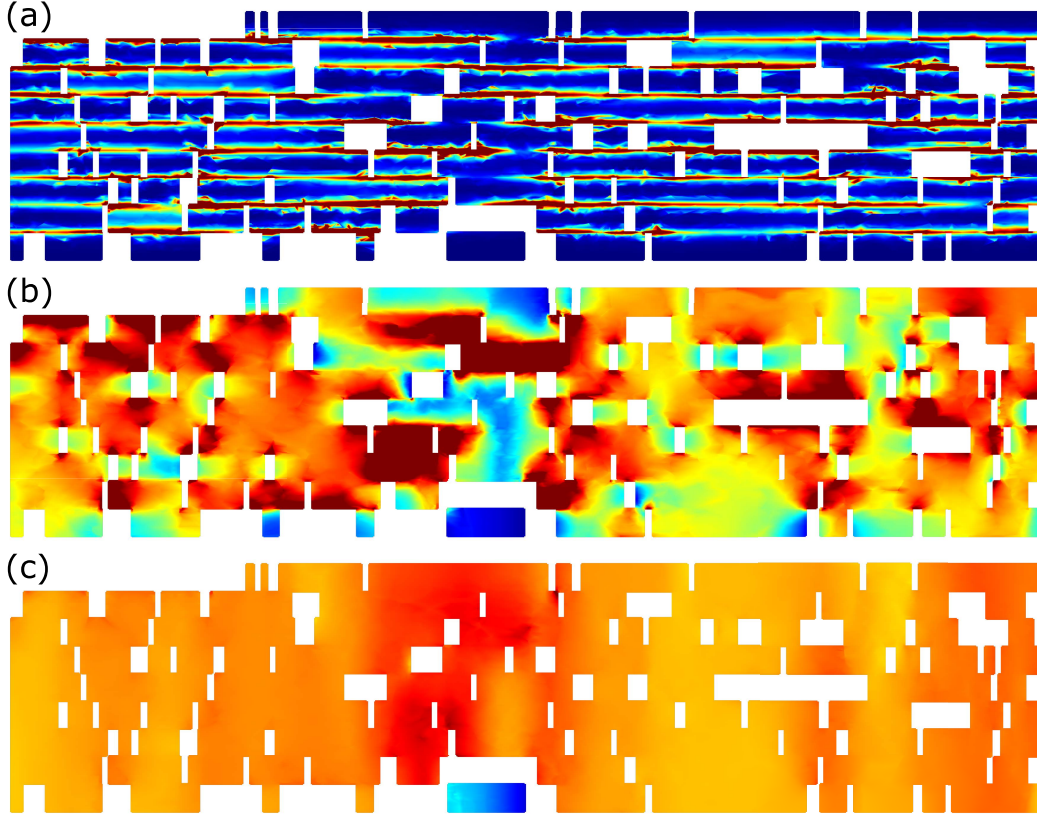


Figure 3.3.12: Color-coded surface currents as seen in cross-sections of a model system for $\sigma_{\text{out}} =$ (a) 10^{-4} Sm^{-1} (b) 1 Sm^{-1} (c) 10^4 Sm^{-1} . Red color corresponds to the highest current density, dark blue to the lowest.

quantity, the situations shown in Figure 3.3.12 (b) and (c) are desired. There are different approaches on how to prevent the unphysical pure surface currents. The most efficient way is to introduce a buffer in between overlapping flakes such that the current is forced to move in the out-of-plane direction. Figure 3.3.13 illustrates the concept, while Figure 3.3.14 shows the result. The buffer layer prevents pure 2D surface currents, which leads to a vanishing conductivity σ_{tot} for very small values of σ_{out} (green line in Figure 3.3.14). However, the $\sigma_{\text{tot}}(\sigma_{\text{out}})$ -curve is also shifted on the x -axis due to the increased out-of-plane distances. To minimize the shift, the buffer layer thickness is reduced to the smallest value that can be modeled with FEM (red line in Figure 3.3.14). The curve shifts left again, but at buffer layer thicknesses smaller than the graphene flake thickness, numerical instabilities start to occur: There are dents and spikes in the saturation regime of the corresponding $\sigma_{\text{tot}}(\sigma_{\text{out}})$ -curves. Via extrapolation to an infinitesimally thin buffer layer, it is found that a $\sigma_{\text{tot}}(\sigma_{\text{out}})$ -curve without surface currents cor-

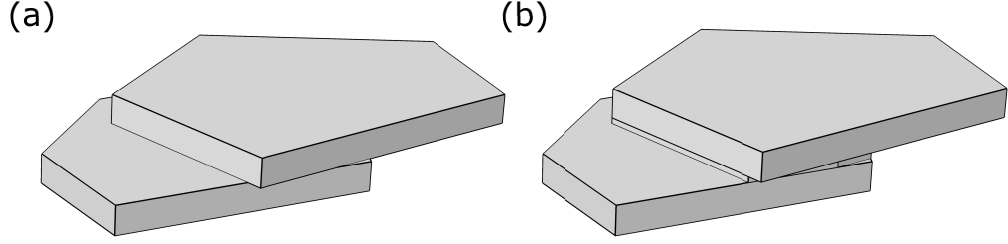


Figure 3.3.13: Two flakes (a) without buffer layer and (b) with buffer layer.

responds to a scaled version of the original curve where the maximum value σ_{\max} remains the same but the minimum value σ_{\min} goes to zero (dashed black line in Figure 3.3.14):

$$\sigma_{\text{tot}} \rightarrow \frac{\sigma_{\max}(\sigma_{\text{tot}} - \sigma_{\min})}{\sigma_{\max} - \sigma_{\min}} \quad (3.3.7)$$

This fits the observation that surface currents only occur for the smallest values of σ_{out} and do not have an effect on the other regimes.

The anisotropic conductivity also has an effect on the numerical solver of the mathematical problem. As explained in section 3.3.3, the solution of a matrix equation is required. Since this is in general a linear problem, it is possible to employ direct solving methods (e.g. Gaussian elimination, Cholesky decomposition, or other lower-upper factorizations). These methods are often more stable and offer higher precision than iterative solvers. However, for a direct solution, the full matrix needs to be stored in the random access memory. This becomes problematic when matrices are extremely large, which is the case for a large number of finite elements. Additionally, if a matrix is of order O , O^2 operations are required to solve the corresponding system with Gaussian elimination. The geometries investigated here contain approximately 10^6 finite elements, so direct solving is extremely time consuming. Last, the matrices of the problem at hand are sparse, i.e. most elements are zero. In this case, a direct solution where each element is considered is highly inefficient. Thus, for the specific case of this work, an iterative numerical solver is faster and less memory-consuming.

At this point, the anisotropic conductivity comes into play again: An iterative numerical solver relies on a preconditioned system of equations. A preconditioner conditions the mathematical problem into a form that facilitates numerical solving. In the highly anisotropic systems analyzed here, the condition number is rather high, which means that the system is very sensitive to small changes in the input. Furthermore, roundoff errors can have a strong impact and lots of preconditioners fail to provide a well-conditioned system. It was found that a solution with the generalized minimal residual

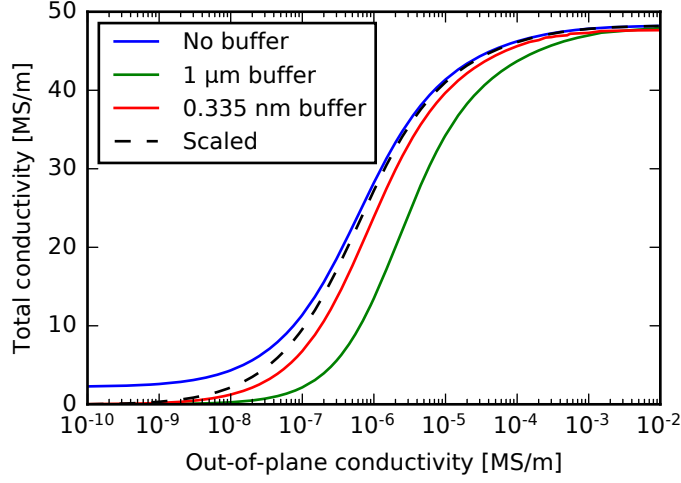


Figure 3.3.14: $\sigma_{\text{tot}}(\sigma_{\text{out}})$ -curves that illustrate the transition from a thick buffer to no buffer in an FEM model system.

method yields the best results in terms of a balance between computation time and robustness. The preconditioning is performed within COMSOL Multiphysics®. To ensure the accurateness of the results, a randomly chosen sample of systems is double-checked with direct solvers.¹

From the discussion in this section, computational expense and numerical stability emerge as the elementary challenges of the FEM approach for GCMs. For reliable and converging simulations, a fine mesh is required, which leads to a large number of finite elements per unit volume. Even with an adaptive mesh, a typical geometry contains $1 - 1.5 \cdot 10^6$ finite elements. Since this translates directly to memory demand and computation time, the system size is limited. At the same time, it is important to make the simulated system as large as possible to ensure convergence, statistical reliability, and numerical robustness. The resulting situation is a tradeoff where memory demand, computation time and system size have to be balanced. To overcome this problem, many of the simulations presented here are performed for several different geometries with the same average parameters. This reduces the statistical error without the necessity to investigate overly large systems.

3.3.6 Summary

FEM is only partially suitable for the analysis of GCMs. Due to the anisotropy of the systems, numerical difficulties arise and the simulation results have

¹The relevant parameters for the FEM simulations are listed in the Appendix 6.3.

to be carefully analyzed to prevent erroneous conclusions. Especially in the regime of low out-of-plane conductance, workarounds are necessary to achieve satisfying results. Across the whole conductivity spectrum, the finite element method is computationally expensive and not particularly robust. However, while FEM is not unreservedly recommended, it is possible to extract a variety of valuable findings from the simulations. This is especially true since the most stable regime, the regime of high out-of-plane conductivity, is the basis for the majority of the conclusions drawn in section 3.3.4.

There are a number of similarities between the results from FEA and the analytical description. The $\sigma_{\text{tot}}(\sigma_{\text{out}})$ -curves have similar shapes and are only slightly shifted with respect to each other. The shift can be compensated with the non-ideality factor b of the analytical model. For all the systems investigated here, b is close to 1, the ideal case. The change in flake sizes has the same effect in both methods, not only qualitatively but also quantitatively. Anisotropically arranged flakes produce a similar shift of the $\sigma_{\text{tot}}(\sigma_{\text{out}})$ -curve. Structural homogeneity, a phenomenon that could not be analyzed within the analytical model, is found to be an additional parameter with a strong impact on electrical conductivity. In this regard, FEA suggests that the theoretical maximum $\sigma_{\text{max}} = p \cdot \sigma_{\text{in}}$ from the idealized analytical model also applies to disordered but homogeneous systems.

The FEA can be extended analogously to the analytical model with regard to new materials or multiphysics. While different geometric and physical input parameters can be adjusted rather easily, the investigation of multiphysical phenomena is computationally more resource-intensive. In conclusion, FEM might not be unconditionally suitable for GCM modeling but it is a helpful tool for analyzing specific characteristics of GCMs. In addition, it can help to crosscheck the results of other simulation methods.

3.4 3D random resistor network model

3.4.1 A simulation method optimized for GCMs

The previous sections have shown that it is difficult to find a suitable method for the simulation of a GCM. In general, the fast simulation methods might be too simplified while the more precise methods can only be used in small model systems. Due to that, a central part of this thesis is the conceptual design and the implementation of a new simulative method, which is tailored to modeling GCMs. This method is presented in the following sections.

To avoid the computational expense of FEM but still achieve a realistic description, a model based on a randomized 3D resistor network is developed.

The method is capable of efficiently simulating systems comprised of tens of thousands of graphene flakes. At the same time, the microscopic properties of the raw material are taken into account. Due to the low computational expense, large systems can be analyzed and statistical methods are employed. With these conditions, a proper connection of the nano- and the macroscale is achieved.

Self-written code can be optimized for any given problem, but it requires proper validation. In the following sections, the method is compared to the FEA and the analytical results. In section 3.4.4.3, a comparison with literature data and in section 4.4, a comparison with experimental results is carried through. The method has been presented in Reference [114] and it has been used for a comprehensive investigation of GCMs in Reference [113]. This section reproduces some of the published results.

3.4.2 Preliminary considerations

Before deciding to develop a new model, many literature-known methods were thoroughly examined and evaluated. Especially in the field of EMAs, a lot of work on composites or nanostructured macro-materials can be found [122, 123, 124]. However, there are two major issues with these approaches. First, microscopic parameters are only taken into account to a small extent or not at all, which is part of the effective medium approach in itself. Hence, since an important part of this thesis is the investigation of quantitative relations between macroscopic properties and microscopic parameters, common approaches such as Bruggeman's effective media theories [122] or McLachlan's general effective media equation [123] are not suitable. Additionally, most of the EMAs were originally focused on percolation behavior and are often only valid close to the percolation regime. When they are applied outside of this range, unphysical results may be the consequence. Examples where EMAs fail can be found in References [125] or [126] where copper-graphene composite films were investigated with Helsing and Helte's effective mean field analysis [124]. In Reference [125], the graphene flake conductivity was determined to be larger than 300 MSm^{-1} and in Reference [126], it exceeds 200 MSm^{-1} . In light of the theoretical maximum conductivity of approximately 100 MSm^{-1} [22, 23] for pristine monolayer graphene, the EMA is highly questionable.

Special attention should be paid to the field of effective media based on resistor lattices [127, 128] where disordered systems are mapped onto ordered lattices to obtain closed form expressions. This approach is also suitable for well-connected networks far away from the percolation threshold and allows for anisotropic conductivities. It has been successfully applied to conductive

metallic nanowire networks [129] and 3D-printed meshes [130]. Both cases are somewhat related to the flake networks investigated here, especially since the analytical model can be interpreted as an effective medium comprised of an ordered resistor lattice as well. While Reference [129] even considers microscopic material parameters, it is only in the form of average or effective quantities. This leads to a commonality of all the EMAs. It is not possible to manipulate individual flakes and thus to study the influence of statistical distributions of physical quantities. The information depth is reduced to effective quantities, which are only valid for specific situations and not necessarily related to microscopic parameters. The network model presented in the following sections provides more flexibility by allowing direct access to the physical properties of every individual flake.

A common simulation method that is often employed to study heat transport is molecular dynamics (MD). Recently, Liu et al. have presented transport calculations and MD simulations to model the electrical conductivity of graphene foams [131]. However, their methods aim at the atomic scale and are thus not suitable for the macroscopic systems investigated in this work. After careful review of many possible simulation methods, it was found that a new approach would be required for GCMs, and a resistor network model has shown to be appropriate.

The assumptions for the network model are similar to the assumptions in the FEA, but a few additional considerations are taken into account. For the same reasons as presented before, GCMs are modeled with high packing densities and rigid polygonal flakes. In both FEA as well as in the analytical model, all the flakes share the same electrical conductivity. In the network model, this changes when physical quantities follow statistical distributions. Previously, connections between flakes within a single layer (edge-to-edge connections) were not considered. This assumption is to be maintained, which is justified as follows: In a GCM, graphene flakes exhibit random shapes and orientations. For proper edge contact with substantial influence on overall current flow, a large number of atoms needs to contribute to electronic transport. Thus, edges need to be perfectly aligned over a significant length. This includes both macroscopic flake alignment as well as the atoms at the edges. The contact between two armchair edges would differ from the contact between an armchair and a zigzag edge. Once there is a slight misalignment, the edge contact is degraded to a point-like contact. Statistically, this is far more likely than perfectly aligned edges. This is why - compared to the areal contact between two sheets where for an overlap of $1\text{ }\mu\text{m}^2$ several 10^7 atoms in each sheet contribute to electronic transport - edges are neglected.

3.4.3 Detailed description of the simulation method

3.4.3.1 Geometry and resistor network generation

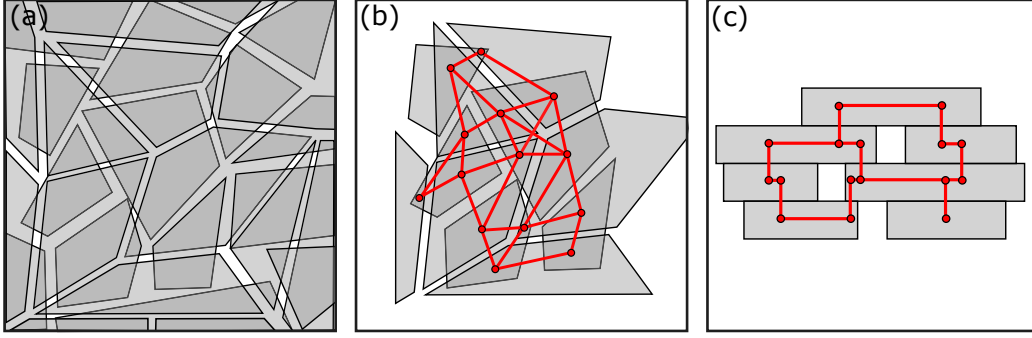


Figure 3.4.1: (a) Top view of two overlapping layers of graphene flakes. (b) Central section from (a) where overlaps are identified, and nodes are generated and connected. (c) Side view of four connected layers. Reprinted with permission from [114].

The geometry for the network model is generated with the algorithm presented in section 3.3.2. It is already optimized to model GCMs and is thus transferable. The geometry algorithm produces 2D layers, which are then given a finite thickness and are stacked to form a 3D object. Subsequently, the 3D geometry is transformed into a graph with nodes and edges. First, the overlaps between flakes of adjacent layers are identified, and their shapes, sizes and positions are determined. At the geometric center of every overlap, two nodes are created; one in the upper flake and another one in the lower flake. Nodes within the same flake or at the same overlap are connected by an edge. In this way, a 3D graph is obtained. The process is depicted in Figure 3.4.1.

Based on the geometric data of the flakes and their overlaps, electrical conductances are assigned to the edges. For out-of-plane connections, the conductance G_{out} is computed according to

$$G_{\text{out}} = \sigma_{\text{out}} \cdot \frac{A_{\text{out}}}{l_{\text{out}}} \quad (3.4.1)$$

with the electrical conductivity between two graphene flakes σ_{out} , the distance between adjacent layers l_{out} and the area of the overlap A_{out} . The interlayer (out-of-plane) connection of two flakes within a GCM can either be a graphite-like stacking or a twisted bilayer graphene (T-BLG) connection. The out-of-plane conductivity of graphite is well-known (333 Sm^{-1} [132]) and

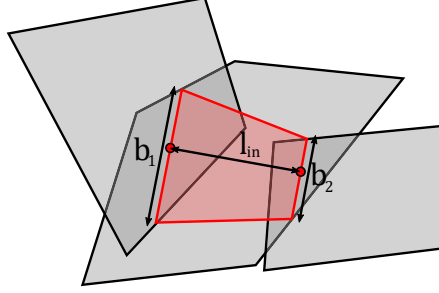


Figure 3.4.2: Exemplary trapezoid (red) to illustrate the calculation of the in-plane flake conductance. Reprinted with permission from [114].

many different forms of bilayer graphene have been investigated as well. In this work, σ_{out} is either treated as a parameter or Perebeinos et al.'s theory on interlayer conductance [133] is applied, as it has been experimentally confirmed by Koren et al. in 2016 [30]. The other parameters in equation (3.4.1) are dictated by the geometry.

The situation is more complex for the in-plane conductances G_{in} since many nodes can be interconnected within a single flake. Current is not limited to the flake area directly between overlaps but it can potentially spread across the entire graphene flake. Furthermore, overlaps are not point-like nodes but objects with a finite surface area. Due to multiple possible overlaps per flake, an accurate description of current flow would require additional methods such as FEM. As discussed in section 3.3.5, this would lead to unacceptable computation times for large structures. Nevertheless, the conductance values G_{in} should be dependent on the individual geometric specifications, namely the total flake area, the distance between connected overlaps, the areas, and the orientations of the overlaps. Current flow from or to large overlaps for example is expected to be more efficient due to a smaller spreading resistance. To solve this dilemma, a combination of simulation methods is employed. In the setup of the electrical network, an empirical parameter is considered that is determined by FEA of several smaller model systems².

As a starting value for the in-plane conductance between two overlaps, the electrical conductance of a trapezoid as depicted in Figure 3.4.2 is chosen. The height of the trapezoid corresponds to the connection line between the node positions, i.e. the centers of the overlaps. The base edges are the intersections of the overlaps and the perpendiculars to the connection line at the

²It should be noted that the considerations for in-plane connections only become necessary when transitioning from 1D-based to 2D-based materials. In nanowire networks or CNT-based macro-materials for example, in-plane conductances can be modeled as 1D, which facilitates the network setup significantly [134, 129]

two nodes. With the base edges being the two terminals, the conductance G_{trap} of such a trapezoidal resistor is given as

$$G_{\text{trap}} = \sigma_{\text{in}} \cdot \frac{t_{\text{gr}} \Delta b}{l_{\text{in}}} \left(\log \left(\frac{b_1}{b_2} \right) \right)^{-1} \quad (3.4.2)$$

with the in-plane conductivity σ_{in} , the thickness of a graphene sheet t_{gr} , the distance between two nodes l_{in} , the lengths of the baselines b_1 and b_2 with $b_1 > b_2$ and their difference $\Delta b = b_1 - b_2 > 0$. Equation (3.4.2) is the exact result for a prism with a trapezoidal base. For $b_1 = b_2 \equiv b_0$, equation (3.4.2) becomes

$$G_{\text{trap}} = \sigma_{\text{in}} \cdot \frac{t_{\text{gr}} b_0}{l_{\text{in}}} \quad (3.4.3)$$

The trapezoidal description considers several important geometrical aspects: The distance between the overlaps, the portion of the flake where the majority of the current is expected to flow, the area of the overlaps and their orientation towards each other. The conductances are normalized for every individual flake such that the total current within a given flake does not exceed the theoretical maximum

$$G_{\text{norm}} = G_{\text{trap}} \frac{A_{\text{flake}}}{\sum_i A_i}. \quad (3.4.4)$$

G_{norm} is the normalized conductance between two overlaps, A_{flake} signifies the area of the flake, and the A_i correspond to the areas of the individual trapezoids in the given flake. A normalization is necessary because for a large number of overlaps in a single flake, the sum of the areas of the trapezoids $\sum_i A_i$ can be much greater than A_{flake} . Without normalization to A_{flake} , the conductances could become unphysically large and allow more current flow than what is physically achievable. For a small number of overlaps on the other hand, the normalization to A_{flake} means that current can spread in the whole flake and is not limited to the region between two overlaps.

During normalization, each trapezoid is equally weighted, irrespective of the amount of current actually flowing through it. This introduces a source of error that needs to be taken into account. An alternative approach that considers current flow requires a self-consistency loop where each connection is re-weighted after the electrical network has been set up and solved. However, in extensive studies it is found that this procedure leads to substantially longer computation times and still unsatisfactory precision, which is why a different method is chosen: the introduction of an empirical parameter k to compensate for the approximations in the network model.

$$G_{\text{in}} = k \cdot G_{\text{norm}} \quad (3.4.5)$$

The parameter k is initially determined by generating test structures and comparing FEA results to the network model. The computation of k only has to be performed once and will be explained comprehensively in the following section. Before that, the construction of the electrical network is demonstrated and the solution of the resulting matrix equation is explained. All the conductances between nodes of the resistor network are compiled into a matrix (G_{ij}) according to nodal analysis. On the main diagonal, for every node i , the sum of all conductances of the edges connected to i is noted:

$$G_{ii} = \sum_j G_{ij}, i \neq j \quad (3.4.6)$$

The off-diagonal elements of the conductance matrix are the negative conductances of the edges between the nodes i and j : $-G_{ij} \forall i, j : i \neq j$. If nodes i and j are not connected, $G_{ij} = 0$. To compute the total electrical conductivity of the GCM, a current through the structure is simulated. To this end, a border region at the edges of the structure is defined, where all flakes are connected to a current source (Figure 3.4.3 (a)). At the points where current is injected, the current density is kept constant. This corresponds to a homogeneous current flow through the bulk of the GCM. Furthermore, current is conserved, i.e. the same absolute amount of current I_{tot} that enters one side leaves the structure on the other side. Apart from the border regions, the external current at every node is zero, in accordance with Kirchhoff's current law. For a total of n nodes, the following matrix form of the current-voltage-equation is obtained:

$$\begin{pmatrix} G_{11} & -G_{12} & \dots & -G_{1n} \\ -G_{21} & G_{22} & \dots & -G_{2n} \\ \dots & \dots & \dots & \dots \\ -G_{n1} & -G_{n2} & \dots & G_{nn} \end{pmatrix} \cdot \begin{pmatrix} \Phi_1 \\ \Phi_2 \\ \dots \\ \Phi_n \end{pmatrix} = \begin{pmatrix} I_1 \\ I_2 \\ \dots \\ I_n \end{pmatrix} \quad (3.4.7)$$

with the conductances G_{ij} , the electric potential Φ_i at node i , and the injected current value I_i at node i . The conductance matrix is singular and an arbitrary reference node where $\Phi = 0$ can be chosen. Subsequently, equation (3.4.7) is solved for the potential vector so that the electric potential at every overlap in the structure is known. To compute the overall voltage drop, two probe surfaces are defined. They are parallel to the side faces of the GCM where current is injected. The probe surfaces are located outside the border region and separated by a distance d that is at least five times as large as the largest graphene flakes (Figure 3.4.3 (a)). The minimum distance guarantees a sufficient number of flakes in between the probes to account for statistical fluctuations. The probe potential is computed by averaging all the

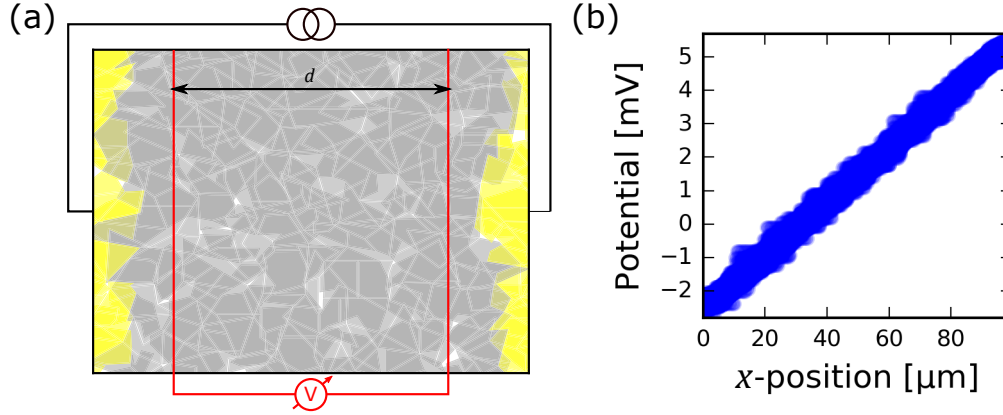


Figure 3.4.3: (a) Top view of a GCM. Current enters or leaves the structure through the yellow flakes at the sides. All the flakes that intersect with the probe surfaces (red lines) are considered for voltage measurement. Reprinted with permission from [114]. (b) Potential along the current direction (x -coordinate) in a structure with 20000 flakes in 20 layers for $\sigma_{\text{out}} = 1 \text{ Sm}^{-1}$.

potentials at the overlaps that intersect with the respective probe surface. The potential difference V between the two probes is similar to the voltage drop measured in a four-point probes configuration. The difference is that not only the surface is probed, but flakes from every layer are considered to capture the bulk and avoid edge effects.

It could be argued that mesh analysis is more realistic than nodal analysis since in many real-world scenarios, a voltage is applied rather than a current. However, the individual meshes are difficult to identify and to separate in the random resistor network model presented here. The task would be time-consuming and inefficient. Most importantly, the electrical conductivity is an inherent material parameter, which is independent of the calculation method that is used. For sufficiently large systems, and outside the border region as defined in Figure 3.4.3 (a), there should not be any difference. In this work, GCM simulations with tens of thousands of graphene flakes and sufficiently large d are performed, and on the macroscopic scale, the voltage drops smoothly and homogeneously across the whole structure. An example is provided in Figure 3.4.3 (b). As in Figure 3.3.4 (b), the apparent thickness of the curve results from the voltage variation in y - and z -direction at the respective x -positions. At the edges, the curve levels off slightly, because current injection and extraction take place at $x > 0$ and $x < 100 \mu\text{m}$ respectively.

The measurement setup described above is chosen since the focus of this work is on intrinsic material parameters and not on contact resistances or probing

effects. The only exception is section 3.4.5, where top contacts are investigated. With the probe distance d , the thickness t , and the width w of the GCM, the total electrical conductivity σ_{tot} can be determined according to

$$\sigma_{\text{tot}} = \frac{I_{\text{tot}}}{V} \cdot \frac{d}{tw}. \quad (3.4.8)$$

The thickness t is given as the total number of 2D layers multiplied by the average layer thickness. The width w corresponds to the vertical axis of the structure in Figure 3.4.3 (a).

3.4.3.2 Determination of the empirical parameter k

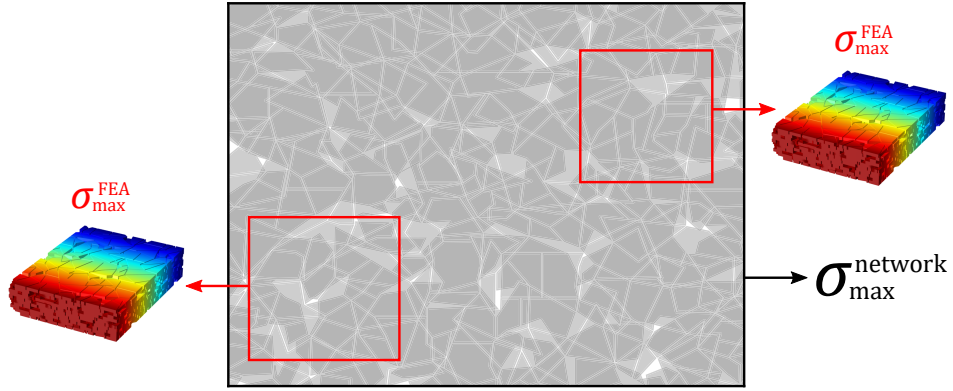


Figure 3.4.4: Illustration of the conductivity limit evaluation. The central structure is generated by the geometry algorithm and evaluated with the network model. Randomly chosen sections are examined by FEA. Reprinted with permission from [114].

The theoretical considerations in section 3.2 have shown that the total conductivity of an idealized GCM σ_{tot} is ultimately limited by the packing density p of the GCM and the in-plane conductivity σ_{in} of the individual graphene flakes according to

$$\sigma_{\text{tot}} \rightarrow p \cdot \sigma_{\text{in}} \equiv \sigma_{\text{max}}. \quad (3.4.9)$$

It is a fundamental upper limit that has to be respected. Since it is the only definitive reference value, the calculation of the empirical parameter k is based on σ_{max} . In section 3.3, it was found that the limit value $p \cdot \sigma_{\text{in}}$ is not only valid for idealized systems but also holds for disordered structures with homogeneously distributed flakes.

With the geometry algorithm described above, large homogeneous 3D geometries with varying packing densities in the relevant range for GCMs $p > 0.7$

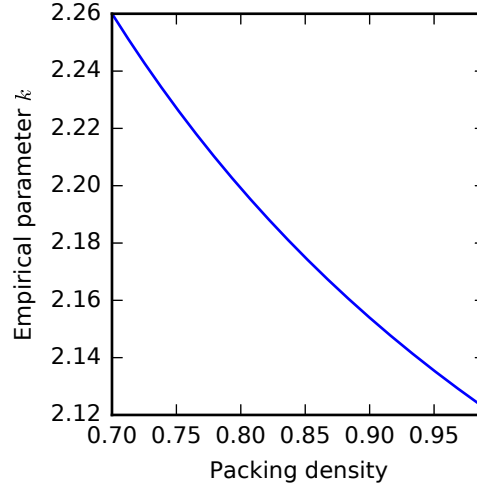


Figure 3.4.5: Functional relationship between the empirical parameter k and the packing density. Adapted with permission from [114].

are generated. For these geometries, and without the inclusion of k , the limit value of the total conductivity $\sigma_{\max}^{\text{net}}$ is calculated within the framework of the network model. For comparison, it is also determined by FEA ($\sigma_{\max}^{\text{FEA}}$) considering randomly selected sections of the large geometries. A large system size is favorable for the network model in order to achieve statistically reliable results. For FEA, the computational expense is much higher so that the calculations are limited to exemplary sections of the complete geometries. The procedure is illustrated in Figure 3.4.4. From every large geometry that is analyzed with the network model approach, at least three sections are evaluated by FEA.

The comparison of the computed quantities $\sigma_{\max}^{\text{net}}$ and $\sigma_{\max}^{\text{FEA}}$ yields the empirical parameter k . For homogeneous systems, the following is required:

$$p \cdot \sigma_{\text{in}} = \sigma_{\max}^{\text{FEA}} = k \cdot \sigma_{\max}^{\text{net}}. \quad (3.4.10)$$

The value of k is dependent on the overall packing density p but does not vary with flake size or other microscopic parameters within the boundaries described in the geometry section. An influence of the out-of-plane conductances can also be ruled out since k is determined from the limit value of the conductivity in the saturation regime. Thus, its inclusion in the in-plane conductances according to equation (3.4.5) is justified.

By evaluating 30 test structures in the range of $0.7 < p < 0.99$, the following

functional relationship is found:

$$k(p) = \frac{\sigma_{\max}^{\text{FEA}}}{\sigma_{\max}^{\text{net}}} = \frac{1.85 \cdot p}{p - 0.127}. \quad (3.4.11)$$

The relationship $k(p)$ is shown in Figure 3.4.5. After the initial determination of k , no further comparison between methods is required for the usage of the network model.

3.4.3.3 Statistical and computational advantages of the network simulation method

As the network model relies on random geometric elements, a minimum number of flakes has to be included in the simulation to obtain statistically reliable results. Furthermore, to treat a simulated GCM as a uniform material and apply equation (3.4.8), the dimensions of the modeled GCM have to exceed a certain threshold to avoid finite size effects. In extensive parameter studies, the necessary conditions for successful modeling with the network method were analyzed. In brief, a minimum number of 20 to 30 layers is required for convergence of the conductivity, depending on the structural details. This corresponds to a thickness of 6 to 10 nm, which is easily fulfilled by real-world GCMs. That also means that surface effects in real materials can be neglected when side contacts are established. The length and width of the simulated GCM should be at least 25 times as large as the average flake length. For statistical robustness, a total of 25000 - 30000 flakes across all layers is required. Important results of the convergence tests are illustrated in more detail in the Appendix 6.1. If extremely inhomogeneous materials are simulated, the system size should be 1.5 times as large. With these parameters, the statistical fluctuation of the resulting total electrical conductivity can be limited to less than 2%. Such a degree of statistical robustness is attributed to the large flake numbers. Numerical robustness on the other hand is provided by the simple mathematical relations that lead to the linear system of equations (3.4.7). Thus, compared to other simulation methods, the statistical reliability of the data is higher and a fallacy of insufficient sample size can be avoided more easily.

During algorithm analysis, it is found that the geometry generation and the connection of the nodes are the most time-consuming components. Only for geometries with more than 50000 flakes the solution of the matrix equation becomes dominant. All of these processes can be parallelized efficiently. The geometry generation and the flake connection represent a so-called “pleasingly parallel problem”, i.e. the individual tasks can be performed completely independent of each other. The layers of the geometry are created individually

without the need of communication between the different processes. The same holds true for the in-plane connections of the nodes in each layer, while the out-of-plane connections can already be set during the node creation. The conductance matrix is sparse, since only flakes in adjacent layers can be connected. For the solution of the corresponding matrix equation, a variety of efficient algorithms exists. The parallelization of this process is possible (e.g. with open source solutions such as MPI for Python [135]), but not necessary for the systems investigated in this work. If the minimum layer lengths and widths are applied, run-time analysis shows that the complete network simulation method scales according to $\mathcal{O}(m^{7/2})$ with the number of flakes m . For a constant number of layers and increasing length and width of the structure, the method scales according to $\mathcal{O}(m^2)$, as shown in Figure 3.4.6. The two types of scaling behavior arise from the fact that many operations in the algorithm are performed layerwise. Thus, an extra layer always adds an additional iteration in a loop or requires an additional parallel process, which is not the case for the extension of existing layers. As a consequence, an increase in the layer number is computationally more expensive.

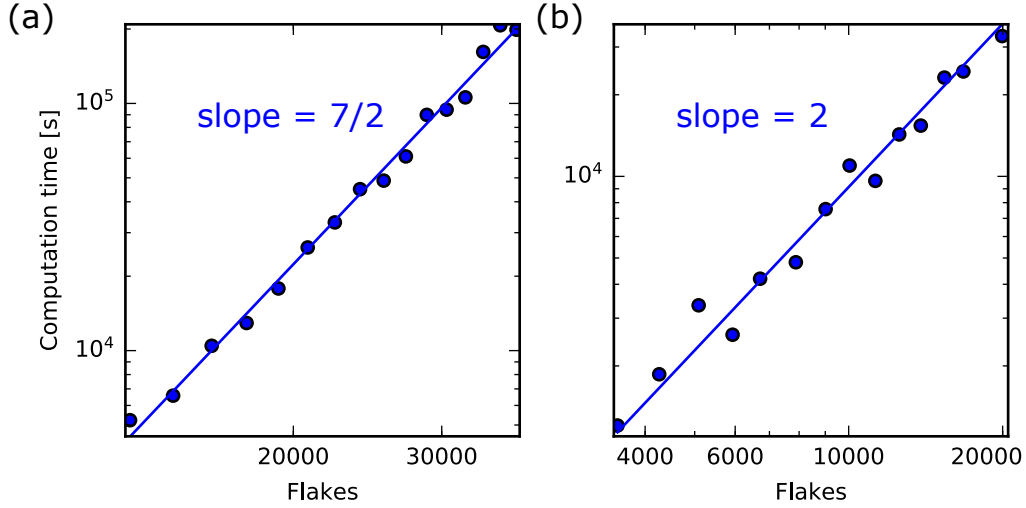


Figure 3.4.6: Run-time analysis for (a) an increasing amount of layers with fixed side lengths, and (b) increasing side lengths of a fixed amount of layers. The circles correspond to simulated data points, the lines represent a linear fit. The slope of a given linear function yields the respective scaling behavior.

3.4.4 Results and discussion

3.4.4.1 General characteristics and comparison to previous approaches

As with the previous approaches, the characteristic $\sigma_{\text{tot}}(\sigma_{\text{out}})$ -curve is investigated first. Figure 3.4.7 (a) shows the averaged curve of ten structures, each one with 30 layers and a total of > 55000 flakes. The geometric parameters of the flakes are extracted and averaged, and subsequently plugged into the analytical model (equation (3.2.14)). The resulting curve is shown in direct comparison to the network model in Figure 3.4.7 (a). For reference, an FEM curve computed with similar average parameters is plotted as well.

The agreement between the curves is evident. The three regimes discussed in sections 3.2.2 and 3.3.4 are found in all three methods, and only a slight shift on the x -axis is visible. The saturation value is the same for all three curves. The analytic curve exhibits the largest slope, followed by the network model, and then the FEM-curve. As argued in section 3.3.4, the fact that the curves from the network model and from FEM are not as steep as the analytical curve can be explained with the higher degree of geometric complexity. The shift of the analytical curve on the x -axis can be compensated with the non-ideality factor b as introduced in equation (3.2.20). In the specific case of Figure 3.4.7 (a), b is determined to be 1.29, and in general, it ranges between 1 and 1.7. These values, which are close to the ideal case 1.0, quantify the accordance that is already visually apparent.

In sections 3.2.2 and 3.3.4, an identical scaling behavior for flake sizes is observed across different simulation methods. Hence, the phenomenon is investigated with the network model as well. Figure 3.4.7 (b) shows the $\sigma_{\text{tot}}(\sigma_{\text{out}})$ -curves of a fixed flake configuration that is scaled to different sizes. As in the previous studies, the flake thickness is retained but the in-plane dimensions are scaled with a factor f . The corresponding analytical curves are computed with a fixed non-ideality factor $b = 1.51$ and displayed as dashed lines. The scaling produces identical results: An increase in the lateral flake size by a factor f has the same effect as an increase of σ_{out} by a factor f^2 . The accordance of all three simulation methods regarding the scaling - despite the different degrees of geometric and computational complexity - is a strong argument for the proposed mathematical relationship.

The same systematic shift on the x -axis is observed when the network model is used to analyze not a fixed configuration with scaled flake sizes, but a variety of different configurations, each one with another average flake size. Irrespective of the exact size distribution, the curves shift according to the mean flake area: the larger the flakes, the further the shift toward smaller

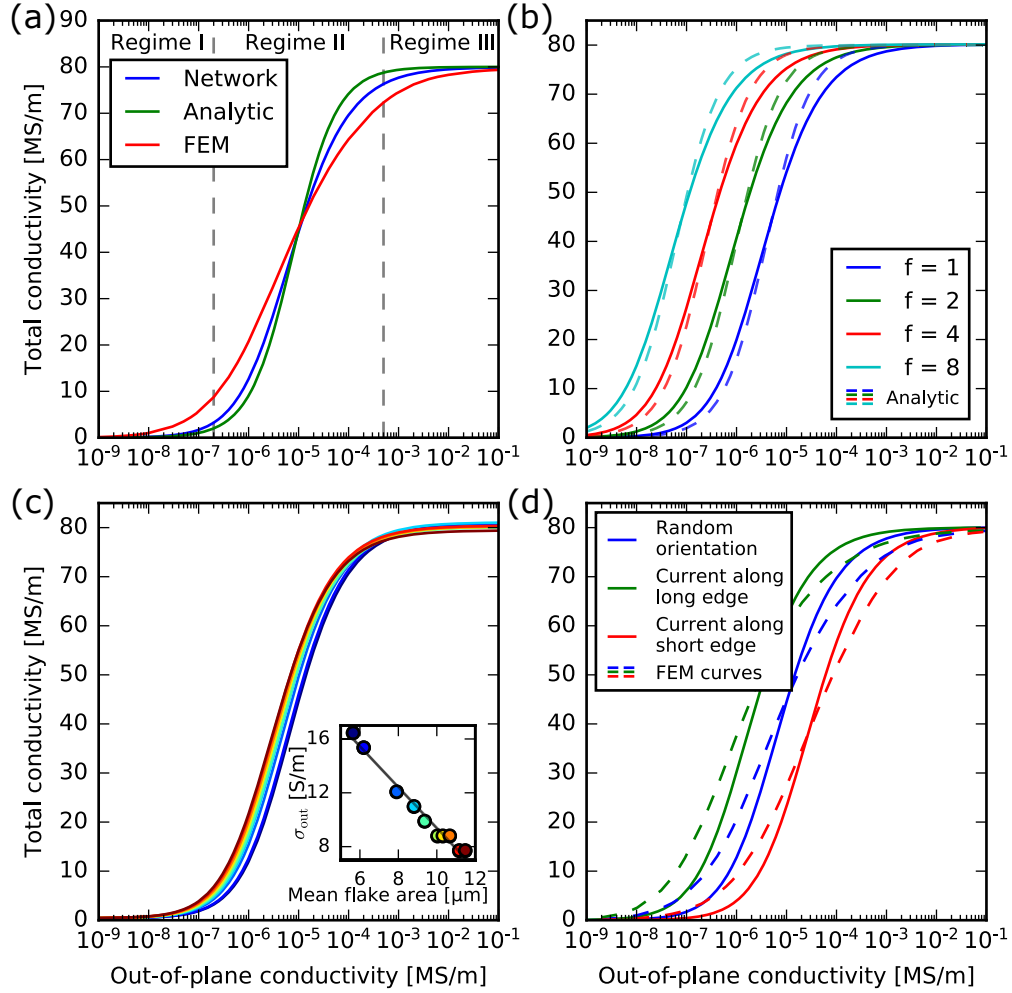


Figure 3.4.7: (a) Typical network model $\sigma_{\text{tot}}(\sigma_{\text{out}})$ -curve compared to the analytical model and an exemplary FEM calculation. (b) Flake size scaling effects on the $\sigma_{\text{tot}}(\sigma_{\text{out}})$ -curve for the network model (solid lines) and the analytical model (dashed lines). (c) $\sigma_{\text{tot}}(\sigma_{\text{out}})$ -curves for different flake size distributions. Inset: σ_{out} at the half-maximum as a function of the average flake area. Dot colors correspond to the curve colors in (c). The gray line is a guide to the eye. Adapted with permission from [113]. Copyright 2018 American Chemical Society. (d) Scaling in anisotropically ordered geometries in the network model (solid lines) compared to FEA (dashed lines).

out-of-plane conductivities. The phenomenon is illustrated in Figure 3.4.7 (c), while different size distributions are shown in the Appendix 6.2. In the inset, the value of σ_{out} at 50% of σ_{max} is plotted versus the mean flake area of the corresponding distribution. Here, a systematic decrease with mean flake area is observed. The analysis suggests that for flake sizes which follow the guidelines from section 3.4.3.3, the material system is self-averaging. Therefore, it is not necessary to consider the exact size distribution but the average flake size suffices as an input. When flake sizes exceed the abovementioned boundaries, for example when they become similar in size as the GCM itself, a different behavior is expected. This scenario, however, is far from realistic given the current state of the art in graphene flake and GCM production.

To complete the comparison with the FEA results, an anisotropic arrangement of graphene flakes is investigated with the network model. The geometries are prepared in the same way as in section 3.3.4, i.e. a regular geometry is stretched or compressed along the x -direction³. Due to the large system sizes in the network model, the factor of stretching or compression s can be interpreted in a physical way. For the regular geometries, flakes are randomly shaped and oriented, so for large enough flake numbers, the average flake length in x -direction is the same as the average flake length in y -direction. Stretching the x -direction by a factor of s simply corresponds to flakes which are arranged in such a way that their average x -length is s times as large as their average y -length. Figure 3.4.7 (d) compares the effect of anisotropic ordering in the network model (solid lines) to the FEM computation (dashed lines). The shifting of the curves occurs for the same reasons as explained in section 3.3.4, and the magnitude of the shift is nearly identical as well. The slight difference can most likely be attributed to the fact that the geometries of the FEM case and the network model are not identical. Consequently, the effect of the deformation of the overlaps differs as well, resulting in a slightly different shift on the x -axis. For severe geometric deformations, the empirical parameter k does not hold anymore and the curves have to be renormalized to meet the intended maximum.

The network simulation method agrees with the FEM approach and the analytical method in most regards. The qualitative characteristics are in fact identically reproduced, however on a much larger scale with many more flakes compared to the FEM approach and higher complexity compared to the analytical model. Quantitative differences can be explained coherently. Thus, the network approach can be considered a suitable simulation method for GCMs and its advantages will be exploited in the following sections.

³As in previous sections, x and y represent the in-plane directions.

3.4.4.2 Statistical distributions of physical quantities

In a step towards more realistic GCMs, statistical distributions instead of fixed values for σ_{in} and σ_{out} are considered. Figure 3.4.8 (a) depicts the results for a fixed flake configuration with $p = 0.8$, where the out-of-plane conductivity is constant for all flakes but the in-plane conductivities follow Gaussian distributions f_G according to

$$f_G(\sigma_{\text{in}}) = \frac{1}{\sqrt{2\pi s_{\text{in}}^2}} \exp\left(-\frac{(\sigma_{\text{in}} - \bar{\sigma}_{\text{in}})^2}{2s_{\text{in}}^2}\right). \quad (3.4.12)$$

The distributions share the same mean $\bar{\sigma}_{\text{in}} = 50 \text{ MSm}^{-1}$ but the standard deviations vary $s_{\text{in}} = 0.001 \bar{\sigma}_{\text{in}}, 0.1 \bar{\sigma}_{\text{in}}, 0.3 \bar{\sigma}_{\text{in}}, 0.5 \bar{\sigma}_{\text{in}}$. For each value of the standard deviation, the results of five model systems are averaged. As the limiting case - an infinitely large standard deviation - the results for a uniform distribution with $0 < \sigma_{\text{in}} < 100 \text{ MSm}^{-1}$ are also shown.

A clear trend can be identified: the broader the distribution of the in-plane conductivities, the lower the total conductivity. For a uniform distribution of σ_{in} between 0 and 100 MSm^{-1} , the total conductivity in saturation is reduced by approximately 20% compared to a constant σ_{in} of 50 MSm^{-1} . In total, more than 20 different conductivity distributions were investigated, all of which lead to the same result: The maximum total electrical conductivity is only obtained for a nearly homogeneous in-plane conductivity across the whole GCM.

The situation is fundamentally different for σ_{out} as is shown in Figure 3.4.8 (b). For a given flake configuration, a fixed value $\sigma_{\text{in}} = 100 \text{ MSm}^{-1}$ is chosen and Gaussian distributions are assumed for the out-of-plane conductivities. The distributions have identical mean values $\bar{\sigma}_{\text{out}}$ and varying standard deviations $s_{\text{out}} = 0.1 \bar{\sigma}_{\text{out}}, 0.2 \bar{\sigma}_{\text{out}}, 0.3 \bar{\sigma}_{\text{out}}, 0.5 \bar{\sigma}_{\text{out}}, 2.0 \bar{\sigma}_{\text{out}}$. For each value of the standard deviation, the results of five model systems are averaged. For $s_{\text{out}} \leq 0.5 \bar{\sigma}_{\text{out}}$, the curve hardly changes and only exhibits a slightly delayed ascent. However, for $s_{\text{out}} = 2.0 \bar{\sigma}_{\text{out}}$, the curve rises earlier. It converges with the other curves when the saturation regime is approached, but in the transition regime, a broad distribution of σ_{out} is beneficial for the overall electrical conductivity. Physically, this means that in a GCM, highly conductive flake overlaps are decisive for the total conductivity. They can overcompensate poorly conductive connections and are thus more effective than a homogeneous out-of-plane conductivity in the whole GCM. Furthermore, the total conductivity in the saturation regime is not reduced by the statistical distribution of σ_{out} .

In the sense of an effective medium, the net effect of statistically distributed quantities is a change in the effective quantities. For instance, a distribu-

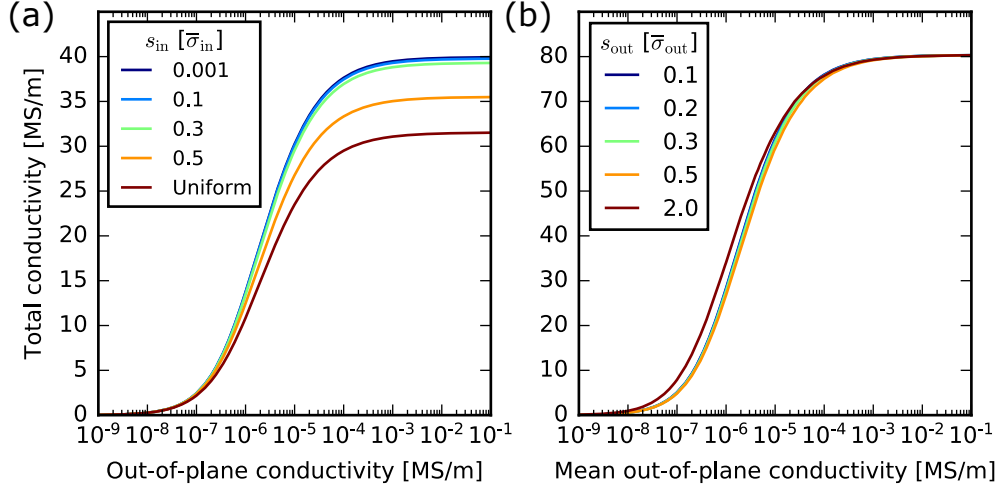


Figure 3.4.8: $\sigma_{tot}(\sigma_{out})$ -curves with (a) statistical variation of σ_{in} and (b) statistical variation of σ_{out} . Adapted with permission from [113]. Copyright 2018 American Chemical Society.

tion of the σ_{in} -values corresponds to a lower effective in-plane conductivity. Analogously, a widely spread range of σ_{out} -values results in a higher effective out-of-plane conductivity.

Besides Gaussian distributions, the occurrence of a bimodal conductivity distribution is also realistic; e.g. a portion of the flakes is conducting while the other portion is not. Such a condition can be the result of an incomplete reduction of GO, or the addition of nano-sheets other than graphene to functionalize the GCM. To analyze the influence of non-conductive flakes in the conducting network, 180 different structures are modeled and evaluated. The portion of non-conducting flakes varies between 0.005 and 0.5 and the packing densities are either $p = 0.7$, $p = 0.8$, or $p = 0.9$. The results are shown in Figure 3.4.9 (a) where the maximum conductivity in saturation σ_{max} (normalized to 1) is plotted versus the share of the non-conducting flakes θ . The computations are plotted together (transparent symbols) and averaged (solid symbols) since the behavior is the same, irrespective of the packing density.

For a share of non-conducting flakes that is below the critical share $\theta_c = 0.1$, σ_{max} decreases nearly linearly with θ , with a slope of -2.2 . Around the critical share of $\theta_c = 0.1$, the conductivity drops substantially by several orders of magnitude. For shares greater than θ_c , the conductivity is expected to follow a power law, as it is typically found in percolation theory [123].

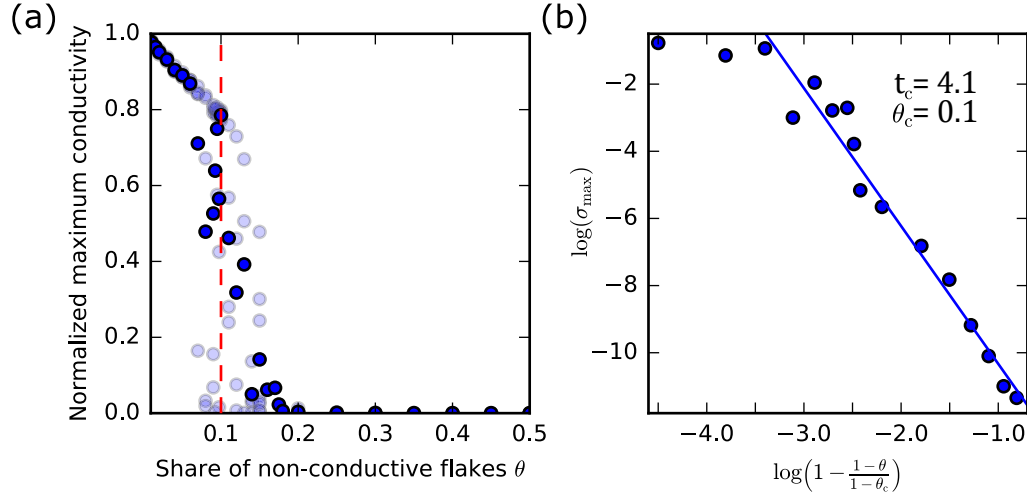


Figure 3.4.9: (a) Normalized maximum conductivity as a function of the share of non-conducting flakes. The red dashed line marks the critical share $\theta_c = 0.1$. Transparent symbols represent simulated data points, opaque symbols represent averaged values. (b) Fit (blue line) of equation (3.4.13) to the averaged data points from (a).

It has the following form:

$$\sigma_{\max} \propto \left(1 - \frac{1 - \theta}{1 - \theta_c}\right)^{-t_c}, \quad (3.4.13)$$

where θ_c is the critical share, and t_c is the critical exponent. Both quantities depend on the dimensionality of the percolating elements, their shapes, and their arrangement. They can also depend on the host material [123]. Figure 3.4.9 (b) shows the fit of equation (3.4.13) to the averaged data points from (a). With a least squares fitting routine, the parameters $\theta_c = 0.1$ and $t_c = 4.1$ are determined.

In the literature, percolating 2D elements have been studied before as conductive elements in non-conductive matrices: Zhang et al. measured $\theta_c < 0.01$ and $t_c = 4.22$ for graphene flakes placed randomly in a 3D insulating host material [136]. Tkalya et al. investigated the percolation threshold of similar systems and found critical shares between 0.01 and 0.023 [137]. Pang et al. created segregated structures, where graphene was not homogeneously dispersed, but assembled at the interfacial regions of polymer particles, which lead to critical shares as low as $\theta_c = 0.0007$ and a critical exponent of $t_c = 1.26$ [138]. The quantities θ_c and t_c are very specific to the investigated system [123]. Therefore, the literature values are expected to differ from the results obtained here. For GCMS, a higher θ_c is expected due to the flat, layered

arrangement. It leads to a higher number of 2D elements that are required to span the full out-of-plane dimension of the system. Additionally, the perfectly homogeneous distribution of non-conductive elements among the conductive ones favors a higher θ_c , since the percolating elements are always at maximum distance from each other.

From an application point of view, the critical share θ_c is a highly relevant quantity. It signifies the absolute limit of non-conductive elements in a GCM before the material cannot be used as a conductor anymore. The network model suggests that the critical share of $\theta_c = 0.1$ is universal for the geometries investigated here as it is independent of packing density, flake size, or conductivity. Note however that this study investigates the worst case scenario for the total conductivity, which is a homogeneously dispersed non-conductive phase. If the low-conductivity and high-conductivity phases were spatially separated, a continuous high-conductivity channel would form inside the material. In that case, the total conductivity would be given by the share θ_{hi} and the conductivity σ_{hi} of the high-conductivity phase $\sigma_{tot} = \theta_{hi} \cdot \sigma_{hi}$.

The physical interpretation of the bimodal conductivity distribution is closely linked to the homogeneity investigations in section 3.3.4. The non-conductive flakes have the same effect as holes in a conductive structure. They act as non-conductive inhomogeneities and reduce the total conductivity when there are enough of them. In FEA, the first severe effects are observed when close to 1% of the flakes are removed. In the network model, this is similar. At a share of 0.5% non-conductive flakes, the overall conductivity averaged over many different structures is reduced by approximately 0.5%, which can be explained by the loss of current-carrying material alone. At a share of 1% non-conductive flakes however, the averaged overall conductivity is reduced by 1.9%. This is the result of both the reduction of current-carrying material as well as the spatial inhomogeneity of the current path due to the non-conductive flakes. Once more, it is found that a homogeneous flake distribution is best for maximizing the electrical conductivity.

3.4.4.3 Comparison with experimental results from the literature

As a test of the network model, published data is compared to simulation results. Information on raw material parameters is used as input for the simulation and the resulting computed conductivity is compared to the experimentally obtained value. The main difficulty lies in identifying publications where sufficient information is presented to run a simulation. While it is relatively easy to measure flake sizes, densities, or the total conductivity of a GCM, the determination of in-plane and out-of-plane conductivities is challenging. However, due to their structural similarity, GICs often repre-

| Stage | Experiment σ_{tot} [MSm ⁻¹] | Simulation σ_{tot} [MSm ⁻¹] |
|-------|--|--|
| 1 | 12.3 | 9.88 |
| 2 | 14.4 | 14.9 |

Table 3.1: Comparison of measured and simulated total conductivities. The experimental data is taken from Reference [65].

sent a suitable substitute for doped GCMs. In Reference [46], in-plane and out-of-plane conductivities of a large number of GICs are compiled.

In 2017, Zhou et al. presented highly conductive potassium-intercalated graphene films in the stage-1 (C₈K) and stage-2 (C₂₄K) configurations [65]. The nomenclature is analogous to GICs: Stage-1 refers to potassium dopants between each layer of graphene whereas stage-2 corresponds to potassium dopants between every two layers of graphene. Comparing the density of their undoped graphene film with a graphite single crystal, a packing density of $p = 0.78$ is found. For production details, they reference a previous publication, from which an average flake size of at least 35 μm in diameter is deduced [73]. Note that this is a conservative estimate and should be regarded as a lower bound. The group also presented dispersions with average flake diameters up to 108 μm [73]. For the in-plane and out-of-plane conductivities, the measured values in potassium-intercalated graphite in stage-1 (C₈K) and stage-2 (C₂₄K) configurations are taken from the literature [46, 89]. However, the less densely packed graphene films from Zhou et al. seem to offer more room for dopants than a perfect crystal: The increase in film thickness after doping is smaller than for potassium-intercalated graphite [65, 89].

Considering all these aspects, ten different flake configurations are modeled for each stage and the average total conductivity of the GCM is computed. The results are compiled in Table 3.1. The simulations are consistent with the experimental results. For stage-2, a difference of 3% is observed, for stage-1 the difference amounts to 20%. The deviation for stage-1 may result from the fact that the stage-1 film is not identical to a perfect stage-1 GIC. Murray and Ubbelohde found an in-plane conductivity of $\sigma_{\text{in}} = 10.9 \text{ MSm}^{-1}$ for stage-1 C₈K [89], which is already lower than the total conductivity of 12.3 MSm^{-1} measured by Zhou et al. This could indicate the difference of the two structures. Nevertheless, the accuracy of the network model demonstrates the power of this simulation method.

In the above type of prediction of electrical conductivities, only individual data points are generated. A more meaningful test of the model is performed when the flake-size dependent conductivity of a GCM is analyzed, since a full curve can be compared to several data points. A thorough literature review

revealed four different publications, which are suitable for this analysis (References [116, 117, 80, 72]). They all present an investigation on the influence of flake sizes on the electrical conductivity of pure graphene films.

For each film, the average flake size, the total conductivity, and the density are considered as input parameters for the simulation. The in-plane and out-of-plane conductivities are then determined with a fitting routine. They are not modeled as statistical distributions but as effective quantities, which are constant in the whole GCM. The validity of this approach is a direct result from the findings on self-averaging in section 3.4.4.2: When a physical quantity is distributed statistically in a sufficiently large system, it can also be modeled as a constant effective quantity. Analogously, the average flake sizes are reproduced in the simulation instead of the exact flake size distributions. Furthermore, it is assumed that all the films prepared in the same way share the same in-plane and out-of-plane conductivity as they originate from the same raw material and were subject to the same process steps. In some cases, data has to be extracted from plots, and in References [116, 117, 80] where the density is not explicitly provided, a constant packing density $p = 0.8$ is assumed. For each set of graphene films, ten exemplary structures are modeled with the network simulation, and the resulting electrical conductivity is averaged. Figure 3.4.10 shows the simulated conductivity curves with respect to the average flake size, together with the data points from the different publications. In Figure 3.4.10 (a), two curves and two sets of data points are shown because the results from two different GO reduction methods could be extracted.

While the data points seem to follow the trend that the simulation suggests, it is clear that apart from Reference [116], shown in Figure 3.4.10 (a), there are too few data points for a proper comparison. For (b)-(d), it would also be possible to fit a straight line through the measured values. Furthermore, measurement errors are not reported in any of the publications. And since some of the data is extracted from plots, an additional source of error is introduced.

Reference [116] (Figure 3.4.10 (a)) seems to provide the most appropriate data for a sound analysis for several reasons: First, the data points are widely spread and cover over two orders of magnitude in flake size. This allows for a clear test of the model since the shape of the curve becomes more characteristic for a larger range of flake sizes. Second, Reference [116] is the only one of the four publications where actual flake areas are published and not flake diameters. Although flake areas can be estimated from flake diameters, the data from Reference [116] is more precise. Third and most importantly, Reference [116] is the only publication that presents four data points for each of two different preparation methods. Out of all the presented

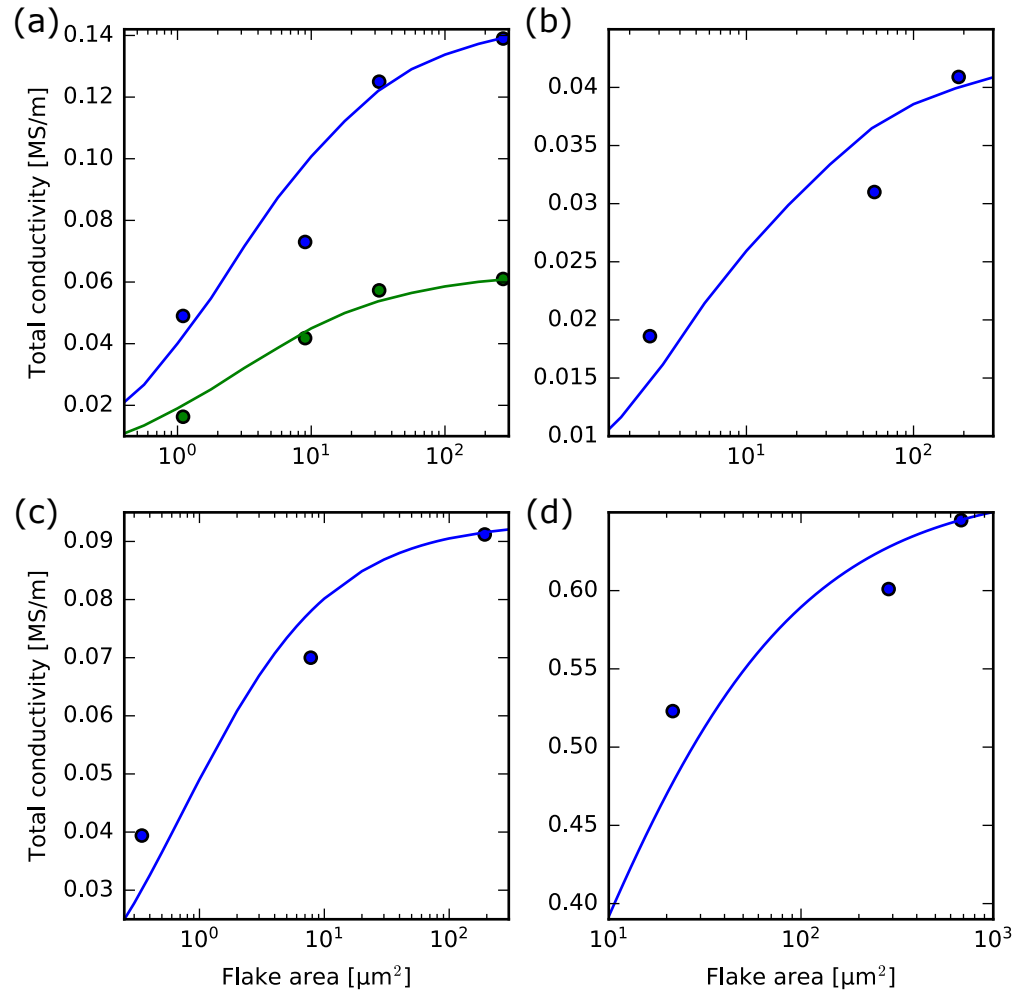


Figure 3.4.10: Total conductivity of graphene films in the literature as a function of the average flake area. The solid lines correspond to the simulation, the data points are taken from References (a) [116] (b) [117] (c) [80] (d) [72]. In (a), the blue line and data points correspond to thermally reduced films, whereas the green line and data points correspond to a chemical reduction.

publications in Figure 3.4.10, it provides the most suitable dataset, and it closely matches the prediction of the network model.

The next study is based on the observation that the fitting routine for the simulated curves yields out-of-plane conductivities on the order of 0.01 Sm^{-1} - 0.1 Sm^{-1} for the cases shown in Figure 3.4.10. Considering the in-plane conductivities as fixed in each batch, the individual out-of-plane conductivities are determined as the last free parameter. In Figure 3.4.11 (a), the film conductivities are plotted with respect to these out-of-plane conductivities. For better comparison, the conductivities in each batch are normalized to 1.0 as the maximum conductivity. As a point of reference, the out-of-plane conductivity of T-BLG is indicated as the gray area [133, 30]. It is expected to be on the same order as the out-of-plane conductivity in GCMs when there are sufficient turbostratic flake-to-flake connections. The dashed line indicates the average out-of-plane conductivity $\sigma_{\text{out}} \approx 0.1 \text{ Sm}^{-1}$ obtained from the fit. 82 % of all data points are located in the range between 0.01 Sm^{-1} and 0.2 Sm^{-1} . The spread is not systematic though: A low out-of-plane conductivity can correspond to a high total conductivity and vice versa. The fitted out-of-plane conductivities range around the lower end of T-BLG conductivity. Considering that the T-BLG values are measured and simulated for the van-der-Waals distance of 0.335 nm between graphene layers, the results are physically coherent. In the macroscopic GCM, the interlayer distance is expected to deviate from the optimum case so that on average, the distance is greater than 0.335 nm. An increased distance subsequently leads to a lowered out-of-plane conductance compared to ideal T-BLG. For further studies, the average value $\sigma_{\text{out}} \approx 0.1 \text{ Sm}^{-1}$ can be used for estimations when the data is incomplete.

In Figure 3.4.11 (b), the normalized film conductivities are plotted with respect to the corresponding flake areas. Again, the in-plane conductivities are assumed to be constant within each batch as they are determined by the raw materials and the fabrication process. The general qualitative trend that larger flake sizes lead to higher electrical conductivities is not surprising. It is noteworthy though that for the data presented here, a minimum flake area in the order of $10 \mu\text{m}^2$ is required for a material to reach more than 50% of its potential. In the analytical model, this matches well with the predicted average out-of-plane conductivity of $\sigma_{\text{out}} \approx 0.1 \text{ Sm}^{-1}$. When $100 \mu\text{m}^2$ or more are reached, the flake size has been fully exploited.

At present, the amount of data in the literature that can be used to test the network model is rather small. The analyses that can be conducted however show strong agreement between the simulation and the experimental data. This holds true for individual conductivity predictions as well as the flake-size dependent conductivity.

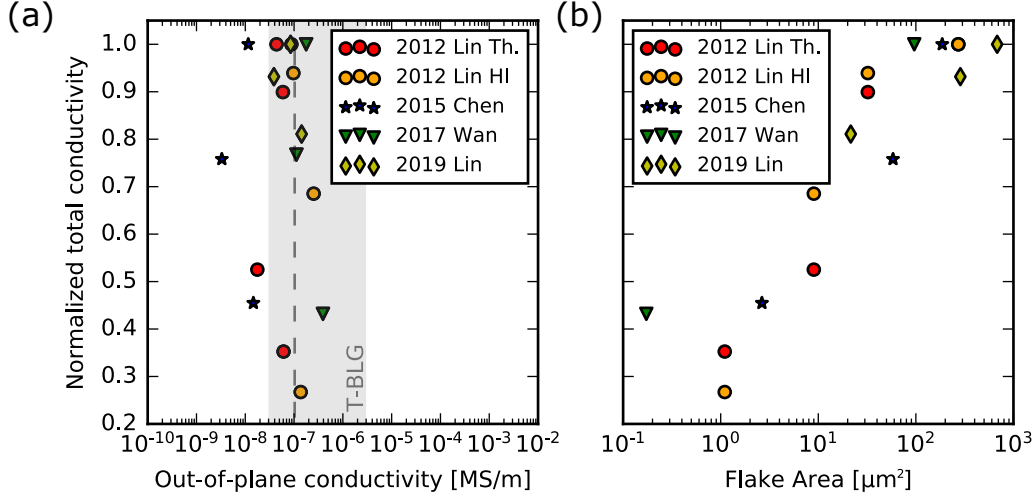


Figure 3.4.11: (a) Normalized graphene film conductivity from the literature versus fitted σ_{out} . The shaded area is the σ_{out} -range of T-BLG. The dashed line is the average σ_{out} of all the data points. (b) Normalized graphene film conductivity versus average flake area for graphene films in the literature.

3.4.5 Top contacts

For some measurements, it is necessary to contact a GCM sample from the top. In that case, current does not flow spatially homogeneously, but propagates from the top contact into the sample and back out again. The network simulation method can be easily adapted to investigate this scenario: The border region used for current injection (Figure 3.4.3) is replaced by selected flakes from the uppermost layer, and the voltage probe surfaces are adjusted accordingly. For homogeneous materials, top contacts have been studied extensively, especially in the context of four-point probe measurements [139]. For a layered material built from anisotropically conductive components however, such a study has not been conducted.

Consider the model system depicted in Figure 3.4.12 (a) with length $l = 100 \mu\text{m}$, width $w = 50 \mu\text{m}$, and a thickness of 25 graphene layers. The two top contacts I_+ and I_- cover the full width of the structure and $8 \mu\text{m}$ of its length. Current enters the system through I_+ and leaves through I_- . Current propagation is investigated by plotting the total amount of current between $x = 20 \mu\text{m}$ and $x = 80 \mu\text{m}$ as a function of the layer⁴. The top layer corresponds to $z = 0$, the n -th layer from the top has the position $z = n$.

⁴These x -positions are selected to rule out any effects of the proximity to the current insertion or exit positions, while preserving a sufficiently long measuring distance for statistical averaging over many flakes.

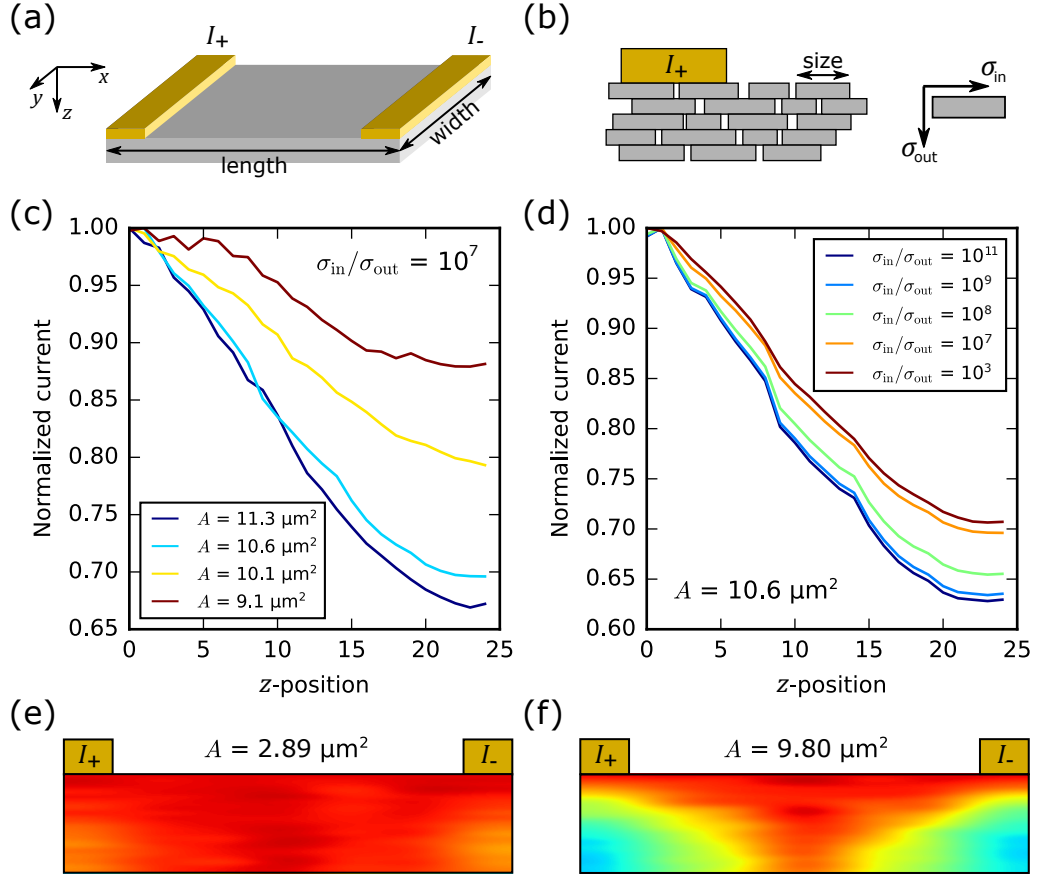


Figure 3.4.12: (a) Model system for the investigation of current propagation. (b) Decisive material parameters in the GCM: average flake area and conductivity anisotropy σ_{in}/σ_{out} (c) and (d) Total amount of current (normalized) as a function of z -position for (c) fixed σ_{in}/σ_{out} and variable flake areas, (d) fixed average flake areas and variable σ_{in}/σ_{out} . (e) and (f) Color-coded current density $j(x, z)$ for fixed $\sigma_{in}/\sigma_{out} = 10^9$ and different average flake areas $A = 2.89 \mu\text{m}^2$ and $A = 9.80 \mu\text{m}^2$. Red color corresponds to the highest current density (1.0), blue to the lowest (0).

Since GCMs are nanostructured materials, the internal material properties have to be considered. The major contributors are the average flake area and the conductivity anisotropy $\sigma_{\text{in}}/\sigma_{\text{out}}$ as shown in Figure 3.4.12 (b). The results are plotted in Figure 3.4.12 (c) and (d).

Generally, current flow decreases towards the bottom of the model system, which is expected when top contacts are employed. In Figure 3.4.12 (c), the average flake area A is varied for a fixed ratio $\sigma_{\text{in}}/\sigma_{\text{out}} = 10^7$. For the smallest flakes with $A = 9.10 \mu\text{m}^2$, the amount of current in the bottom layer is still as high as 88% of the current in the top layer. With increasing flake sizes, current flow is more and more concentrated on the uppermost layers. At an average flake area of $A = 11.3 \mu\text{m}^2$, the current in the bottom layer has dropped to 67% of the total current in the top layer. Within the framework of the network model, the explanation is straightforward: For larger flakes, fewer flake-to-flake transitions are required to connect the top contacts. At each transition, current can spread deeper into the sample such that the number of current-carrying flakes is increased. However, since the current leaves the structure through a top contact again, it needs to propagate back to the uppermost layer. Thus, the fewer the flake-to-flake transitions, the less likely it is that the current will spread to the bottom. This behavior is independent of $\sigma_{\text{in}}/\sigma_{\text{out}}$.

In Figure 3.4.12 (d), the conductivity ratio $\sigma_{\text{in}}/\sigma_{\text{out}}$ is varied for a fixed average flake area $A = 10.6 \mu\text{m}^2$. At $\sigma_{\text{in}}/\sigma_{\text{out}} = 10^{11}$, the amount of current in the bottom layer has decreased to 63% of the value in the top layer. At $\sigma_{\text{in}}/\sigma_{\text{out}} = 10^3$, it has only decreased to 71%. There is a clear trend: the smaller $\sigma_{\text{in}}/\sigma_{\text{out}}$, the more the current spreads into the bottom layers. The explanation is straightforward. Flake-to-flake transitions become more conductive compared to in-plane conduction when $\sigma_{\text{in}}/\sigma_{\text{out}}$ decreases. Thus, it is more efficient for current to propagate towards the bottom of the structure. Despite the fact that the conductivity ratio is varied over eight orders of magnitude, while the flake sizes are only altered by $\sim 20\%$, the influence of the flake sizes is more significant. The reason is the nanostructured nature of GCMs. Both in-plane and out-of-plane conductances contribute to current transport through a GCM as soon as more than one flake is involved. Even for current flow that is perfectly aligned with the plane of the flakes, flake-to-flake transitions are necessary. Thus, when $\sigma_{\text{in}}/\sigma_{\text{out}}$ is altered, both the current flow in (x, y) -direction $I_{(x,y)}$ as well as in z -direction I_z are affected. The impact on I_z is stronger however, which is why there is a net effect as seen in Figure 3.4.12 (d).

Summarizing, small flakes and a small conductivity anisotropy favor current propagation into the deeper layers of a GCM. For larger flakes and a larger conductivity anisotropy, current flows mainly in the layers close to the top

contacts. Figures 3.4.12 (e) and (f) visualize these two cases using the same model system as in (a). The color-coded current density j is shown as a function of the (x, z) -position. The values are integrated along the y -direction and normalized to the top layer $z = 0$. The color scale ranges from red ($j = 1.0$) to blue ($j = 0$). The conductivity anisotropy is set to $\sigma_{\text{in}}/\sigma_{\text{out}} = 10^9$, the average flake areas are $A = 2.89 \mu\text{m}^2$ in (e) and $A = 8.90 \mu\text{m}^2$ in (f). While the current spreads homogeneously into the model system in (e), it is limited to the upper layers in (f), except for the middle part of the structure, where substantial current flow reaches down to the bottom.

The distinction between the scenarios shown in (e) and (f) is common in the four-point probe technique. In Figure 3.4.12 (e), current flow is nearly independent of the z -position. This corresponds to a sample that is thin compared to the probe separation, i.e. it is considered to be 2D. Accordingly, when a sample is thick compared to the probe separation, it is considered 3D [139]. In a four-point measurement, the transition from 2D- to 3D-behavior is observed when moving from a small probe spacing to a large one in a single sample [140]. Such a measurement yields the different components $\sigma_x = \sigma_y$, σ_z of the conductivity tensor $\boldsymbol{\sigma}$. Note that these components differ from σ_{in} and σ_{out} of the individual flakes.

For the 2D/3D transition, consider the system shown in Figure 3.4.13 (a). It is similar to the previous model system, but additional voltage probes U_+ and U_- are applied. Furthermore, the structure is expanded so far in the x -direction that it can be considered infinitely long. This point is reached as soon as the four-point probe resistance $R = (U_+ - U_-)/I_+$ does not change by further extension. The width of the structure is $w = 40 \mu\text{m}$, the thickness t comprises 30 layers of graphene flakes with an average surface area of $A = 10.6 \mu\text{m}^2$. The four contact pads I_+ , I_- , U_+ , and U_- are arranged equidistantly with a spacing that is varied from $s = 14 \mu\text{m}$ to $s = 100 \mu\text{m}$. The length of the structure is adaptive to the spacing $l = 20 \mu\text{m} + 3s$. The packing density is $p = 0.8$. Note that the x - and y -coordinates are interchangeable since the in-plane electrical conductivity σ_{in} is homogeneous in graphene.

The limiting cases of homogeneous 2D and 3D samples with anisotropic conductivity can be treated analytically to compute the expected four-point probe resistances $R_{2\text{D}}$ and $R_{3\text{D}}$. A derivation of the expressions is found in the Appendix 6.4.

$$R_{2\text{D}} = \frac{s}{wt} \frac{1}{\sigma_x} \quad (3.4.14)$$

$$R_{3\text{D}} = \frac{2 \log 2}{\pi w} \frac{1}{\sqrt{\sigma_x \sigma_z}} \quad (3.4.15)$$

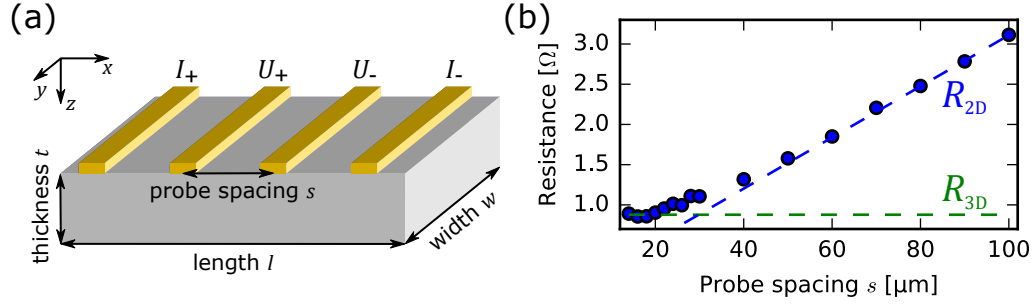


Figure 3.4.13: (a) Model system for the investigation of the 2D/3D transition in a thin sample. (b) Four-point probe resistance as a function of probe spacing. The circles are simulated data points, while the dashed lines indicated the theoretical 2D- (blue) and 3D-limits (green).

Figure 3.4.13 (b) shows the simulated four-point probe resistance R as a function of probe spacing s . For large values of s , R approaches R_{2D} as indicated by the dashed blue line. In this regime, equation (3.4.14) holds, i.e. $R \propto s$, and σ_x can be extracted. Regardless of the σ_{out} -value, σ_x is found to be equal to σ_{tot} as investigated in the previous sections. This is in line with expectations since σ_{tot} was always computed for side-contacted systems. In those cases, spatially homogeneous current flow independent of the z -position is expected. The accordance of the simulated data points with the theoretically derived analytical expression (3.4.14) shows that for large enough systems, a GCM does indeed behave like an anisotropic but homogeneous material, confirming again the self-averaging nature of the system. Additionally, the accordance implies that a four-point resistance measurement is suitable to determine σ_{tot} when the probes are sufficiently spaced.

For small s , R saturates to R_{3D} , which is independent of s . In Figure 3.4.13 (b), the value is indicated by a dashed green line. When $\sigma_x = \sigma_{tot}$ is already extracted from the 2D-limit, equation (3.4.15) can be used to compute σ_z , a quantity that characterizes current flow through a GCM in the direction perpendicular to the graphene layers. Thus, the full conductivity tensor σ is obtained. The fluctuation of the data points in the 3D-limit is slightly more pronounced than in the 2D-limit since fewer flakes connect the closely spaced contacts. However, the contact pads that span the full width of the structure cover several flakes and thus provide some statistical averaging.

For typical σ_{in} - and σ_{out} -values as found in section 3.4.4.3, σ_z is substantially smaller than σ_x . Assuming $\sigma_{in}/\sigma_{out} = 10^7$, the four-point simulation yields an even larger $\sigma_x/\sigma_z \approx 5 \cdot 10^7$. This initially surprising value can be understood by considering the geometry of the model system in Figure 3.4.13 (a), and

the general formula for electrical conductivity

$$\sigma_i = R_i \frac{l_i}{A_i} \quad (3.4.16)$$

with the resistance R , the length l and the conductor cross-section A . The index i refers to either the x - or the z -coordinate. In the case of σ_x , the conducting cross-section is given as the product of thickness and width of the model system. The relevant length is the system length.

$$A_x = t \cdot w \quad (3.4.17)$$

$$l_x = l \quad (3.4.18)$$

For σ_z on the other hand, the geometric quantities are given as:

$$A_z = l \cdot w \quad (3.4.19)$$

$$l_z = t \quad (3.4.20)$$

The values of R_x and R_z are assumed to be on the same order since they are both defined by a sequence of a similar number of alternating in-plane and out-of-plane connections. For this specific case, and with $l = 100 \mu\text{m}$ and $t = 30 \cdot 0.335 \text{ nm}$, the ratio σ_x/σ_z is obtained as

$$\frac{\sigma_x}{\sigma_z} \approx \frac{l_x}{l_z} \frac{A_z}{A_x} = \frac{l^2}{t^2} = 10^8, \quad (3.4.21)$$

For a quick first approximation, the results is very close to the simulated $\sigma_x/\sigma_z \approx 5 \cdot 10^7$ and shows why $\sigma_x/\sigma_z > \sigma_{\text{in}}/\sigma_{\text{out}}$.

In comparison to samples with isotropic conductivity, the transition from 2D to 3D behaviour only occurs at a relatively large probe spacing. For isotropically conductive samples, theory and experiment predict a threshold $s \approx 5t$, above which 2D-behavior is observed [141, 142]. In the case displayed in Figure 3.4.13 however, 2D-behavior only sets in for $s > 50 \mu\text{m} \approx 5000t$, which is due to the anisotropy of the conductivity tensor [143]. There are direct consequences of this observation for measurements in an experiment: Even with movable probe tips, it is not trivial to measure the 2D/3D-transition on graphene films since large probe spacings s on very thin samples are required. Moreover, when performing top contact measurements to extract σ_{tot} , s needs to be large enough to ensure 2D-behavior. Otherwise, the determined σ_{tot} -values and the σ_z -values derived from them will be incorrect. Fixed contacts however are less flexible and may have an impact on the overall material system properties, which is not ideal either. In general, top contacts are not ideal for highly anisotropic GCMs, since current will only

flow through the near-surface parts. Side contacts or large contact distances avoid this problem.

As demonstrated in this section, the network model is well-suited to model top contacts on GCMs. The findings will be used further in section 4.3.2.

3.4.6 Evaluating raw materials for GCMs

The network simulation method predicts the electrical conductivity of GCMs based on the microscopic properties of the corresponding raw material. This enables systematic optimization, which is particularly relevant in production scenarios in which material properties are linked and cannot be tuned independently. Two examples are shown in References [144] and [145], where ultrasonication is used to exfoliate graphite into graphene. Due to the employed method, the lateral flake size decreases with the number of layers. As both the layer number and the lateral flake size have a significant impact on overall electrical conductivity, the question arises, at which point a producer should rather focus on flake size instead of layer number or vice versa. The problem and the solution obtained with the network simulation method will be illustrated by two exemplary scenarios.

Scenario 1: Consider a manufacturer of graphene mono- and multilayers. Due to the manufacturer’s processing, the flake diameter and the number of layers are linked in a similar way to Reference [144]. The in-plane conductivities of the manufacturer’s flakes depend on the layer number as well and follow the mathematical relation as proposed in Reference [28]. For various layer numbers, the corresponding flake diameters and in-plane conductivities are summarized in Table 3.2. The data is used as input for the network simulation, and the GCM conductivity is predicted for each set in Table 3.2. The packing density is assumed to be $p = 0.8$. For a wide range of out-of-plane conductivities, the resulting total conductivities of the GCMs are shown in Figure 3.4.14 (a).

| Layers | Flake diameter [μm] | Scenario 1: σ_{in} [MSm^{-1}] | Scenario 2: σ_{in} [MSm^{-1}] |
|--------|-------------------------------------|---|---|
| 1 | 0.70 | 100 | 100 |
| 2 | 0.90 | 50.9 | 25.0 |
| 3 | 1.02 | 34.5 | 11.1 |
| 4 | 1.50 | 26.3 | 4.34 |
| 7 | 3.00 | 15.8 | 0.38 |
| 10 | 6.80 | 11.5 | 0.25 |

Table 3.2: Relation of layer number, flake diameter, and in-plane conductivity for two scenarios.

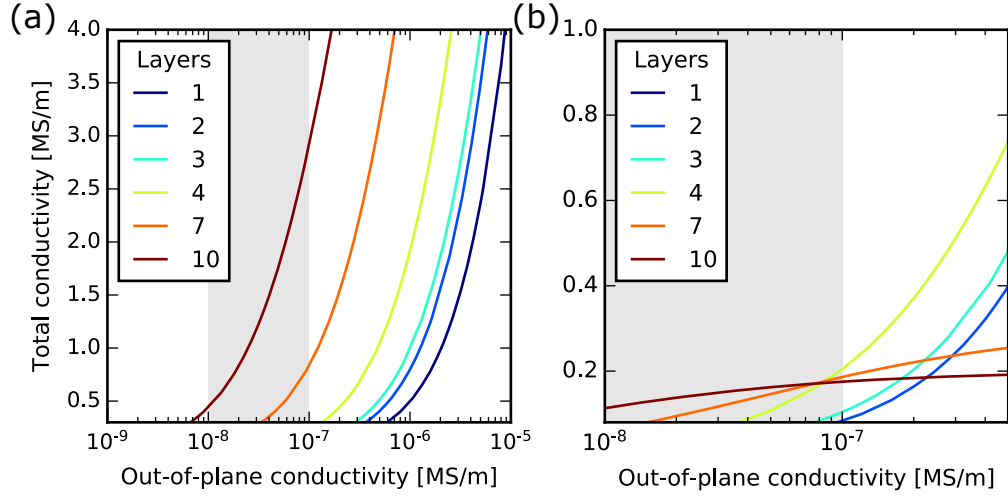


Figure 3.4.14: Conductivities of GCMs produced from base materials with different layer numbers. The expected out-of-plane conductivity range is highlighted in gray. (a) Scenario 1. (b) Scenario 2.

Considering published GCM data (see section 3.4.4.3) as well as theoretical and experimental works on T-BLG [133, 30], the out-of-plane conductivity likely ranges between 10^{-7} MSm $^{-1}$ and 10^{-8} MSm $^{-1}$ (shaded area in Figure 3.4.14). In this region, the multilayer graphene flakes with ten layers yield the most conductive GCM by far. All the other layer numbers are linked to small diameters $\leq 3 \mu\text{m}$, which is detrimental to the total conductivity. It is also apparent that the potential of the manufacturer's material cannot be fully exploited in a pure GCM. The out-of-plane conductivity required to reach the saturation regime would be unrealistically high. Hence, despite high individual flake conductivities even for few-layer flakes, the manufacturer's material is not particularly suitable for undoped high-performance GCMs.

Scenario 2: A different manufacturer provides graphene flakes with the same layer number-flake size relation as in Scenario 1. However, compared to Scenario 1, the in-plane conductivities are worse for few-layer graphene. The in-plane conductivity data is taken from Reference [29] and can also be found in Table 3.2. The resulting $\sigma_{\text{tot}}(\sigma_{\text{out}})$ -curves are shown in Figure 3.4.14 (b). In this case, the evaluation is not as clear as before. In the out-of-plane conductivity range between 10^{-7} MSm $^{-1}$ and 10^{-8} MSm $^{-1}$, the optimum layer number varies. For the biggest part, the flake size is dominating and compensates a low in-plane conductivity. Thus, multilayer flakes with ten layers are best for GCM conductivity. When the out-of-plane conductivity

approaches 10^{-7} MSm $^{-1}$ however, graphene flakes with four layers yield the most conductive GCM.

It becomes clear that a sound knowledge about the raw material is crucial to answer the question of the optimum combination of flake sizes and layer numbers. When a material is thoroughly characterized, the network simulation can be used to optimize it for GCM conductivity. If it is desired, mixtures of flake sizes and diameters can be studied as well. Apart from optimization studies, the network simulation method also enables the fast evaluation of a raw material. It can be used to predict the potential of a material, and to identify its weak points. Regardless of the field of application, the material properties which serve as input parameters for the simulation need to be determined as precisely as possible to obtain meaningful simulation results.

3.4.7 Implications for the production of GCMs

The results obtained from the network simulations have strong implications for the manufacturing of GCMs. In the following, the main findings are translated into production guidelines.

In statistical analyses, it is found that a perfectly homogeneous in-plane conductivity across the whole GCM is best for the overall electrical conductivity. The broader the in-plane conductivity distribution, the lower the total conductivity. In a real-world scenario, a perfectly homogeneous in-plane conductivity is virtually impossible since a minimum degree of fluctuation will naturally occur. Still, a guideline can be derived: When dopants are employed, it is most beneficial to distribute them as evenly as possible in the GCM and to avoid clustering. For example, surface coating of the macroscopic material is expected to be less efficient than a treatment of the complete volume, such as vapor-phase doping. When optimizing a GCM, the focus should be on improving the quality of the least conductive flakes instead of pushing the limits of the most conductive ones. Thus, the conductivity distribution becomes narrower.

The opposite holds true for the out-of-plane conductivity: Highly conductive flake-to-flake transitions dominate poorly conductive ones. Thus, a heterogeneous out-of-plane conductivity distribution is more effective than a homogeneous one with comparable average parameters. It leads to an earlier start of the transition regime without reducing the total conductivity in saturation. Just like for the in-plane conductivity, the out-of-plane conductivity in a GCM is subject to statistical fluctuations. The conclusion that this is not detrimental to the overall performance is a promising result for applications. The benefit of large graphene flake sizes for GCM conductivity is one of the clearest results of this work. The underlying physical mechanisms are evident:

Not only do larger flake sizes reduce the amount of flake-to-flake transitions, but they also increase the overlap areas and are thus able to compensate low out-of-plane conductivities. Furthermore, the flake size is a property, which is easier to manipulate during production than all the other input parameters. To change the flake size, a different raw material has to be chosen or the size selection step has to be slightly altered, but no additional materials or new processes are required. One example where flake sizes can be exploited are acceptor-like dopants. Some of those dopants (e.g. AsF_5 , SbF_5) lead to exceptionally high in-plane conductivities but most of them are detrimental to the out-of-plane conductivity [46]. Larger flake sizes can mitigate or even fully compensate these effects so that the full potential of the dopants can be reached. The quantitative analysis from the previous sections allows for the precise determination of the required flake size for optimum conductivity when a certain out-of-plane conductivity is given. Thus, the appropriate raw material to balance price, processibility and optimum conductivity can be selected. The simulations also show that the exact distribution of flake sizes is irrelevant as long as the average flake size is appropriate. This makes manufacturing a lot easier since the composition of a tailor-made flake size distribution is most likely cost- and time-intensive.

The percolation-type study on non-conductive flakes shows that the obtainable maximum conductivity of a GCM is severely reduced when non-conductive elements are incorporated. If additives other than dopants are indispensable, their share has to remain below 10%. Otherwise, the GCM is not useful as a conductor anymore.

According to FEA and the network model, arranging graphene flakes along the current direction has an effect similar to employing larger flakes. In GCM production, this can be helpful when access to large enough flakes is limited. In that case, a proper flake arrangement can still compensate an insufficient out-of-plane conductivity. As an example, microfluidic methods similar to Reference [98] could be employed during wet spinning to create fibers with an in-plane flake arrangement.

Regardless of the flake orientation, a dense and homogeneous packing that is free of holes should be made a high priority. The simulations show that optimum conductivity is only achievable for a homogeneous spatial distribution of the graphene flakes. If inhomogeneities do occur, an even distribution across the material is always preferable over large clusters.

In general, the interplay of the various material parameters, which affect the conductivity of a GCM, makes a quantitative evaluation difficult. As different influencing factors compete, they overlap or even dominate each other. The network simulation method helps to interpret experimental results and to understand the underlying physical reasons. It is also a useful tool for the

optimization of a material when a trade-off has to be accepted. As shown in section 3.4.6, where a higher in-plane conductivity is connected to a smaller flake size, the network simulation method can be used to quickly analyze a large parameter space and find the optimum conditions.

In terms of competitiveness with metal conductors, the simulation has not revealed any showstoppers for GCMs. In fact, recent publications show that most material parameters are already in a competitive range. References [83], [84], and [72] are three examples where packing densities $p > 0.9$ have been achieved. Raman-spectra reveal a low amount of defects at the same time as well. Reference [98] contains a thorough analysis and demonstration on how to achieve dense and ordered packing of graphene fibers. References [120] and [73] show that GO flakes with lateral dimensions of more than $80\text{ }\mu\text{m}$ can be successfully produced and processed. With these dimensions, even purely turbostratic flake-to-flake transitions can be considered sufficiently conductive. The requirements deduced from previous publications as shown in section 3.4.6 are also fulfilled. The situation is different for graphene flakes. Commercial graphene dispersions currently seem to be limited to flake diameters $< 10\text{ }\mu\text{m}$. This can be sufficient, but not necessarily. To be on the safe side, manufacturers can either concentrate on producing larger flakes, or exploit other possibilities to engineer highly conductive GCMs such as appropriate dopants or anisotropically ordered flakes.

Regarding the in-plane conductivity: In an idealized pure GCM, graphene flakes could be electronically decoupled, e.g. due to misalignment, so that the in-plane conductivity in the bulk does not differ from the in-plane conductivity of isolated monolayers. So far, however, there is no publication that reports on methods to achieve this situation on a large scale. A more promising approach to increase electrical conductivity is the usage of dopants. References [65] and [100] have both demonstrated significant conductivity improvements upon doping. Most importantly, in studies on GICs, electrical conductivities even higher than in copper or silver have been achieved [63, 146, 46]. This underlines the great potential of doped GCMs, which are structurally similar to GICs.

If the above guidelines can all be followed at the same time, there seems to be no fundamental material-related limit that prevents super-metallic electrical conductivity in a GCM. In terms of processing technology however, the main challenge is to combine all the desired material parameters without creating new weaknesses.

3.4.8 Summary

The resistor network model enables fast and comprehensive analyses of the electrical conductivity of GCMs. Out of all the investigated simulation methods, it is the most suitable one. In contrast to the analytical model and the finite element approach, it is more efficient and more flexible.

For all three simulation methods, the $\sigma_{\text{tot}}(\sigma_{\text{out}})$ -curves are generally similar in shape and position, irrespective of the complexity and precision of the method. The maximum conductivity values are identical, as is the effect of flake size scaling. Analogous to FEA, the network model reveals that anisotropically oriented graphene flakes have a positive effect on the total conductivity while inhomogeneities are detrimental. Simulations with the network model further suggest that statistical distributions of physical quantities can have a severe impact on the total conductivity. The broader the distribution of in-plane conductivities, the smaller the resulting total conductivity. A wide range of out-of-plane conductivities on the other hand can be beneficial for the total conductivity. Apart from parameter studies, the simulations are compared to literature results. A high degree of agreement is found, but the amount of data that is suitable for a comparison is very small. Last, the potential for systematic material optimization is demonstrated, and guidelines for manufacturers are derived.

Due to the brick-and-mortar structure, the network model is versatile and can be extended efficiently. A simple approach is to alter the 2D building blocks to other materials than graphene. This is demonstrated in sections 3.4.4.2 and 3.4.4.3 respectively, where non-conductive as well as doped flakes are introduced. So despite the original intent, the network model can be understood as a simulation method for 2D-based composites with anisotropic conductivity rather than being limited to GCMs. This also includes composites where 2D flakes are embedded in a rigid matrix [147]. In these materials, the 2D content is often far below the high-conductivity threshold $p = 0.7$ defined in this work. However, the rigid matrix keeps the flakes in place and prevents sagging, which fits the network model. For those types of composites, the focus is usually more on percolation studies than on the high conductivity regime [148]. This is beyond the scope of this work, but it represents an interesting use case.

A more comprehensive extension to the network model would be the introduction of multiphysical effects such as strain- or temperature dependence. In the case of strain for example, the geometric structure would be affected as well as a few other input parameters such as the in-plane or out-of-plane conductivities. With a suitable mathematical description, a multiphysical extension to the network model would be easily feasible.

The overall agreement between the three simulation approaches and the accordance with literature data make a strong case for the network model. The studies are conclusive and the results offer valuable insights. The simulations have deepened the understanding of GCMs. During the experimental part of this work, the network model will be verified once again by comparing simulated and measured data. It will also be used as a tool to interpret the experimental results and to distinguish between the influences of different material parameters.

4 Preparation and analysis of graphene-based thin films

4.1 Introduction

The experimental part of this thesis serves two main purposes. First, the quantitative mathematical relations established in chapter 3 are validated with measurements on self-produced samples. The data presented in the literature is neither sufficient for this purpose nor properly accessible. Second, the experimental work is essential for a sound assessment of the potential of GCMs. Suitable synthesis and characterization methods are identified and evaluated with regard to large-scale production scenarios.

Graphene-based thin films are found to be a convenient material system for the above-mentioned purposes. In contrast to graphene fibers, high-quality graphene films can be synthesized without complex technical equipment. They can be produced quickly, at low cost, and with a large variety of base materials while using a single experimental setup. This allows for the systematic variation of microscopic parameters to validate the simulations. It also leads to the generation of a large data set of process information, which is further analyzed to deepen the understanding of GCMs and their potential. Doping is beyond the scope of the experimental part of this thesis. Only undoped, pure carbon films are investigated.

Chapter 4 is divided into three sections. The first part provides a detailed outline of the graphene film synthesis. The relevant methods are explained and their efficacy is evaluated. In the second part, the films are characterized structurally and electrically to verify several assumptions from chapter 3. In the third part, graphene films with systematically varied microscopic parameters are prepared, and the results are compared to the simulations. To conclude, the potential of GCMs in large-scale applications is reassessed based on the new findings.

4.2 Preparation of graphene films

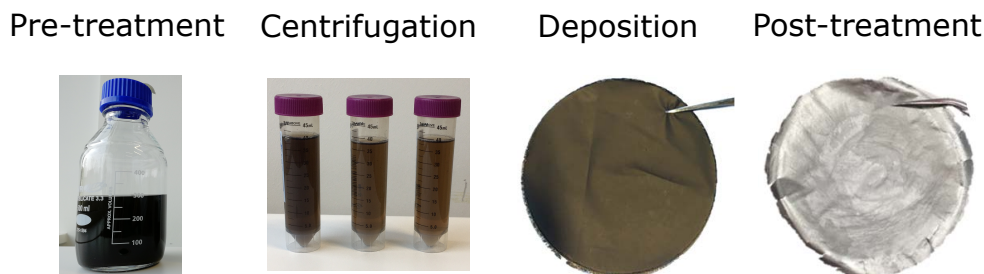


Figure 4.2.1: Process flow for graphene film synthesis. From left to right: Ultrasonicated GO dispersion; centrifuged dispersion in tubes; deposited GO film; reduced GO film.

As a starting point for the preparation of graphene films, graphene or GO dispersions are purchased from various suppliers. They consist of exfoliated flakes, which are suspended in an aqueous solution where they remain colloidally stable. Purchasing the dispersions instead of synthesizing them in the lab saves time while preserving flexibility. Different raw materials from different suppliers can be tested without altering the preparation methods. Starting from the purchased dispersion, Figure 4.2.1 gives an overview of the process flow for graphene film synthesis as performed in this work. The first process step is a pre-treatment such as dilution or sonication. Then, centrifugation is performed to obtain the desired flake sizes. The centrifuged material is used for film deposition, followed by a post-treatment step such as pressing or thermal annealing. If GO is used as the starting material, a reduction step is performed as well.

4.2.1 Pre-treatment

For a successful film synthesis, some dispersions need to be pre-treated. Depending on the deposition method, a certain graphene or GO concentration is required. Here, concentrations are always expressed in mgml^{-1} , which signifies that a certain weight of graphene or GO is suspended in a given volume of the final product. For blade coating, a high concentration $> 10 \text{ mgml}^{-1}$ is required, while a concentration of 1 mgml^{-1} is appropriate for vacuum filtration. Centrifugation for size selection requires low concentrations $< 2 \text{ mgml}^{-1}$ as well. Therefore, dilution by adding more of the dispersion medium (e.g. water, ethanol, isopropyl alcohol (IPA), etc.) is frequently performed. Increasing the concentration is more difficult, but for GO in water,

it could be achieved by gently heating the dispersion without making it boil to prevent damage to the flakes or heavy agglomeration. Since this process is difficult to control and may alter the dispersion stability, it is completely avoided.

Some suppliers suggest mild sonication before using the dispersion, in order to separate or exfoliate agglomerated flakes. However, since sonication can decrease the lateral size of the flakes [120], it needs to be employed carefully.

4.2.2 Centrifugation

As outlined in section 3.4.4, the average flake size plays a crucial role in GCM conductivity. Hence, a centrifugation protocol is used to separate differently sized flakes. The approach is well established in the literature [144, 149, 150] and particularly suitable for macroscopic applications since large volumes can be processed efficiently.

In a centrifuge, a tube filled with dispersion is rotated such that a centrifugal force is exerted on the particles suspended in the dispersion medium. According to Stoke’s law, the larger the particles, the faster they move to the outside, i.e. the bottom of the centrifugation tube [151]. The emerging precipitate is called sediment, while the medium and the particles remaining above are called supernatant. The sediment mainly contains particles that are larger than a certain cutoff size, while the supernatant contains the smaller particles. The size separation depends on numerous factors such as the density and viscosity of the dispersion medium, the concentration of the dispersion, the sizes, and the density of the suspended particles, as well as the centrifugal force acting on them. Traditionally, the centrifugal acceleration is measured in multiples of the gravitational acceleration g and listed as “relative centrifugal force” RCF , a dimensionless quantity. It is defined as

$$RCF = \frac{4\pi^2}{g} r f_r^2 \quad (4.2.1)$$

with the distance from the tube to the rotation axis r and the rotational speed f_r . For centrifuges, the rotational speed is often measured in revolutions per minute (rpm). When f_r is increased, the centrifugal force increases as well and thus, the size cutoff for particles in the sediment decreases.

To sort a dispersion by flake size, several centrifugation steps have to be combined. The technique is sometimes referred to as liquid cascade centrifugation [152, 153] and illustrated in Figure 4.2.2. In multiple centrifugation steps with sequentially decreasing rotational speed, different flake size regimes are collected from the supernatant, while the sediment is processed further. All

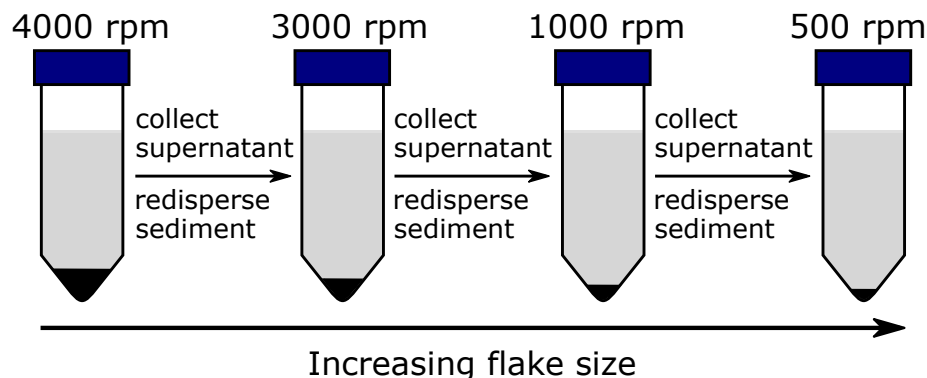


Figure 4.2.2: Exemplary centrifugation cascade used for flake size separation.

dispersions of graphene or GO contain a certain amount of unexfoliated multilayer flakes. These can be removed with an initial centrifugation step at a low rotational speed or remain in the sediment during the last steps in the cascade.

Since different dispersions from several suppliers are employed in this work, there is no universal relation between the rotational speed and the average flake size in the sediment. Thus, a method to measure the flakes' lateral sizes or surface areas is required. In the literature, most research groups deposit flakes on a flat surface and use an electron microscope for the size measurement [116, 117, 80, 72]. While it can be challenging to obtain a large data set in this way, the individual measurements are very precise due to the clear visibility. Other methods to measure particle sizes such as light scattering always struggle with the extreme geometrical anisotropy and the non-uniform layer numbers of 2D materials in dispersions [154, 145, 155].

The measurement technique used in this work is illustrated in Figure 4.2.3. First, a small volume of a given dispersion is diluted to 0.1 mgml^{-1} . With a pipette, a single droplet of the diluted dispersion is dripped onto a clean silicon piece. Subsequently, a filter paper is placed on top of the silicon piece and the sample is left to dry. Thus, water is sucked into the filter paper, while the flakes settle on the silicon surface. Drying without a filter paper is not recommended as it often results in the so-called “coffee stain effect”, where the majority of the dispersed material is carried towards the edges of the droplet during evaporation, leaving a ring-like stain [156]. With a filter paper, the dispersed flakes settle evenly on the silicon surface. After complete drying, the sample is imaged with a scanning electron microscope. As shown in Figure 4.2.3, large parts of the sample are covered such that many individual flakes are visible. The areas of the flakes are measured with a commercial software by defining a polygonal outline. For a sufficient amount of data, a

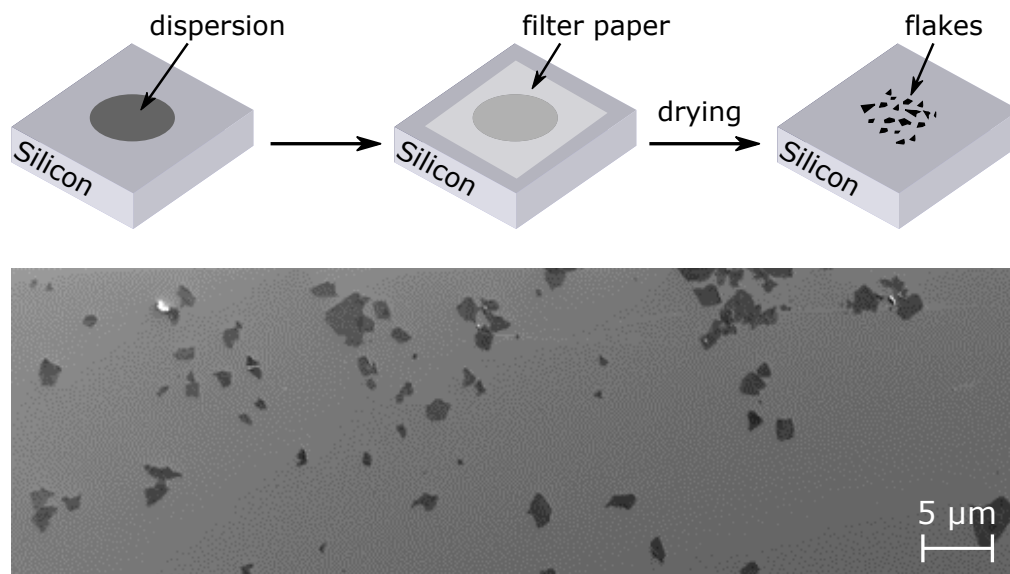


Figure 4.2.3: Top: Procedure to deposit graphene flakes for visualization as described in the main text. Bottom: Scanning electron micrograph of graphene flakes on a silicon substrate.

minimum of 100-150 flakes per sample should be measured. The lower bound holds for narrow distributions, while more flakes are required to characterize wide distributions.

The edge detection and subsequent area measurement are tasks which can be automated if necessary (see Supporting Information of Reference [116] for an example). In this case, the contrast has to be well adjusted such that monolayers and multilayers can be clearly distinguished, and overlapping flakes are counted individually and not as a single large flake. In this work, no automated process for edge detection is used as the naked eye seems to be less prone to error. Given the quantity of flakes evaluated here, it is not worth the effort of automation yet.

Since the visualization requires only a small amount of dispersion, the average flake size could theoretically be measured for every single film. However, it is more practicable to evaluate full centrifugation cascades within a given dispersion batch such that a relation between the average flake size and the centrifugation step is obtained. For two exemplary liquid cascade batches, one with graphene and one with GO, the relation between the rotational speed f_r and the resulting average flake area is depicted in Figure 4.2.4. Both batches are based on the centrifugation protocol as shown in Figure 4.2.2. The average flake area of the original dispersion is also indicated as a dashed line. In section 4.4, centrifugation is employed to study the effect of a sys-

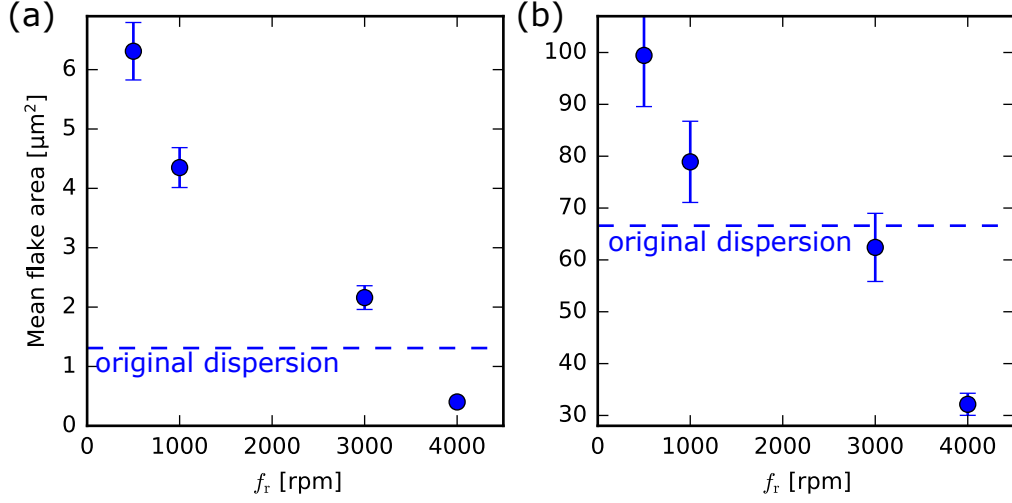


Figure 4.2.4: Flake sizes obtained from liquid cascade centrifugation of (a) a graphene dispersion and (b) a GO dispersion. The dashed lines indicate the mean flake area of the original dispersions, the errors stem from the statistical distribution of the measured flake sizes.

tematically varied flake size on the electrical conductivity of graphene films. The results are then compared to the prediction of the simulation and used for its validation.

Note that the selected sizes vary heavily between graphene and GO, despite the fact that the same centrifuge with identical values of RCF and the same cascade are employed. This confirms the above statement that there is no universal relation between rotational speed and average flake size in the sediment. For each dispersion a separate evaluation is required. If dispersions are stored for longer periods of time, a re-evaluation becomes necessary. Especially in graphene dispersions, particles tend to agglomerate after a few weeks, thus changing shapes and masses. GO dispersions are more stable, but still vary from supplier to supplier and have to be characterized individually.

4.2.3 Deposition

In this work, three common deposition methods to prepare graphene and GO films are tested: Casting, blade coating, and vacuum filtration. All of these methods are fast and cheap, and can be scaled up to process large amounts of graphene-based materials. They have all been used to create highly conductive graphene films with conductivities of up to 1 MSm^{-1} in undoped graphene films [72, 65, 157].

Casting

Casting is by far the simplest method: A given dispersion is cast into a suitable container or onto a substrate, and left to dry. The drying process can be accelerated by mild heating. If the dispersion medium evaporates too quickly, bubbles form and the film becomes structurally inhomogeneous. The higher the concentration of the dispersion in the beginning, the faster the drying process. While the dispersion medium evaporates, the flakes arrange into a flat structure, likely due to the surface tension of the dispersion medium [158]. However, for the films in this work, the ordering is not sufficient to produce mechanically stable and highly conductive films. All the films produced by casting and drying are rather brittle and less conductive compared to the other preparation methods. Additionally, while the films are flat, the thickness is not homogeneous across the samples. For these reasons, different approaches are chosen.

Blade coating

Blade coating is the process of scraping a highly concentrated dispersion, also referred to as “paste” or “slurry”, onto a substrate. For this, the viscosity of the dispersion needs to be large enough that a stable film with a well-defined thickness is formed. An illustration is given in Figure 4.2.5. In this work, a micrometer adjustable film applicator is used to scrape GO slurries with reproducible thickness. Copper or polytetrafluoroethylene (PTFE) are used as substrates. After the coating process, the film has to dry. In contrast to simple casting however, the flakes are pre-ordered before drying due to the shearing forces exerted by the coating blade.

All the blade-coated films produced in this work are mechanically and electrically superior to the films that are cast. The thickness of the blade-coated films is homogeneous and can be controlled. There are two challenges with blade coating. First, highly concentrated dispersions are so viscous that effi-

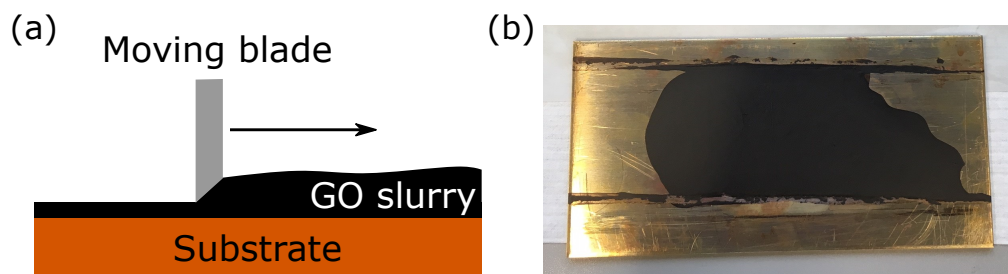


Figure 4.2.5: (a) Schematics of the blade coating process. (b) Graphene oxide film on a copper substrate.

cient centrifugation is not feasible. To select flake sizes from a given slurry, it would have to be diluted, centrifuged, and finally, the concentration would have to be increased again, all without degrading the material. The second challenge during blade coating is tuning the dispersion properties such that it is viscous enough while preventing the flakes from agglomerating. However, the chemical optimization of dispersions for coating is beyond the scope of this work.

Vacuum filtration

Vacuum filtration is employed for the majority of the purchased dispersions, since their viscosity is generally too low for blade coating. In addition, centrifugation and vacuum filtration require similar dispersion concentrations and can therefore be combined efficiently. In vacuum filtration, dispersions are filtered through a filter membrane with the support of a vacuum pump. The membrane is permeable to the dispersion medium, but impermeable to the flakes. During filtration, the flakes stack up on top of the membrane and a filter cake forms. The filter cake dries to become a film that can be peeled from the membrane and is freestanding if it is thick enough. Vacuum filtration is illustrated in Figure 4.2.6.

The ordering process of the graphene flakes during filtration has been analyzed in Reference [159]. It is suggested that at first, adhesion between the flakes produces a loosely aggregated structure where the basal planes of the flakes are aligned with each other. When the dispersion medium is subsequently removed, its surface tension compresses the structure into the

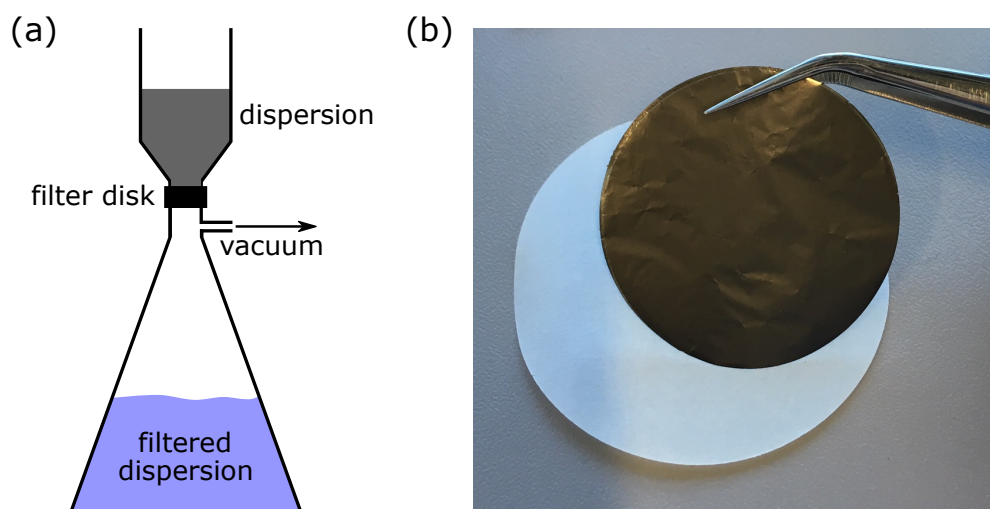


Figure 4.2.6: (a) Schematic depiction of vacuum filtration. (b) Freestanding vacuum filtrated GO film with membrane filter below.

final thin film. The high degree of order in the vacuum filtrated films results in mechanical integrity and a homogeneous thickness.

Vacuum filtration is particularly suitable for dispersions with low concentration, or for the preparation of ultrathin films $< 3\text{ }\mu\text{m}$. The drying process is extremely fast as the biggest portion of the dispersion medium is already removed during the filtration. The main challenge lies in preparing dispersions in such a way that the filter membranes do not get clogged and the dispersion medium can flow through them. To achieve this, it is often sufficient to remove the smallest particles by centrifugation or to use a membrane filter with a specific pore size and high compatibility to the given dispersion.

4.2.3.1 As-deposited thin films

In total, dispersions from six different suppliers (Appendix 6.5) are used to synthesize graphene or GO films. All but one can be processed via vacuum filtration and two are suitable for blade-coating. For the dispersion compatible with both methods, there is no difference in conductivity between blade-coated or vacuum filtrated films. After deposition and drying, basic physical measurements are performed to characterize the films. The thickness is determined with a Mitutoyo IP65 digital micrometer gauge with a precision of $1\text{ }\mu\text{m}$. On each film, the thickness is measured at 15 different positions and if the results are compatible, the average thickness is computed. The weight is measured with a Sartorius LA310S lab scale with a precision of 0.1 mg . The as-deposited films are mechanically flexible. They can be bent and folded without damage.

4.2.4 Post-Treatment

The synthesized thin films are subjected to three different forms of post-treatment: Chemical reduction in hydriodic acid (HI), thermal annealing, and mechanical pressing. For GO films, a reduction step is indispensable, while graphene films only profit from it when they are not fully reduced.

Chemical reduction

When GO films were first synthesized, the reduction was mainly performed with hydrazine [160, 67, 161], but in recent years, HI has shown to be more effective [162] so that many research groups have adopted the technique [117, 65, 163, 164]. In this work, GO films are immersed in HI for 24 hours and then thoroughly washed with ethanol and water. After the chemical reduction, the films change in color and exhibit a metallic luster. A before and after picture is shown in Figure 4.2.7 (a).

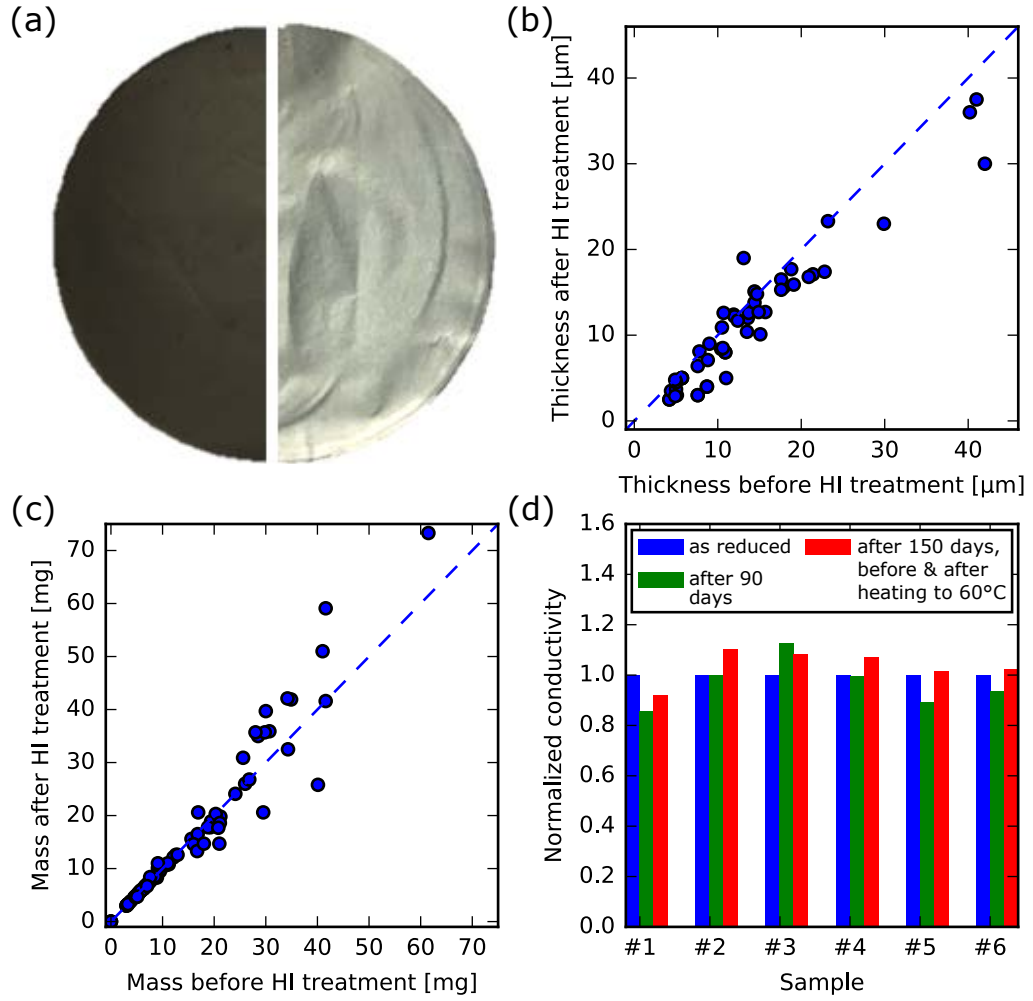


Figure 4.2.7: (a) GO film before (left) and after (right) HI-treatment. (b) Film thickness and (c) mass before and after HI-treatment. The dashed lines correspond to unchanged quantities. (d) Long-term conductivity measurements. The conductivities before and after heating to 60°C in air are identical.

Most of the films become thinner upon HI-treatment, which is consistent with Reference [162], where it is suggested that the shrinkage occurs due to the removal of oxygen-containing groups on the graphene sheets. The mass of most films remains approximately constant. For the GO films, this is an indication that some form of doping takes place. When all the oxygen is removed and the weight of the films does not change, other species have to be incorporated. For an estimation of an upper limit of the iodine content after immersion in HI, consider a typical GO film with 60% carbon atoms and 40% oxygen atoms¹. Assuming that all the oxygen weight (16 u per atom) is replaced by iodine weight (127 u per atom), the film would exhibit an atomic percentage of iodine atoms of 7.7% after HI-treatment. A possible explanation could be that the removed oxygen functional group leave defect sites behind where iodine attaches in a stable way. Alternatively, iodine might be intercalated between graphene sheets.

The effects of HI-treatment are long-term stable. Over a period of 150 days, the conductivities of HI-treated samples stored in a plastic box under ambient conditions fluctuated by $\lesssim 10\%$ around their mean values, but without an overall trend. The conductivities remained the same when the films were heated to 60°C in air. The results of the thickness, mass and long-term conductivity measurements are shown in Figure 4.2.7 (b) - (d).

Thermal annealing

After chemical reduction, a thermal annealing step is highly recommended. Chemically removed oxygen groups leave dangling bonds and other defects behind, which impair the electrical conductivity of the films. Depending on the annealing temperature, a thermal treatment can fully heal these defects and restore the graphene lattice [165, 166, 167]. Additionally, thermal treatment removes contaminations from the films such as residual additives from the dispersion or leftover oxygen-containing functional groups.

It has been found that at temperatures above 2000°C, the carbon atoms rearrange into an energetically favorable position such that the pristine sp²-structure is restored [168, 166, 73]. This implies that not only GO but also pure graphene films can benefit from a thermal treatment. In all the publications on thermally treated GCMs, there is an unambiguous connection between the annealing temperature and the electrical conductivity: The highest temperatures consistently lead to the highest conductivities [83, 166, 167, 94, 92, 73, 13]. Furthermore, the best absolute conductivities are achieved with films treated at temperatures between 2500 and 3000°C. Therefore, a high-temperature annealing is indispensable for optimum con-

¹See Appendix 6.5 for the oxygen content of the dispersions used in this work

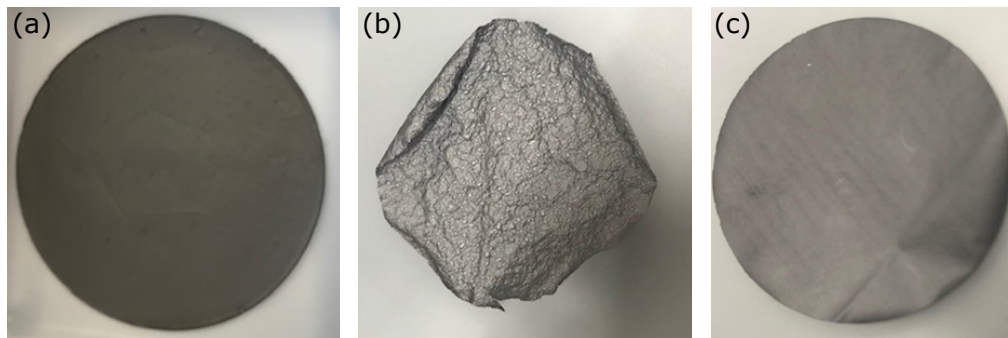


Figure 4.2.8: Graphene film (a) before thermal treatment, (b) after thermal treatment, and (c) after mechanical pressing.

ductivities. In this work, a Carbolite LHTG 100-200/30-2G furnace is used for thermal treatment. The interior of the heating chamber is fully constructed from graphite, which makes annealing temperatures of up to 3000°C possible. Typical annealing times are 15-30 minutes, where longer annealing times lead to higher conductivities. Annealing times > 30 minutes do not lead to further improvement of the films prepared in this work.

Previous literature data shows that during high-temperature thermal annealing, nearly all the oxygen is removed from carbon films [168, 166]. Correspondingly, a considerable loss of thin film mass is observed in this work as well: Graphene-based films lose up to 30% of their mass, GO-based films up to 70%, which is more than the expected oxygen content (see Appendix 6.5). From the data gathered here however, it is not possible to identify which portion of the mass loss stems from oxygen, carbon, or foreign chemical species such as the residual iodine from HI-treatment. It should be noted though that previously annealed films do not lose any more mass if they are subjected to an additional high-temperature heat treatment. This suggests that during thermal annealing, the films obtain a stable internal structure without any loosely bound particles.

As the heating process leads to the outgassing of chemical species, thermally treated films often exhibit bubbles and a substantially increased thickness. However, if these films are subsequently pressed, their thickness can usually be reduced to a lower value than before the thermal treatment. Most notably, the films keep their mechanical integrity and stay flexible; an observation that is also found in the literature [73]. Figure 4.2.8 shows before and after pictures of thermally treated and subsequently pressed films. After being crumpled and expanded during the heating, the films can be fully flattened again.

Mechanical pressing

The last step of the post-treatment is always mechanical pressing to densify the films. There is no benefit in carrying out this step at an earlier stage, because both wet-chemical and thermal treatment can increase the layer separation and thus decrease the film density. An MTI HR01 rolling press (schematics in Figure 4.2.9 (a)) is found to be the most effective tool for pressing, since the thin, line-like contact between the rolls leads to very high pressures. A 120 μm -thick silicone-free transfer foil with is used as a substrate. Figure 4.2.9 (b) shows the thicknesses of graphene films before and after pressing, (c) shows the corresponding densities, and (d) compares the change in density to the change in conductivity. A major thickness reduction is only possible for films thicker than 10 μm because of the residual gap between the rolls. Due to the nature of the device, thicker films can be exposed to higher pressures than thinner films. This is why the highest densifications are achieved for initially thick films $> 30 \mu\text{m}$. According to this interpretation, the thinner films could potentially be densified even further. Across all thicknesses, an average thickness reduction of 22% is achieved. Note that the relative densification of the films is not dependent on the initial density as shown in Figure 4.2.9 (c). Across a broad range of initial densities between 0.6 and 1.3 gcm^{-3} , a density improvement of 100% or more can be achieved².

The conductivity gain after mechanical densification as shown in (d) seems to be mainly a geometrical effect. On average, an increase in film density by a factor F leads to an increase in conductivity by a factor $1.08 F$. This suggests that mechanical pressing does not reduce the distance between the graphene layers, but rather compresses cavities created during the deposition. A significant reduction in layer separation on the other hand would lead to an improved out-of-plane conductance and an increase in density at the same time, surpassing the almost 1:1 correspondence between density and conductivity increase.

²In (c) only those films are shown where the density was evaluated before and after pressing and where compression was achieved exclusively by mechanical pressing.

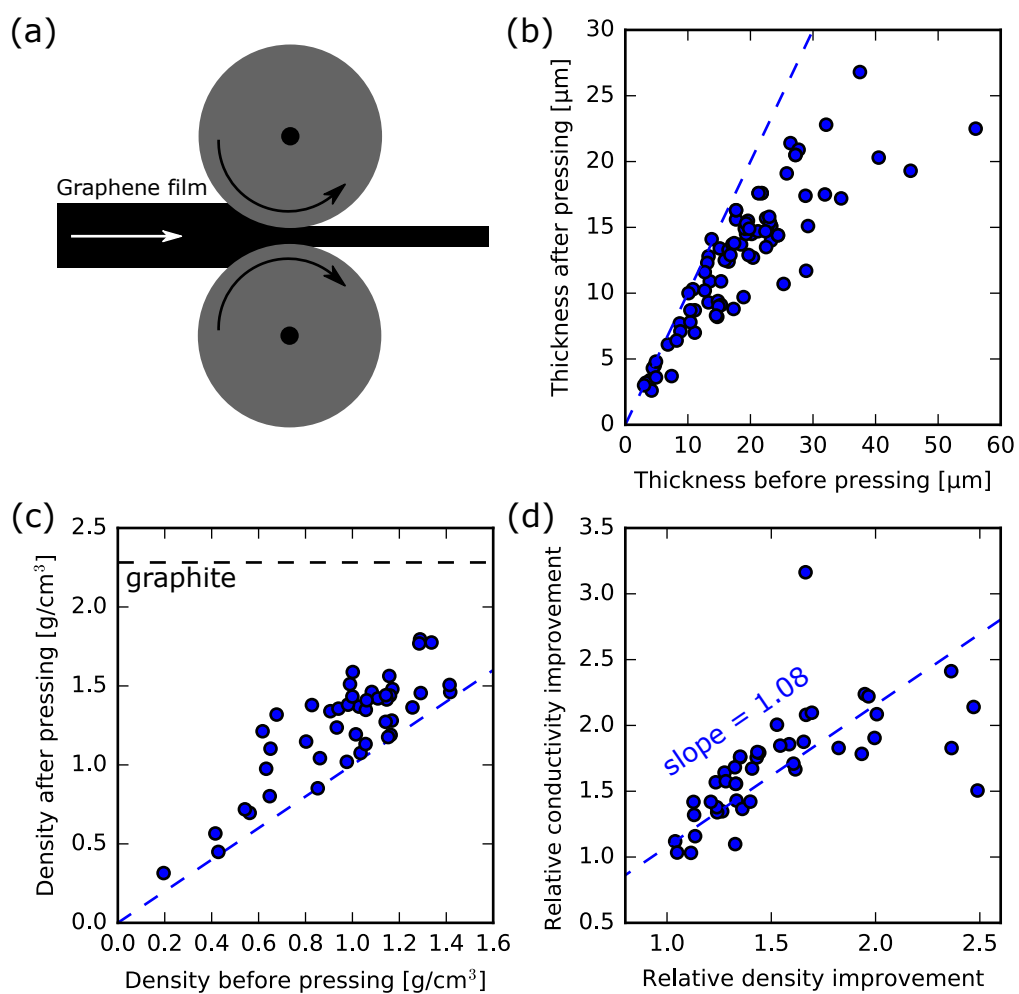


Figure 4.2.9: (a) Schematics of the rolling press process. (b) Thickness and (c) density before and after mechanical pressing. The dashed blue lines indicate unchanged quantities. The density of graphite is indicated in (c). (d) Comparison of the relative density and conductivity improvements.

4.3 Characterization

4.3.1 Structural characterization

4.3.1.1 Scanning electron microscopy

Scanning electron microscopy (SEM) is used to image the internal structure and the surface of the graphene films. For very thin samples $< 1\text{ }\mu\text{m}$, the thickness measurement is also performed with SEM. On the inside of a graphene film, graphene flakes are arranged in a flat layered manner as shown in Figure 4.3.1 (a) and (b). The surface exhibits some roughness (c), which has to be considered when using top contacts. Figure 4.3.1 (d) shows the side of a rough film. The surface roughness translates into superstructures on the inside, which in turn are formed by aligned graphene sheets. Overall, this type of thin film morphology is typical of graphene films as reported in the literature [169, 83, 117, 65, 84, 164, 85]. It also confirms the assumption of stacked and aligned graphene sheets from the previous chapter.

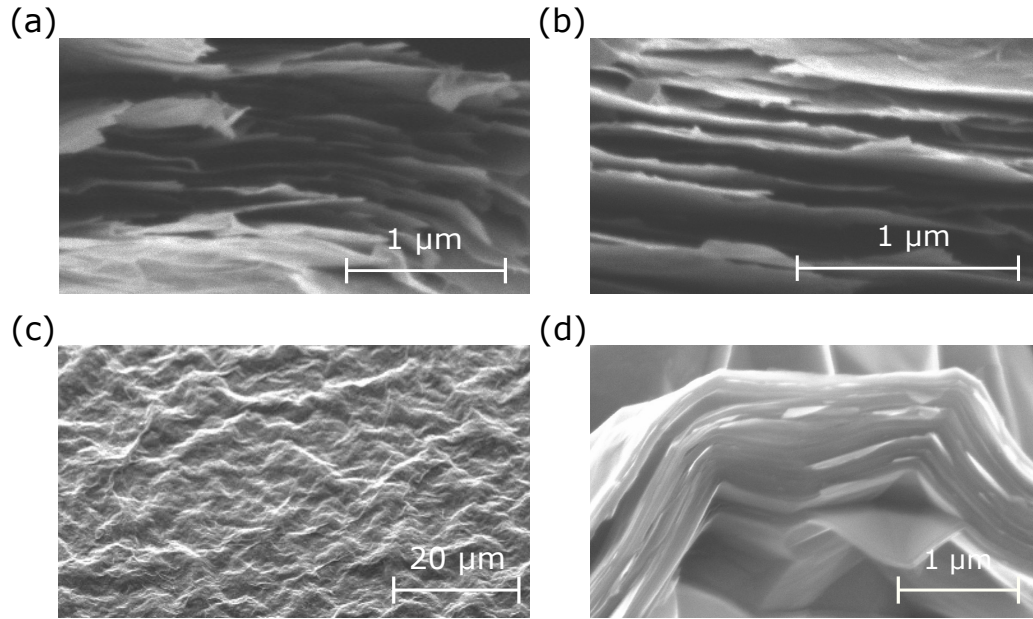


Figure 4.3.1: SEM micrographs. (a) and (b) Side views of the edge of a cut graphene film. (c) Surface of a graphene film imaged at a 54° angle. (d) Side view of a film with a rough surface.

4.3.1.2 Raman spectroscopy

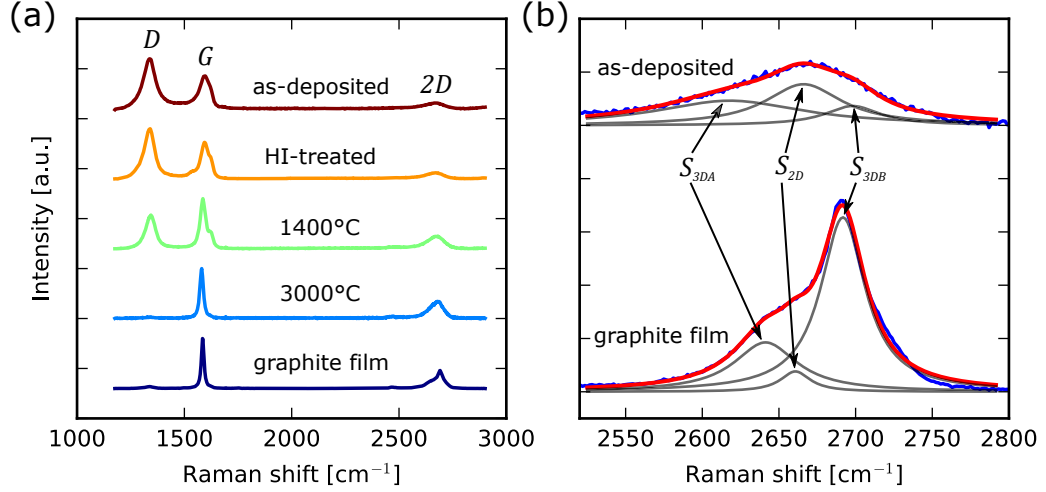


Figure 4.3.2: (a) Raman spectra of graphene films at different stages of processing. A graphite film is measured for reference. (b) Close-up of the 2D-peak and its sub-peaks. The raw data is shown in blue, the sub-peaks are black, and their sum is shown as the red line.

Raman spectroscopy is a standard tool to characterize graphene and its derived materials [170, 171, 172, 173]. The spectra contain a variety of information on chemical and physical properties. Although the information density is higher for mono- and few-layer graphene, Raman spectra of graphene films are also insightful to assess their quality and monitor the effect of post-treatment methods. In this work, Raman spectra are recorded with a Horiba LabRAM Aramis confocal Raman microscope at a laser wavelength of 633 nm. For each film, measurements are taken at five random positions. The background is removed and the spectra are averaged.

Figure 4.3.2 (a) shows the Raman spectrum of an as-deposited graphene film, its evolution during post-treatment, and the spectrum of a graphite film for comparison. Preparation details are listed in the Appendix 6.7.2.2. Apart from several smaller peaks, the characteristic *D*-, *G*-, and 2*D*-peaks can be identified at wavenumbers around 1340, 1580, and 2660 cm^{-1} respectively. A comprehensive explanation of the peak origins beyond the scope of this work is given in the reviews [172, 173]. The presence of a prominent *D*-peak is a sign of structural defects in the as-deposited film. However, the peak intensity decreases steadily during post-treatment due to the removal of residual oxygen and the restoration of the graphene lattice. Accordingly, the *G*-peak intensity increases, since the corresponding vibrational mode requires defect-

| Sample | $I(D)/I(G)$ | L_D [nm] | R^* |
|-------------------------------|-------------|------------|-------|
| Graphene film as-deposited | 1.81 | 21.2 | 0.74 |
| Graphene film HI-treated | 1.64 | 23.5 | 0.61 |
| Graphene film heated to 1400° | 1.08 | 35.7 | 0.66 |
| Graphene film heated to 3000° | 0.098 | 393 | 0.42 |
| Graphite film | 0.10 | 371 | 0.07 |

Table 4.1: Evaluation of the Raman spectra of graphene films

free carbon hexagons³. From the integrated intensity ratio of the D - and G -peaks $I(D)/I(G)$, the mean distance between defects L_D in nanometers can be determined according to [175]

$$L_D = 2.4 \cdot 10^{-10} \cdot \lambda^4 \cdot I(G)/I(D), \quad (4.3.1)$$

where λ denotes the laser wavelength in nanometers. Although not specifically derived for graphene-based macro-materials, the equation provides a solid point of reference and is commonly used to evaluate graphene films in the literature [73, 71, 13]. Applying equation (4.3.1) to the thin film spectra from Figure 4.3.2 (a), $L_D = 371$ nm is found for the graphite film and $L_D = 21.2$ nm for the as-deposited graphene film. This is in line with expectations as the random stacking of individual graphene flakes to obtain a thin film is much more likely to induce disorder and structural imperfections than the pressing of graphite. It also hints at potential damage of the graphene flakes that was introduced during the production of the raw material. When the as-deposited graphene film is subjected to post-treatment, the Raman spectrum evolves accordingly. Upon HI-treatment, the overall shape hardly changes, but $I(D)/I(G)$ decreases from 1.81 to 1.64, most likely due to the removal of remaining oxygen-containing functional groups that act as defect sites in the film. After subsequent thermal annealing at 1400°C for 15 minutes, $I(D)/I(G)$ further decreases to 1.08, indicating the healing of graphene defects as reported in the literature [166, 167, 176]. After annealing at 3000°C for 15 minutes, $I(D)/I(G)$ drops substantially to 0.098, suggesting nearly full defect healing. $I(D)/I(G) = 0.098$ translates to $L_D = 393$ nm, which even exceeds the large defect-free crystallite sizes in the graphite film. From the composition of the $2D$ -peak, the amount of turbostratic stacking can be extracted [177] as shown in Figure 4.3.2 (b). In pristine graphite, there are two sub-peaks S_{3DA} and S_{3DB} . A third sub-peak S_{2D} emerges due

³What appears to be a shoulder of the G -peak is the D' -peak. Similar to the D -peak, it requires a defect for scattering, but the associated lattice vibration belongs to a different phonon branch and the phonon wavevector is smaller. Hence, the D' -peak is also a sign of lattice defects, but with a lower intensity than the D -Peak [174].

to the layer misalignment when turbostratic stacking is present [172]. From the intensities of the individual sub-peaks, the share of turbostratic stacking R^* can be computed according to [177]

$$R^* = \frac{I(S_{2D})}{I(S_{2D}) + I(S_{3DB})}. \quad (4.3.2)$$

A higher value of R^* corresponds to a higher share of layer mismatch and thus a more graphene-like behavior of the building blocks. A lower value of R^* signifies more out-of-plane order and a higher similarity to crystalline 3D graphite. Correspondingly, $R^* = 0.07$ is obtained for the graphite film and $R^* = 0.74$ for the as-deposited graphene film. The share of turbostratic stacking remains high at $R_{\text{HI}}^* = 0.61$, $R_{1400}^* = 0.66$, and $R_{3000}^* = 0.42$ for an HI-treated film and graphene films annealed at 1400 and 3000°C respectively. This confirms the structural difference to graphite films as explained in section 2.2.2. However, comparing the initial $R^* = 0.74$ to $R_{3000}^* = 0.42$, some degree of graphitization takes place and the partial restoration of an AB-stacking sequence is observed, which is in line with the literature [75]. The results of the Raman studies are compiled in Table 4.1. The findings are consistent with literature reports where Raman spectroscopy is performed on graphene films [158, 73, 71, 13]: Graphene films are structurally similar to graphite films, but the degree of turbostratic stacking is substantially higher. HI- and heat treatment are confirmed as effective means to reduce defects and improve crystallinity.

4.3.2 Electrical characterization

4.3.2.1 Measurement method of the electrical conductivity

With the exception of section 3.4.5, the simulations focus on the spatially homogeneous current flow and the resulting electrical conductivity of the conductor material. This scenario corresponds to the situation in a power cable or a motor winding for example. In the simulations, the electric potential is computed at every overlap in the structure, which directly yields the voltage drop between arbitrary points. However, this approach is not transferable to real-world experiments, so that an alternative is required. The findings from section 3.4.5 show that contacting a GCM from the top is not ideal for every geometry. Thus, a non-invasive contactless eddy current method is selected for conductivity measurements.

In an eddy current measurement, a coil is brought in close proximity to a conductive material. An alternating current is passed through the coil such that an alternating magnetic field is induced. The field generates current

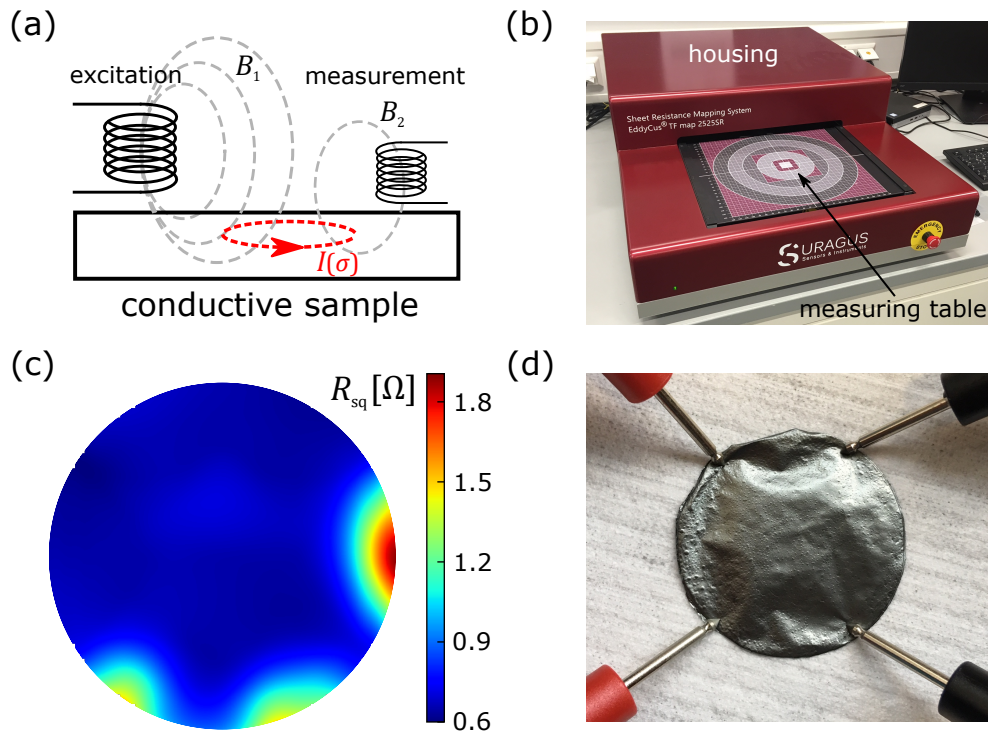


Figure 4.3.3: (a) Eddy current measurement concept. A magnetic field B_1 is generated by an excitation coil. It induces an eddy current $I(\sigma)$ in the conductive sample that depends on the sample conductivity σ . The eddy current induces a secondary field B_2 that is picked up by a second coil. (b) Eddy current measurement device. (c) Color-coded measurement of the sheet resistance R_{sq} of a circular graphene film. (d) Setup for a van-der-Pauw measurement.

flow in closed loops (eddy currents) inside the conductive material, which in turn induces a secondary magnetic field. The secondary field is probed with another coil as it contains the information about the electrical conductivity of the measured material.

The device used in this work operates at a frequency on the order of 10 MHz, allowing penetration depths of several hundred micrometers [178]. In preliminary tests, the manufacturer investigated the frequency-dependent conductivity of graphene films and found no change in the measured conductivity from the medium MHz regime down to the low kHz regime. Thus, the measured values are assumed identical to the DC conductivity as well⁴.

Figure 4.3.3 (a) - (c) illustrate the measurement technique, the measuring device, and an exemplary spatially resolved sheet resistance measurement. For a measurement, the sample is placed on a measuring table, which can move into and out of the housing. The excitation coil is located 3 mm above the table and moves perpendicular to the table's direction of movement. The measuring coil is located underneath the table. The combination of a moving table and moving coils enables spatially resolved conductivity measurements. While the focus is on average conductivity, spatial resolution enables the assessment of film homogeneity and the identification of defects. Apart from that, the advantages of an eddy-current measurement are the non-contact operation mode and the speed of the measurement. The non-contact mode eliminates the unknown influence of a contact pad or a probe tip. Additionally, the films remain untouched and undamaged. Joule heating due to the eddy currents is not observed. A spatially resolved sheet resistance measurement of a film with a 4-cm-diameter and a resolution of 1 μm only takes 2.5 minutes while providing an information depth that surpasses other methods by far. More information about eddy current measurements of electrical conductivity can be found in References [178, 180, 181].

The eddy current device is calibrated with metal foils and crosschecked with commercially available graphite and graphene films. Additional comparisons with four-point probe measurements in the style of van-der-Pauw [139] (Figure 4.3.3 (d)) show: The conductivities obtained with eddy current measurements correspond to homogeneous current flow in a conductor and match the four-point probe measurements of thin films in the 2D-regime.

⁴There are no systematic studies on the electrical conductivity of graphene films in the frequency range from DC to 10 MHz. However, there are published measurements on CVD graphene, which indicate a frequency independence in said regime [179].

4.3.2.2 Electrical conductivity results

| Supplier | As-deposited σ [Sm^{-1}] | HI-treatment σ [Sm^{-1}] | Thermal annealing σ [Sm^{-1}] |
|----------|---|---|--|
| #1 | 71000 | 132000 | 223000 |
| #2 | - | 46900 | 341000 |
| #3 | - | 9000 | 312000 |
| #4 | - | 7100 | 278000 |
| #5 | - | 4570 | - |
| #6 | - | 4460 | 96700 |
| #1 & #2 | - | - | 546000 |

Table 4.2: Highest electrical conductivities σ based on different commercial dispersions. Preparation details are listed in the Appendix 6.7.2.3.

The electrical conductivity of a graphene film depends heavily on the starting material and the post-treatment methods. A comparison of the highest conductivities achieved with different starting dispersions is given in Table 4.2. Note that only dispersion #1 is actual graphene (a mixture of mono- and few-layer graphene), the other dispersions are GO-based. Consequently, their conductivity only becomes substantial after reduction. Furthermore, the suppliers do not disclose the exact composition of their dispersions. They name the dispersion medium, the type of dispersed particles, average sizes, monolayer share and concentration, but no information about additives is provided. A detailed list of the available information on each dispersion is provided in the Appendix 6.5.

Two dispersions stand out in terms of conductivity. The graphene-based dispersion #1 provides the most conductive as-deposited films and also yields the record conductivity after HI-treatment. Among the GO-based dispersions, #2 provides the highest conductivities. After thermal treatment, it surpasses dispersion #1, which is most likely related to the flake sizes: As explained in section 2.1.1.4, monolayer GO flakes are typically larger than mass-produced graphene flakes by orders of magnitude. This is also the case for dispersions #1-6: The graphene dispersion contains flake sizes between 1 and $10\mu\text{m}^2$, while several GO dispersions feature average flake sizes of $> 100\mu\text{m}^2$. Prior to thermal annealing, the GO-based films still contain the defects from the reduction process, which severely limits the electrical conductivity. After thermal annealing however, the large flake sizes can be exploited and the GO films prepared from materials #2, #3, and #4

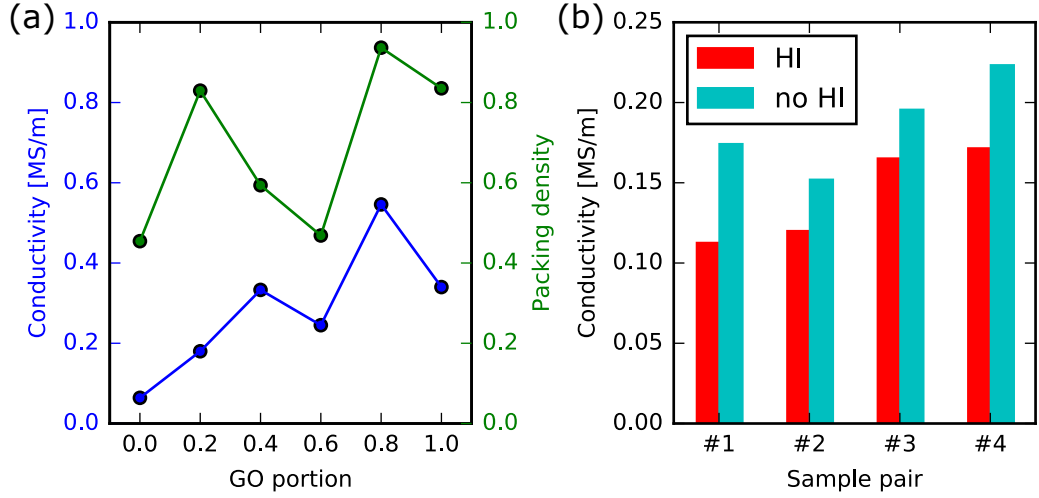


Figure 4.3.4: (a) Conductivities (blue) and packing densities (green) of GO/graphene mixed films after thermal treatment. (b) Conductivity comparison of films with (red) or without (cyan) HI-treatment prior to thermal annealing.

perform better than the graphene-based films⁵. Speaking in terms of the microscopic material parameters from the simulation, the in-plane and out-of-plane conductivities of the GO-based material can be improved, while the graphene-based material remains limited by its small flake size.

In an effort to surpass the limitations of the individual dispersions, mixtures of the best-performing materials are prepared. The idea is based on the results presented in section 3.4.4.2, where it is found that highly conductive flake overlaps can overcompensate poorly conductive connections. Hence, GO dispersion is mixed with graphene dispersion to profit from the large GO flakes for better out-of-plane connections and from the defect-free graphene flakes for a higher average in-plane conductivity. In a series of six films, the GO portion is systematically varied and the films are thermally annealed at 3000°C for 15 minutes. After the subsequent mechanical pressing, the conductivities and the packing densities are recorded. The preparation details are listed in the Appendix 6.7.2.4 and the results are presented in Figure 4.3.4 (a). The mixture of GO and graphene seems to be particularly effective when a high share of GO is combined with a low share of graphene. The best conductivity $\sigma = 546000 \text{ Sm}^{-1}$ is obtained in this way with 80% GO and 20% graphene. Apart from the original intent to improve both the average in-plane and out-of-plane connections, a structural advantage is also

⁵Material #5 did not allow thermal annealing at high temperatures. The films lose their mechanical stability and cannot be measured afterwards.

observed: The 80:20 GO:graphene mixed film features the highest packing density. A possible explanation is provided by Xin et al. in Reference [94], where a graphene fiber is synthesized from a combination of very large and very small flakes. Xin et al. suggest that the large flakes form the basic structure of the fiber, while the small ones fill voids with conductive material. They find the highest conductivity and packing density at a share of 30% small flakes, which is reasonably close to the 20% graphene share found here.

In the literature, HI-treatment is often performed prior to thermal annealing [100, 65, 13]. To assess the necessity of this procedure, six identical GO films and a pair of graphene films are prepared (see Appendix 6.7.2.5). Half of the films are reduced with HI and all the films are thermally treated at 3000°C for 15 minutes. The results are visualized in Figure 4.3.4 (b). After annealing, all HI-treated films exhibit a slightly lower conductivity than their counterparts, even though the densities are similar. This suggests that a purely thermal reduction is as effective or even more effective than a chemical reduction. The following considerations could provide an explanation: At 3000°C, no foreign species are expected to remain inside a graphene film, neither the oxygen-containing functional groups, nor the residual iodine from HI-treatment. Hence, HI-treatment only provides benefits for non-annealed films, but it is unnecessary before high-temperature annealing.

It is possible that for the material used in the literature, an HI-treatment before thermal annealing is beneficial, but in this work, no such indication was observed. Consequently, the necessity of a chemical reduction before thermal treatment should be assessed on a case-by-case basis.

Since post-treatment plays a decisive role, the efficacy of the three methods introduced above is evaluated. The conductivities of 233 films treated i) only with mechanical pressing ii) with HI or iii) thermally followed by mechanical pressing are compiled and compared in a histogram in Figure 4.3.5. Three levels of conductivity improvement can be distinguished. As explained in section 4.2.4, pressing by itself only removes cavities and thus reduces the overall film thickness. This can be interpreted as a geometrical effect and by itself, it leads to the smallest improvements in conductivity. HI-treatment, on the other hand, removes oxygen-containing functional groups and reduces the film thickness at the same time, surpassing pure geometrical enhancements. The highest conductivities however are achieved with thermal treatment at temperatures above 2500°C. The removal of oxygen-containing species in combination with the restoration of the hexagonal lattice is the most effective treatment by far. The data in Figure 4.3.5 covers all the different fabrication methods and materials that were used in this work. As a consequence, the conductivities are widely spread, especially for thermally annealed films.

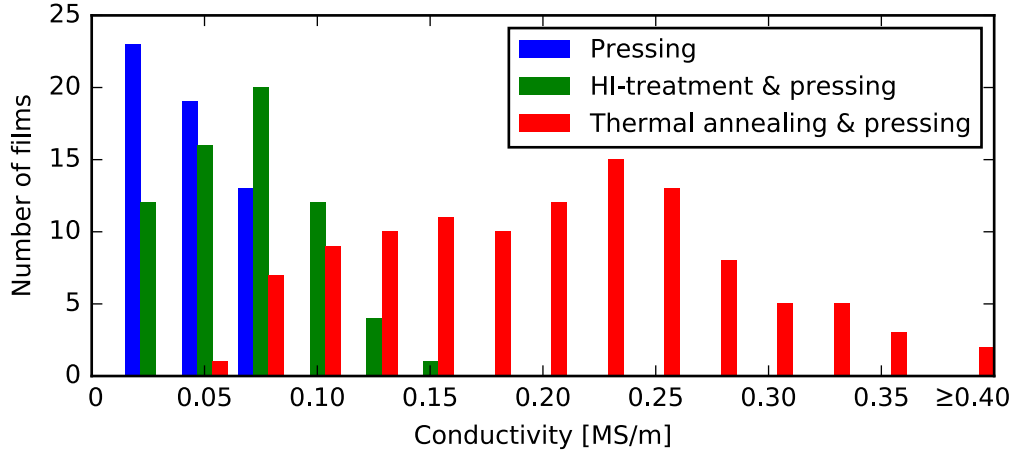


Figure 4.3.5: Conductivities of graphene films after post-treatment.

After refining the process steps however, conductivities between 240000 and 300000 Sm^{-1} could be reproducibly obtained.

The highest conductivity achieved in this work is 546000 Sm^{-1} (80% dispersion #2 and 20% dispersion #1), which corresponds to $\sim 50\%$ of the record values in the literature [79, 65, 73]. The remaining difference could stem from the source material. Most research groups prepare and optimize their own graphene or GO dispersions starting from graphite, whereas only commercial dispersions are used in this work. For even higher conductivities, post-treatment might need to be tailored to the specific starting material or vice versa.

The conductivity results of GO- and graphene-based films are in line with the understanding of electrical conduction in GCMs as presented in the first part of this work. While graphene-based films initially show a superior conductivity due to fewer defects, they are surpassed by GO-based films after defect healing, likely due to the larger flakes obtained during GO production. There seem to be different degrees of limiting factors for the conductivity of GCMs. Some, such as a limited in-plane conductivity, can be mitigated by post-processing, while others, such as the flake size, are fixed once the film is deposited. The latter ones are the more severe obstacles, and should be prioritized during optimization.

4.3.2.3 Temperature-dependence

As outlined in section 2.2.2, undoped graphene films are expected to exhibit a negative TCR around room temperature, which would be a sign of thermally activated transport. To verify this, an exemplary temperature-dependent resistance measurement is performed on a graphene film. The contact de-

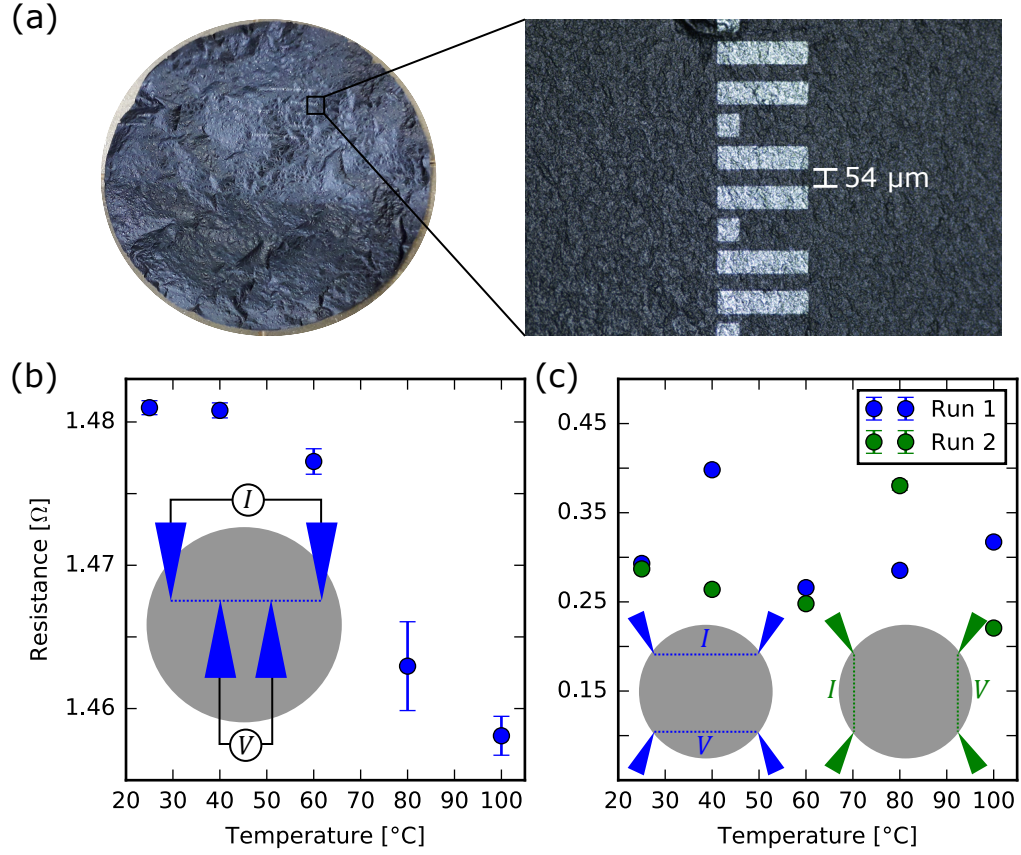


Figure 4.3.6: (a) Graphene film after annealing at 300°C in air with a close-up of the palladium contacts. (b) Temperature-dependent in-line four-point resistance. The inset shows the probe arrangement. (c) Temperature-dependent square four-point resistance. The insets show the probe arrangement during the individual runs.

position and electrical measurements were conducted externally by Martin Hartmann, in the lab of Sascha Hermann at the Center for Microtechnologies, TU Chemnitz. The graphene film was prepared as part of this thesis and as outlined in detail in the Appendix 6.7.2.6. This section is not intended to present a comprehensive study. It is rather a first test, where interesting trends are already emerging.

For a stable electrical contact, palladium contacts with a thickness of 50 nm are deposited on a graphene film. Subsequently, the sample is annealed at 300°C in air. At 200°C , water vapor escapes the film, creating some bubbles and a rougher surface. An image of the film and a close-up of the contacts are shown in Figure 4.3.6 (a).

In a first study, the metal pads are contacted in an in-line four-point configu-

ration and current is swept from $I = -1$ mA to $I = 1$ mA. From the voltage drop V , the resistance is computed according to $R = V/I$. The temperature is increased from 25 to 100°C and a slight but systematic decrease of the resistance is observed. While the data does not allow a linear fit, it shows a clear downward trend, i.e. a negative TCR. The data is shown in Figure 4.3.6 (b).

In a second study, the same film is contacted directly and not via the metal pads. The four probes are arranged in a square configuration close to the film edge and slightly puncture the surface for good contact. Current is applied between two probes and the voltage drop is measured parallel to it. The configuration is rotated by 90° in a second run as shown in Figure 4.3.6 (c). Thus, the sheet resistance and the in-plane conductivity anisotropy are obtained. Similar to the first study, the temperature is increased from 25 to 100°C, but no systematic dependence is observed. The statistical errors from the resistance calculation cannot explain the large variation of the data. It is more likely that the contact quality is an additional source of error, since no metal pads are used and the probes are reset for each measurement.

Evaluating the measurements at room temperature, no in-plane anisotropy is found, which corresponds to the expectation⁶. The measured four-point resistance $R = 0.29 \Omega$ translates to a conductivity $\sigma_{4P} = (37300 \pm 1900) \text{ Sm}^{-1}$ that is consistent with the value $\sigma_{ec} = (37600 \pm 1100) \text{ Sm}^{-1}$ as measured with the eddy current technique. The total uncertainty of the four-point measurement comprises the statistical data analysis error of 0.1% as well as a systematic positioning error estimated at 4%, and the error on the thickness measurement estimated at 3%. The uncertainty of the eddy current measurement is dominated by the error of the thickness measurement.

Despite the preliminary character of this study, the temperature-dependent four-point measurement is in line with the expected graphene film properties. Electrical transport seems thermally activated, no in-plane anisotropy can be observed, and the electrical conductivity agrees with the eddy current measurement. A stable top contact without metal pads appears to be challenging.

4.4 Comparison with the simulation

For a direct comparison of experiment and simulation two studies are conducted. The microscopic properties of graphene films are systematically varied, the resulting total conductivity is measured and then compared to the prediction from the simulation.

⁶An in-plane isotropy marks an important difference to fiber-based materials [182, 183]

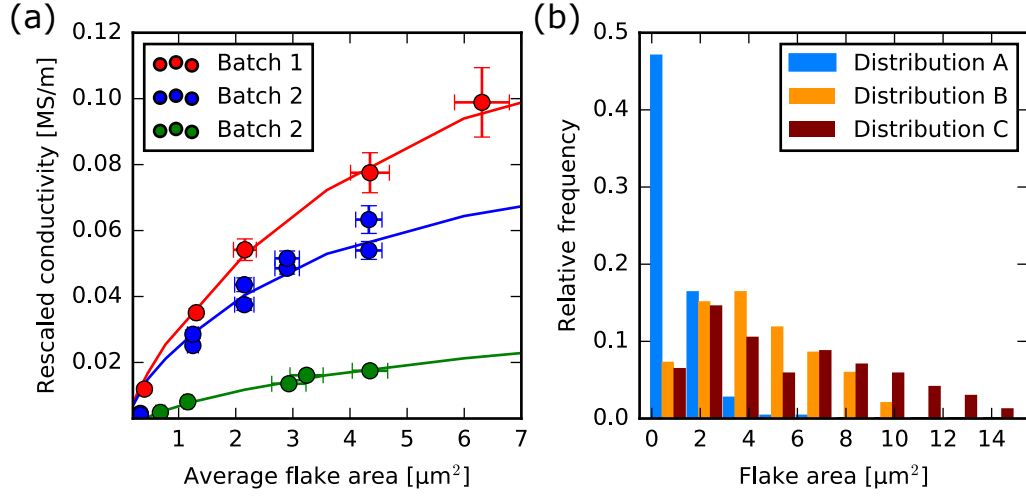


Figure 4.4.1: (a) Conductivity of graphene films σ_{tot}/p as a function of the mean flake area. The solid lines correspond to the simulation, the circles represent measured experimental values. (b) Exemplary flake size distributions from the experiment. They vary from skewed and narrow (A) to nearly symmetric (B) and wide (C).

In the first study the flake sizes are investigated. Three batches of thin films are prepared from a graphene dispersion as explained in section 4.2. The detailed preparation protocol is found in the Appendix 6.7.2.7. With a centrifugation cascade, each batch is divided into five portions, each one with a different average flake size. From these portions, the films are deposited via vacuum filtration (one film per portion in batches 1 and 3, two films per portion in batch 2). The dispersion for batch 1 is processed immediately after receiving the product, batch 2 is processed two weeks later, and batch 3 is processed another four weeks later. The processing of a single batch takes 1-2 days. The electrical conductivity of the films is measured directly after the film deposition without further post-treatment. This is to keep the processing conditions as consistent as possible and to avoid sources of systematic errors such as pressing, which is more efficient for thicker films as shown in section 4.2.4.

In accordance with section 3.4.4.3, the measured input parameters for the simulation are the packing density, the average flake size, and the total electrical conductivity. Just as before, the in-plane and out-of-plane conductivities of individual flakes are determined via a fitting routine, under the assumption that these values have to remain constant within a single batch. Since there are more data points than in section 3.4.4.3, the procedure is more precise. Figure 4.4.1 (a) compares the simulation and the experimental results.

Since the films exhibit different packing densities p , the measured and the simulated conductivities are rescaled $\sigma_{\text{tot}} \rightarrow \sigma_{\text{tot}}/p$ for easier comparison. The experimental data is in good agreement with the prediction from the network model. For the smallest flake sizes in batches 1 and 2, there is a slight deviation, but the other films meet the expectations. The fitted out-of-plane conductivities are in the range of twisted bilayer graphene, similar to the values extracted from the literature (see Figure 3.4.11). The detailed fitting parameters are presented in the Appendix 6.6. The measurement errors on the conductivity and on the density are dominated by the precision of the thickness measurement with the micrometer gauge. Thus, the relative error is larger for thinner films. A crosscheck with a different measurement method can reduce this error. The error on the average flake size corresponds to the estimated statistical error s/\sqrt{m} with the sample standard deviation s and the number of measured flakes m . It can be reduced by measuring more flakes or employing additional methods such as dynamic light scattering [145].

There is a systematic conductivity decrease from batch to batch, which could be linked to an aging process. Over time, graphene flakes tend to agglomerate in a dispersion, so that the average layer number is increased, which in turn reduces the average in-plane conductivity. Consequently, the older the material, the lower the conductivity.

Although only average flake sizes are used as input parameters for the simulation, the distributions of the flake sizes are investigated as well. An exemplary selection is shown in Figure 4.4.1 (b). The distributions vary from narrow to wide, and from heavily skewed to nearly symmetric. Nevertheless, the average flake size suffices as input parameter for the simulation. This finding agrees with the conclusion drawn in section 3.4.4.1: Within the distribution variation presented here, it is not necessary to consider the exact size distribution; mean values are sufficient. It stands to reason that at a certain point, this approximation is not valid anymore. The case of Reference [94] could be an example, where extremely large flakes are combined with extremely small flakes. In that case, there are most likely no flakes which are actually close to the average flake size. However, for all the distributions investigated in this work in both simulation and experiment, the approximation seems to hold. In the second study to compare simulation and experiment, non-conductive elements are incorporated in the conductive graphene films, similar to section 3.4.4.2. To this end, aqueous GO dispersion is ultrasonicated and subsequently mixed with aqueous graphene dispersion. Preparation details are listed in the Appendix 6.7.2.7. The sonication ensures that the GO flakes are similar in size to the graphene flakes so that the two components mix well, which leads to a homogeneous appearance of the films. Without the

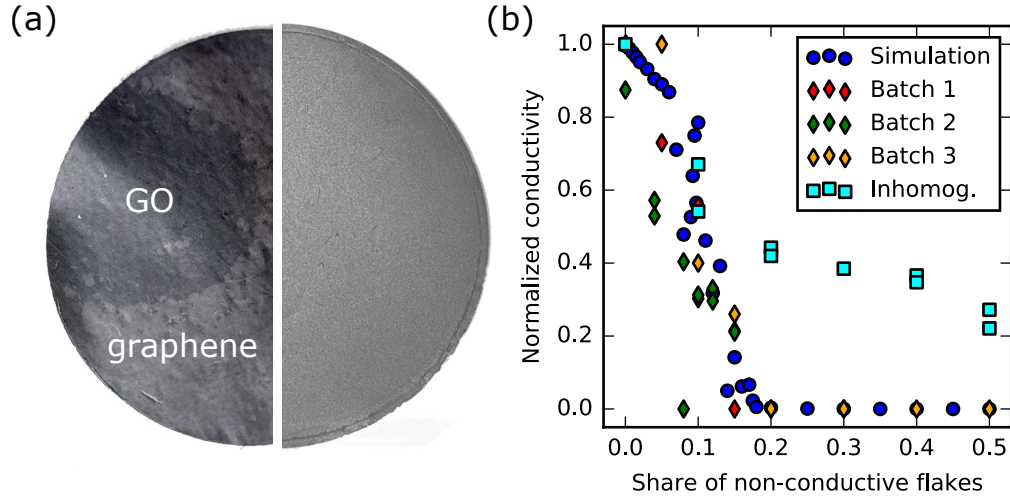


Figure 4.4.2: (a) GO/graphene film inhomogeneously (left) and homogeneously (right) mixed. In the inhomogeneous case, two phases can be distinguished. (b) Normalized maximum conductivity as a function of the share of non-conducting flakes. The blue circles correspond to the simulation, the diamonds show the experimental results. Inhomogeneously mixed films are represented by the square symbols.

sonication, two phases form and the films appear patchy. Both situations are shown in Figure 4.4.2 (a). In three batches, the share of non-conductive GO flakes is systematically varied between 0.5% and 50%, and the measured conductivities are compared to the simulation. For each batch, a film without GO flakes is synthesized to define the potential maximum conductivity. The results are shown in Figure 4.4.2 (b). As in the first study, the experiment and the simulation are consistent. In the simulation, there is a steep drop in electrical conductivity around 10% GO-share. The drop is less abrupt in the experiment, but it is also centered around 10%. Above a 20% share of GO-flakes, the measuring device does not detect a finite electrical conductivity anymore. As stated in section 3.4.4.2, the homogeneously dispersed GO flakes correspond to the worst case scenario. In Figure 4.4.2 (b), inhomogeneously mixed GO/graphene films are shown as well. In that case, the conductivity levels off a lot slower, because fully conductive channels remain intact, even for higher shares of GO.

Both experimental studies support the theory of microstructure-dependent electrical conductivity that is put forward in this work. The measured conductivities do not only correspond to the simulated curves, the amount of data is also much larger and statistically more reliable than what is found in the literature.

5 Conclusion and Outlook

5.1 Conclusion

In the course of this thesis, the electrical conductivity of graphene-based conductor materials (GCMs) was studied for the first time both in simulations and in experiments. To model the conductivity, an analytical approach, FEM, and a novel random resistor network model were applied. The simulations established quantitative relations that describe how the macroscopic conductivity of a GCM depends on its microscopic material parameters. Furthermore, the findings from the simulations lead to the important conclusion that GCMs have the potential to outperform metals in conductor applications. In the experimental part of this work, graphene-based thin films were synthesized. Various fabrication methods were tested and suitable characterization techniques were identified. Electrical conductivity measurements of thin films with systematically varied microscopic parameters agreed with the predictions of the simulations.

Simulations

The analytical model of a simplified graphene conductor quantifies the influence of the following material parameters on the macroscopic electrical conductivity: graphene flake in-plane conductivity, graphene flake out-of-plane conductivity, packing density, and flake size. The interplay of the quantities is such that the flake size and the out-of-plane conductivity can compensate each other, while the packing density and the in-plane conductivity must both be maximized for optimum results. The maximum possible electrical conductivity of a GCM is ultimately limited by the product of packing density and in-plane conductivity. Although simplified, the analytical model provides the first mathematical formula of GCM conductivity. It captures fundamental relationships and enables quick quantitative estimates. Computations with FEM confirm the trends and the conductivity limit determined with the analytical model. In addition, structural aspects are taken

into account by introducing defects and modeling irregularly shaped graphene flakes. The essential discovery in this regard is that even a disordered or defective structure can reach the theoretical maximum conductivity if the building blocks are spatially homogeneously distributed. Conversely, structural defects that represent spatial inhomogeneities lower the GCM conductivity beyond the reduced packing density.

The FEM studies in this work reveal an additional structural property that can be particularly relevant to the manufacturing process of GCMs: an anisotropic flake arrangement. Aligning the long sides of graphene flakes in a GCM with the current flow leads to an overall conductivity increase and vice versa.

To overcome the drawbacks of other simulation methods, a novel network model is conceived and implemented. It is tailored to the efficient modeling of a GCM's conductivity and allows for system sizes of more than 50000 flakes per structure. In contrast to other simulation methods that operate on this scale, all flakes can be manipulated individually. A parallelization of the geometry and network generation reduces the computation time considerably. The network model is set up in accordance with the FEM and requires an empirical parameter to compensate for the simplification of the in-plane conductance.

The findings of the analytical model and the FEA are substantiated by the network model. Despite the different degrees of complexity, there is great accordance among the different methods. Going beyond the confirmation of the initial results, the network model is used to simulate statistical distributions of physical quantities.

While a wide distribution of the out-of-plane flake conductivities can be favorable for a GCM, a statistical distribution of the in-plane flake conductivities is always detrimental. When 10% or more non-conductive elements are incorporated into a GCM, a substantial drop of the total conductivity is observed. As a function of the non-conductive material fraction, the conductivity drop follows a power law, which is typically found in percolation theory [123]. However, percolation studies usually focus on the transition from a low conductivity regime to higher conductivities. In this thesis the high conductivity regime is investigated instead, as it is more relevant for conductor applications.

Regarding statistical distributions of graphene flake sizes in a GCM, the network model shows that the exact size distribution has a negligible influence, but that the average flake size is a decisive quantity. The same flake size scaling behavior as in the analytical model and in the FEA is found.

Due to its versatility, the network model is easily extendable, e.g. to include multiphysics, and transferable to other systems than GCMs. Furthermore,

various measurement scenarios and arbitrary contact configurations can be modeled as shown in a top contact study in chapter 3.4.5. The study represents the first instance of a top contact simulation of a layered material built from anisotropically conductive components.

Experiments

A process chain for the synthesis of graphene-based thin films is set up. All the process steps are tailored to the processing of liquid dispersions, which would also be required for a large-scale production. The process chain starts with a commercial water-based graphene or GO dispersion, which is treated by means of ultrasound and centrifugation, and from which films can be filtrated or blade coated. Post-treatment, especially thermal annealing at high temperatures, has a strong positive impact on the electrical conductivity of the thin films. A non-contact eddy current method provides the most practicable conductivity measurements, as it is fast, non-invasive, and offers spatial resolution.

When comparing the dispersions of different manufacturers, the experiments suggest that without high-temperature treatment, defects in the graphene flakes dominate the overall performance and pure graphene performs better than reduced GO. However, if thermal annealing is carried out, the large flakes of the GO starting material cause the conductivity of reduced GO films to be better than that of graphene films. The highest conductivity obtained in this work is 546000 Sm^{-1} , which is achieved by mixing GO and graphene base materials at an 80:20 ratio.

HI effectively reduces thin films produced from GO. It also increases the conductivity of graphene films, likely by incorporating iodine which acts as a dopant. When a high-temperature thermal treatment is performed, no benefit from a previous HI treatment can be observed, regardless of the base material.

Two experimental studies support the theory of the microstructure-dependent electrical conductivity that is established in the simulation part. They are based on a considerably larger dataset than what is found in the literature. Strong agreement between simulation and experiment is found for both the dependence of the conductivity on flake sizes and on the share of non-conductive flakes in a GCM.

This thesis goes beyond the state of the art at various points. The simulations are the first quantitative conductivity simulations of GCMs in general. Thus, the numerous findings from the simulation studies are largely new or quantify relations that were previously only known on a qualitative level.

Furthermore, the exceptional agreement between the three modeling methods substantiates the validity of the results. In the experimental part, the first systematic investigation of various influencing factors was carried out. In particular, the crucial flake size dependence of the electrical conductivity was successfully quantified. The amount of collected experimental data and the depth of the analysis surpass previous work.

However, the most important contribution of this thesis is the connection of simulation and experiment. By combining both parts, a coherent picture emerges that thoroughly explains which parameters determine the electrical conductivity of a GCM. Fundamental trends and limits are revealed and mechanisms for the systematic optimization become available. The findings of this work do not only deepen the general understanding of electrical conduction in GCMs, but also lead to concrete guidelines for their production as presented in section 3.4.7. The network model in particular provides a new tool to identify and exploit the potential conductivity limits of specific GCMs, which is demonstrated in section 3.4.6. Overall, this work represents the first comprehensive evaluation of GCMs regarding their potential in conductor applications.

5.2 Outlook

Despite the promising conclusion, this thesis has also exposed a number of open points regarding material optimization and processing of GCMs.

First and foremost a suitable dopant is needed to make the GCM conductivity competitive. Depending on the application, different levels of conductivity are required. An overhead power line for example can get by with a lower conductivity than a motor winding. The cross section of the power line could be easily enlarged to achieve the desired conductance, while a motor is heavily optimized in terms of size and an increased winding cross section is not possible. The existing knowledge about GICs should be utilized and the most promising dopants in this field should be tested first. Besides experiments, atomistic simulations could support the search for a suitable dopant. The doped GCM needs to be stable in air and at elevated temperatures. Additionally, the dopant itself should not be harmful to humans or the environment. Processing-wise, it should be verified whether there are dopants which have a catalytic effect on defect-healing in graphene or reduced GO flakes.

GCM processing will become much simpler and cheaper if non-oxidized graphene flakes $\gg 10\text{ }\mu\text{m}^2$ become accessible. The flakes will unlock the full potential of the GCMs, and cost-intensive processing via GO to obtain large flakes can be avoided. Different approaches in this regard have been reported

[184, 39], but it remains to be seen which technology will be successful. As an alternative to large flakes, high quality small flakes can be connected by polymers [164], which would also avoid a reduction step and cost-intensive defect healing. However, if processing via GO continues to provide the highest electrical conductivity, reduction and defect healing methods should be improved to reduce costs. Alternatives to chemical reduction include microwave or ultraviolet radiation [185, 186, 187, 188], while current annealing can substitute high-temperature annealing [189, 190].

Two major topics related to GCMs have not been addressed in this thesis and still require comprehensive studies. First, thermal properties such as the thermal conductivity or material degradation related to heating need to be investigated. Ideally, this is done in multiphysics simulations, where electrical and thermal properties are considered simultaneously, as well as in experiments. The second topic concerns alternating currents (AC). There is reason to assume that GCMs offer substantial advantages in high-frequency applications. Thin films are already studied for flexible antennas [77, 78] and radiofrequency filters [79], but graphene-based cables might also be advantageous: In a resistor network model, the flake-to-flake transitions, which are less conductive than the flakes themselves, could be regarded as capacitors that become more conductive with increasing frequency. It should further be studied whether strong skin and proximity effects are expected in a GCM. Processing-wise, GCMs should be well-suited to fabricate multistrand cables such as Litz wires. Graphene fibers are easily spun with small cross-sections and twisted into yarns [12]. In contrast, conventional metal wires have to be thinned down in cost-intensive processes. A sound statement on the particular benefits of GCMs in AC applications can be an additional driver in further material development.

6 Appendix

6.1 Convergence tests of the network simulation

The convergence of the network simulation was evaluated for the relevant geometric parameters to derive the requirements for robust results.

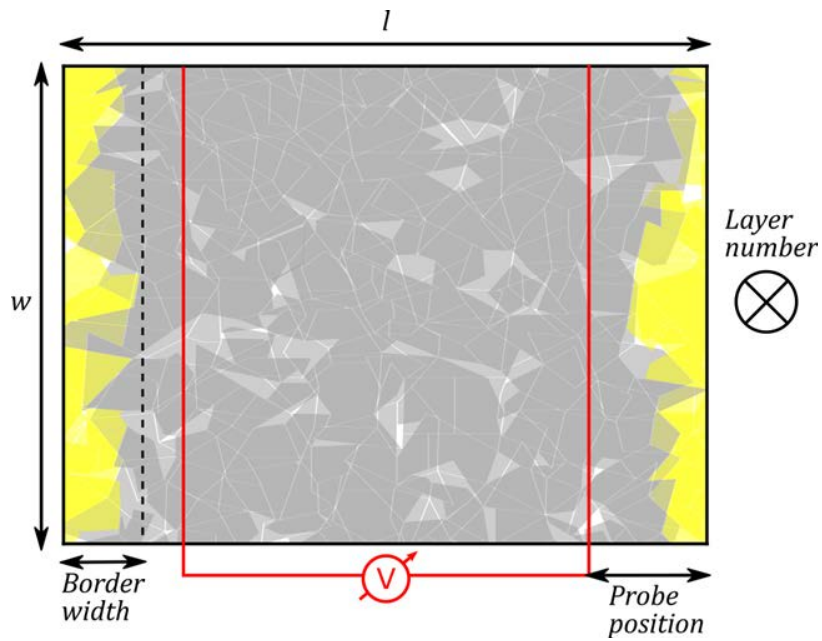


Figure 6.1.1: Overview of variable dimensions and parameters in simulated GCMs. Adapted with permission from [114].

1. Width of the GCM

Parameters: w = varying, $l = 50\text{ }\mu\text{m}$, layer number = 30, border width = $8\text{ }\mu\text{m}$, average flake diameter = $6\text{ }\mu\text{m}$, probe position = $14\text{ }\mu\text{m}$

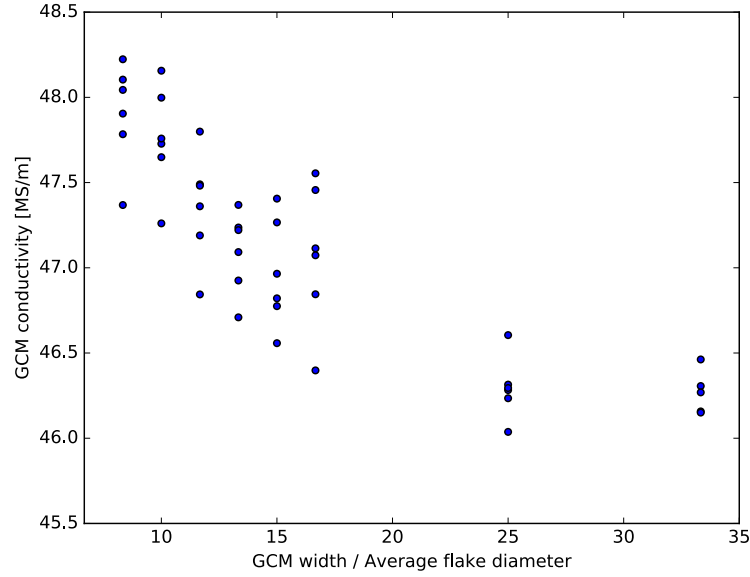


Figure 6.1.2: Variation of GCM width. Adapted with permission from [114].

2. Length of the GCM

Parameters: $w = 50\text{ }\mu\text{m}$, l = varying, layer number = 30, border width = $8\text{ }\mu\text{m}$, average flake diameter = $6\text{ }\mu\text{m}$, probe position = $14\text{ }\mu\text{m}$

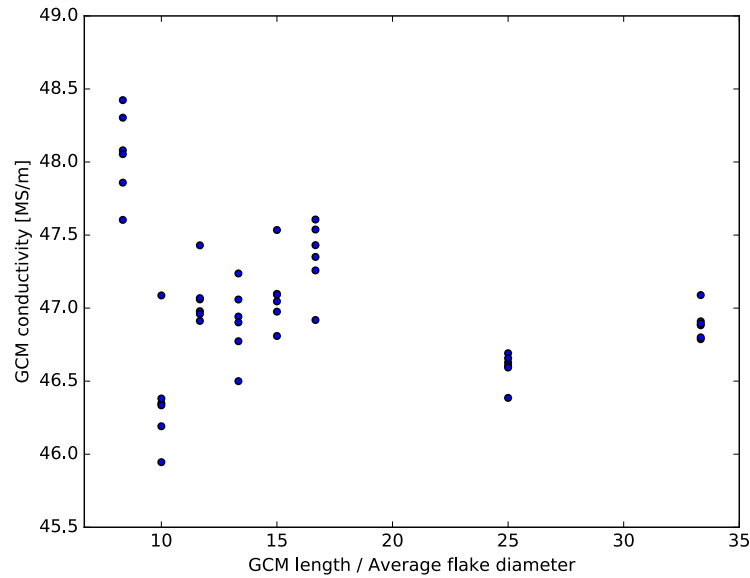


Figure 6.1.3: Variation of GCM length. Adapted with permission from [114].

3. Layer number

Parameters: $w = 50\text{ }\mu\text{m}$, $l = 100\text{ }\mu\text{m}$, layer number = varying, border width = $8\text{ }\mu\text{m}$, average flake diameter = $6\text{ }\mu\text{m}$, probe position = $14\text{ }\mu\text{m}$

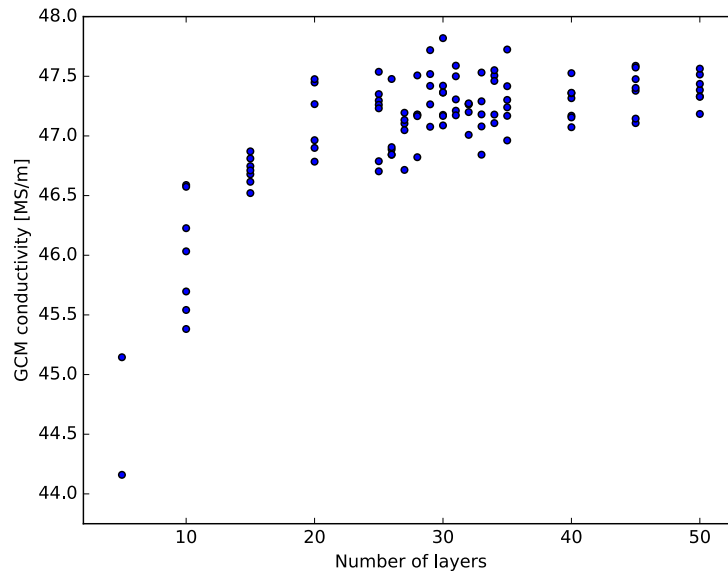


Figure 6.1.4: Variation of the GCM layer number. Adapted with permission from [114].

6.2 Different flake size distributions compared in section 3.4.4.1

Figure 6.2.1 shows representative simulated distributions of flake sizes in a GCM obtained by manipulating the maximum flake area and/or the maximum perimeter of the generated graphene flakes.

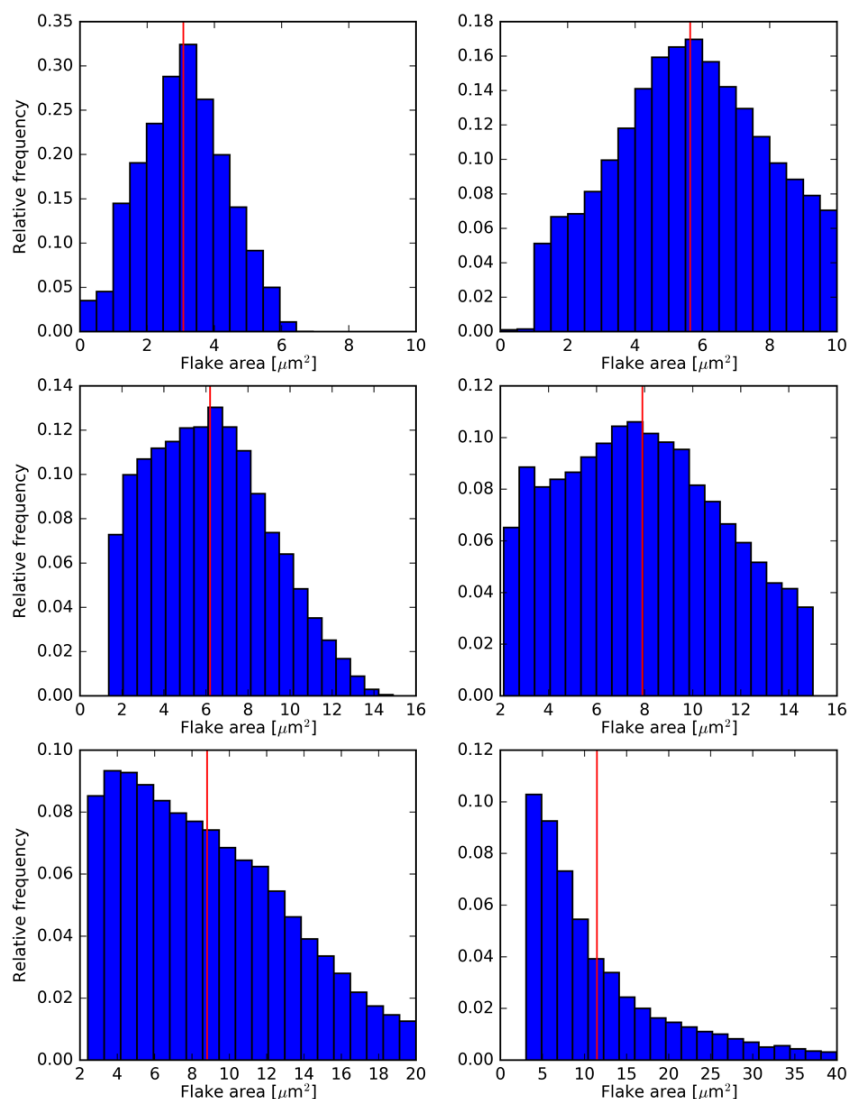


Figure 6.2.1: Exemplary flake size distributions at a packing density of $p = 0.8$ with indicated mean values. Reprinted with permission from [113]. Copyright 2018 American Chemical Society.

6.3 COMSOL Multiphysics[®] settings

Meshing

| | |
|--|------------------|
| Mesh type | Free Tetrahedral |
| x - and y -direction scaling | 1 |
| z -direction scaling | 5000 |
| Smooth across removed control entities | Yes |
| Number of iterations | 4 |
| Maximum element depth to process | 4 |
| Tessellation | Automatic |
| Optimization level | Basic |

Table 6.1: Meshing parameters

Solver

| | |
|---------------------------------|---------------------------|
| Solution approach | Fully Coupled |
| Solver type | Stationary iterative |
| Solution method | GMRES |
| Iterations before restart | 50 |
| Preconditioning | Left |
| Residual tolerance | 0.01 |
| Maximum number of iterations | 10000 |
| Factor in error estimate | 400 |
| Check error estimate | Automatic |
| Maximum intermediate iterations | 100 |
| Multigrid Solver | Geometric multigrid |
| Number of iterations | 2 |
| Multigrid cycle | V-cycle |
| Hierarchy | Lower element order first |
| Multigrid levels | 1 |
| Mesh coarsening factor | 2 |
| Assemble on all levels | Yes |
| Presmoothing / Postsmoothing | SOR / SORU |
| Coarse Solver | MUMPS |

Table 6.2: Solver settings

6.4 Derivation of the analytical expression for the resistance measurement with top contacts

Consider the structure depicted in Figure 3.4.13 (a) with length l , thickness t , width w and equidistant line-like probes with a spacing s . The material is considered to be homogeneous and isotropic with resistivity ρ , the length of the structure is assumed large compared to the probe spacing $l \gg s$.

3D isotropic case

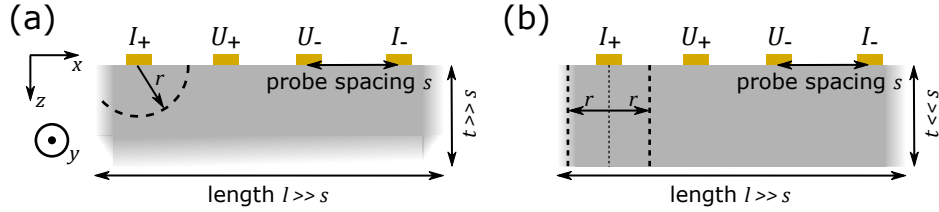


Figure 6.4.1: Cross-section of a collinear four-point probe setup for the derivation of (a) R_{3D} and (b) R_{2D} . The x -, y -, and z -directions are indicated. The structures are extended into the y -direction. Current propagates from contact I_+ into the material as shown by the dashed lines.

Figure 6.4.1 (a) visualizes the 3D isotropic case. The thickness of the structure is large compared to the probe spacing. Current I spreads cylindrically into a homogeneous isotropic material, therefore at distance r_1 from an electrode, the current density j is given as

$$j = \frac{I}{\pi w r_1}. \quad (6.4.1)$$

The electric field E at this position equals

$$E(r_1) = \rho \cdot j = \rho \cdot \frac{I}{\pi w r_1} = -\frac{d\Phi}{dr}(r_1), \quad (6.4.2)$$

with the radial coordinate r and the electric potential Φ . By integration, the electric potential at the position \mathbf{p} at a distance r_1 from the electrode is obtained

$$\Phi(\mathbf{p}) = -\frac{\rho I}{\pi w} \log(r_1/r_0), \quad (6.4.3)$$

where $r_0 > 0$ denotes the distance to the zero potential. At a point \mathbf{p} , the voltage drop V between two electrodes (distances r_1 and r_2) is then given as

$$V(\mathbf{p}) = -\frac{\rho I}{\pi w} [\log(r_1/r_0) - \log(r_2/r_0)] = \frac{\rho I}{\pi w} \log(r_2/r_1). \quad (6.4.4)$$

Applying equation (6.4.4) to the case of a collinear four-point probe array as shown in Figure 6.4.1 (a), the measured voltage drop $U_+ - U_-$ between the two inner probes is given as

$$U_+ - U_- = \frac{\rho I}{\pi w} [\log(2s/s) - \log(s/(2s))] = 2 \log(2) \frac{\rho I}{\pi w}. \quad (6.4.5)$$

2D isotropic case

Figure 6.4.1 (b) visualizes the 2D isotropic case. The thickness of the structure is small compared to the probe spacing. Current I spreads as a constant plane into the homogeneous isotropic material, therefore at distance r_1 from an electrode, the current density j is given as

$$j = \frac{I}{2wt}. \quad (6.4.6)$$

Following the same considerations as before, the electric potential at the position \mathbf{p} at a distance r_1 from the electrode is obtained

$$\Phi(\mathbf{p}) = (r_0 - r_1) \frac{\rho I}{2wt}. \quad (6.4.7)$$

where r_0 denotes the distance to the zero potential again. The voltage drop V between two electrodes with distances r_1 and r_2 to the point \mathbf{p} is thus given as

$$V(\mathbf{p}) = (r_2 - r_1) \frac{\rho I}{2wt}. \quad (6.4.8)$$

In a collinear four-point probe array, the measured voltage drop $U_+ - U_-$ between the two inner probes is then given as

$$U_+ - U_- = (2s - s) \frac{\rho I}{2wt} - (s - 2s) \frac{\rho I}{2wt} = \frac{\rho I s}{wt}. \quad (6.4.9)$$

Anisotropic cases

To go from an isotropic to an anisotropic homogeneous material, the same approach as outlined in [139] is used: The x -, y -, and z -coordinates are transformed such that the anisotropic sample is mapped onto an equivalent

isotropic parallelepiped of resistivity ρ . The resistivity components of the anisotropic material ρ_x , ρ_y , and ρ_z are assumed to be directed along the x -, y -, and z -directions of the structure. The transformed coordinates x' , y' , and z' are given as

$$\begin{aligned}x' &= x(\rho_x/\rho)^{1/2} \\y' &= y(\rho_y/\rho)^{1/2} \\z' &= z(\rho_z/\rho)^{1/2}\end{aligned}$$

and $\rho = \sqrt[3]{\rho_x \cdot \rho_y \cdot \rho_z}$. As outlined in [139], the transformation preserves voltage and current, and thus the resistance. All the steps of the previous derivations for $U_+ - U_-$ can be carried out in the same way, but with transformed dimensions. With the probes aligned along the x -direction as before, the resistances $R = (U_+ - U_-)/I$ are rewritten as

$$\begin{aligned}R_{3D} &= 2 \log(2) \frac{\rho}{\pi w'} = \frac{2 \log(2)}{\pi w} \frac{\rho}{(\rho_y/\rho)^{1/2}} \\&= \frac{2 \log(2)}{\pi w} \rho^{3/2} \rho_y^{-1/2} \\&= \frac{2 \log(2)}{\pi w} (\rho_x \rho_z)^{1/2}\end{aligned}\tag{6.4.10}$$

and

$$\begin{aligned}R_{2D} &= \rho \frac{s'}{w't'} = \frac{s}{wt} \rho (\rho_x/\rho)^{1/2} (\rho_y/\rho)^{-1/2} (\rho_z/\rho)^{-1/2} \\&= \frac{s}{wt} (\rho_x \rho^3)^{1/2} (\rho_y \rho_z)^{-1/2} \\&= \frac{s}{wt} \rho_x.\end{aligned}\tag{6.4.11}$$

By replacing the resistivity with the conductivity according to $\rho_i = \sigma_i^{-1}$ with $i = x, y, z$, equations (3.4.14) and (3.4.15) are obtained.

6.5 Graphene and GO dispersions

| | | | |
|---------------------|---|---|-------------------------------|
| Dispersion | #1 | #2 | #3 |
| Manufacturer | Sixonia | Graphenea | GaoxiTech |
| Product | G-DISP-H2O-Et5-CS-1 | 947-768-1 | GO-3 |
| Dispersed particles | Graphene | GO | GO |
| Dispersion medium | Water/Ethanol 95/5 | Water | Water |
| Concentration | 1 mgml ⁻¹ | 25 mgml ⁻¹ | 10 mgml ⁻¹ |
| Layers | Few- and monolayer | > 95% monolayer | > 99.9% monolayer |
| Flake diameter | 1 – 5 μm , area < 10 μm^2 | D10 6 – 7 μm , D50 14 – 17 μm , D90 29 – 33 μm | 40 – 50 μm average |
| Oxygen content | unknown | 41-50% | unknown |

| | | | |
|---------------------|----------------------|--|-------------------------|
| Dispersion | #4 | #5 | #6 |
| Manufacturer | Ossila | Sigma-Aldrich | TimesNano |
| Product | M885 | 763705 | TNWGO-50 |
| Dispersed particles | GO | GO | GO |
| Dispersion medium | Water/IPA 50/50 | Water | Water |
| Concentration | 5 mgml ⁻¹ | 2 mgml ⁻¹ | 12.3 mgml ⁻¹ |
| Layers | Monolayer | Monolayer | > 98% 1-2 layers |
| Flake diameter | 1 – 50 μm | 22 μm average, D90 50 μm | > 50 μm |
| Oxygen content | unknown | < 54% | 35% |

Table 6.3: Disclosed properties of graphene and GO dispersions used in this work. The data is taken from technical data sheets provided by the manufacturers upon request or online.

6.6 Fitting parameters from the comparison of experiment and simulation

In Table 6.4, the fitting parameters for the curves shown in Figure 4.4.1 are compiled. The listed colors correspond to the colors in Figure 4.4.1. The fitted values of σ_{in} and σ_{out} match well with the literature data analyzed in section 3.4.4.3, Figure 3.4.11.

| Batch | σ_{in} [Sm^{-1}] | σ_{out} [Sm^{-1}] |
|-----------|---|--|
| 1 - red | 248000 | 0.06 |
| 2 - blue | 135000 | 0.11 |
| 3 - green | 62800 | 0.05 |

Table 6.4: Fitting parameters for the comparison of simulation and experiment

6.7 Process parameters for the preparation of graphene and GO films

In this section, the detailed process parameters for the preparation of selected thin films presented in this work are provided. They are referenced to the sections of the main text, where the corresponding results are discussed. As some of the films differ distinctly in their preparation, the preparation protocols are presented separately and not in a combined form. The nomenclature of the commercial dispersions is identical to section 6.5.

6.7.1 Standard procedures

Processes, chemicals, and materials that are employed repeatedly are described and labeled in this section.

Chemicals: For the dilution of dispersions #1, #2, #3, #5, and #6, deionized (DI) water is used. Dispersion #4 requires IPA as well.

Sonication is performed with a Bandelin Sonopuls HD4200 device with a power of 200 W. It is equipped with a TT 213 titanium plate.

Vacuum filtration is performed with a DURAN® filtering apparatus with a PTFE adapter for 47 mm films. The different membrane filters are:

- **PES1:** Polyether sulfone (PES) membrane, pore size 0.45 μm , Sartorius, 15406-4/—N

- **PES2:** Polyether sulfone (PES) membrane, pore size 0.45 μm , Millipore, Ref HPWP04700
- **Anodisc:** Alumina matrix membrane, pore size 0.2 μm , Whatman Anodisc 47, supported
- **MCE:** Mixed cellulose ester (MCE) membrane, pore size 0.45 μm , Whatman ME25

Blade coating is performed with a micrometer adjustable film applicator with a slit size range of 1 μm - 3 mm. Substrates are copper or PTFE. Dried films are carefully peeled from the substrate with a knife and can be cut into arbitrary shapes.

Standard HI process: Films are fully immersed in 57 wt.% HI without stabilizers. After 24 hours, films are taken out and washed with ethanol and water.

Standard 1400 annealing process: Under Argon flow, films are heated from room temperature to 1400°C at a rate of 5°C per minute. The temperature is fixed at 1400°C for 15 minutes and subsequently, the films cool down under Argon flow or in a vacuum.

Standard 3000 annealing process: Under Argon flow, films are heated from room temperature to 400°C at a rate of 6.33°C per minute. The temperature is fixed at 400°C for 15 minutes. Subsequently, the films are heated to 1200°C at a rate of 13.33°C per minute and then to 3000°C at a rate of 15°C per minute. The temperature of 3000°C is fixed for 15 minutes and subsequently, the films cool down under Argon flow or in a vacuum.

Pressing: Films are placed between two 120 μm -thick silicone-free transfer foils and pressed in an MTI HR01 rolling press. The rolling speed is set to 11.5 (arbitrary units of the device) and the separation of the rolls can be continuously varied between 0 and > 1 mm. Pressing is performed in several runs to reduce the film thickness gradually. The smallest separation of the rolls is listed in the preparation protocols.

6.7.2 Preparation protocols

In the centrifugation step, the supernatant is abbreviated as “SN” and the sediment as “SD”.

6.7.2.1 Film for SEM analysis

Film shown in Figure 4.3.1 and discussed in section 4.3.1.1

| Film | SEM1 |
|--------------------|--|
| Dispersion | #1, 10 ml |
| Centrifugation | 2000 rpm, 60 minutes Use SN, discard SD |
| Deposition | Vacuum filtration, PES2 |
| Further processing | Cut with a knife and place on sample holder for side-view image |

Table 6.5: Preparation protocol “SEM”

6.7.2.2 Films for Raman analysis

Films discussed in section 4.3.1.2

| Film | As-deposited | HI-treated | 1400 | 3000 |
|-------------------|---|-------------|----------------------------|---------------|
| Dispersion | #1, 80 ml per film | | | |
| Centrifugation | 500 rpm, 60 minutes | | | |
| | Discard SN Redisperse SD in 80 ml DI water | | | |
| Deposition | Vacuum filtration, PES1 | | | |
| HI treatment | - | Standard HI | | |
| Thermal treatment | - | - | Standard 1400 | Standard 3000 |
| Pressing | - | - | 20 μ m roll separation | |

Table 6.6: Preparation protocol “Raman”

6.7.2.3 Films with the highest electrical conductivity

Film conductivities shown in Table 4.2 and discussed in section 4.3.2.2

Supplier #1:

| Films | As-deposited | |
|-----------------------|---|--|
| Dispersion | #1 | |
| Centrifugation Step 1 | 2500 rpm, 40 minutes Discard SN Redisperse SD in 30 ml DI water | |
| Centrifugation Step 2 | 1000 rpm, 40 minutes Use SN Discard SD | |
| Deposition | Vacuum filtration, PES1 | |

| Films | HI-treated | Thermally treated |
|-----------------------|---|---|
| Dispersion | #1 | |
| Centrifugation Step 1 | 1000 rpm, 40 minutes Discard SN Redisperse SD in 30 ml DI water | 4000 rpm, 60 minutes Discard SN Redisperse SD in 30 ml DI water |
| Centrifugation Step 2 | 500 rpm, 40 minutes Use SN Discard SD | - |
| Deposition | Vacuum filtration, PES1 | |
| HI treatment | Standard HI | - |
| Thermal treatment | - | Standard 3000 |
| Pressing | - | 20 μ m roll separation |

Table 6.7: Preparation protocol “Best Sixonia films”

Supplier #2:

| Films | HI-treated | Thermally treated |
|-------------------|--|------------------------|
| Dispersion | #2, dilute to 1 mgml ⁻¹ with DI water Use 30 ml per film | |
| Centrifugation | 4000 rpm, 60 minutes Discard SN Redisperse SD in 30 ml DI water | |
| Deposition | Vacuum filtration, PES2 | Vacuum filtration, MCE |
| HI treatment | Standard HI | - |
| Thermal treatment | - | Standard 3000 |
| Pressing | 20 μ m roll separation | |

Table 6.8: Preparation protocol “Best Graphenea films”

Supplier #3:

| Films | HI-treated | Thermally treated |
|-------------------|--|-------------------|
| Dispersion | #3, 30 g per film | |
| Deposition | Blade coating on copper with 2 mm slit | |
| HI treatment | Standard HI | |
| Thermal treatment | - | Standard 3000 |
| Pressing | 25 μm roll separation | |

Table 6.9: Preparation protocol “Best Gaoxitech films”

Supplier #4:

| Films | HI-treated | Thermally treated |
|-------------------|--|------------------------------------|
| Dispersion | #4, dilute to 1 mgml^{-1} with DI water and IPA (1:1) 30 ml for HI-treated, 15 ml for thermally treated | |
| Centrifugation | 4000 rpm, 60 minutes Discard SN Redisperse SD in 30 ml DI water | - |
| Deposition | Vacuum filtration, PES2 | Vacuum filtration, Anodisc |
| HI treatment | Standard HI | - |
| Thermal treatment | - | Standard 3000 |
| Pressing | - | 17.5 μm roll separation |

Table 6.10: Preparation protocol “Best Ossila films”

Supplier #5:

| Film | HI-treated |
|------------|--|
| Dispersion | #5, dilute to 1 mgml^{-1} with DI water, use 40 ml |
| Sonication | 15 minutes at 25% power |
| Deposition | Vacuum filtration, PES2 |

Table 6.11: Preparation protocol “Best Sigma-Aldrich films”

Supplier #6:

| Films | HI-treated | Thermally treated |
|-------------------|---|----------------------------------|
| Dispersion | #6, dilute to 1 mgml^{-1} with DI water Use 20 ml per film | |
| Deposition | Vacuum filtration, MCE | |
| HI treatment | Standard HI | |
| Thermal treatment | - | Standard 3000 |
| Pressing | - | 20 μm roll separation |

Table 6.12: Preparation protocol “Best TimesNano films”

6.7.2.4 Films with varying GO-portion

Films shown in Figure 4.3.4 (a) and discussed in section 4.3.2.2

| | |
|-------------------|---|
| Films | GR100, GR80, GR60, GR40, GR20, GR0 |
| Dispersions | #1 & #2 |
| Mixing ratios | 100:0, 80:20, 60:40, 40:60, 20:80, 0:100 |
| Sonication | Sonicate dispersion #2 for 20 minutes at 20% power |
| Centrifugation | Only dispersion #1: 4000 rpm, 60 minutes Discard SN, redisperse SD |
| Deposition | Vacuum filtration, Anodisc |
| Thermal treatment | Standard 3000 |
| Pressing | 20 μ m roll separation |

Table 6.13: Preparation protocol “GO-portion”

6.7.2.5 Films with and without HI-treatment before thermal annealing

Films shown in Figure 4.3.4 (b) and discussed in section 4.3.2.2

| | | |
|-------------------|--|--|
| Films | Sample pairs 1-3 | Sample pair 4 |
| Dispersion | #2, 6 x 30 ml | #1, 150 ml |
| Centrifugation | - | 4000 rpm, 60 minutes Discard SN Redisperse SD in 2 x 40 ml DI water |
| Deposition | Vacuum filtration, MCE | Vacuum filtration, PES2 |
| HI treatment | Pair successively filtrated films, Standard HI for one of each pair | Standard HI for one film |
| Thermal treatment | Standard 3000 | |
| Pressing | 20 μ m roll separation | |

Table 6.14: Preparation protocol “HI-treatment”

6.7.2.6 Film for exemplary TCR measurement

Film shown in Figure 4.3.6 (a) and discussed in section 4.3.2.3

| Film | TCR1 |
|--------------------------|---|
| Dispersion | #1, 50 ml |
| Centrifugation Step 1 | 4000 rpm, 40 minutes Discard SN Redisperse SD in 40 ml DI water |
| Centrifugation Step 2 | 500 rpm, 40 minutes Discard SN Redisperse SD in 40 ml DI water |
| Deposition | Vacuum filtration, PES1 |

Table 6.15: Preparation protocol “TCR”

6.7.2.7 Films for the comparison of experiment and simulation

Films used for the analysis of the flakesize-dependent conductivity shown in Figure 4.4.1 (a) and discussed in section 4.4

| Batch | 1 | 2 & 3 |
|--------------------------|--|--|
| Films | OR, SGR, MGR, LGR, XLGR | XSGR, SGR, MGR, LGR, XLGR |
| Dispersion | #1, OR is the original dispersion | |
| Centrifugation Step 1 | 4000 rpm, 40 minutes SN is SGR Redisperse SD in 40 ml DI water | 4000 rpm, 40 minutes SN is XSGR Redisperse SD in 40 ml DI water |
| Centrifugation Step 2 | 2500 rpm, 40 minutes SN is MGR Redisperse SD in 35 ml DI water | 3000 rpm, 40 minutes SN is SGR Redisperse SD in 35 ml DI water |
| Centrifugation Step 3 | 1000 rpm, 40 minutes SN is SGR Redisperse SD in 30 ml DI water | 2000 rpm, 40 minutes SN is MGR Redisperse SD in 35 ml DI water |
| Centrifugation Step 4 | 500 rpm, 40 minutes SN is SGR Discard SD | 1000 rpm, 40 minutes SN is LGR Redisperse SD in 30 ml DI water |
| Centrifugation Step 5 | - | 500 rpm, 40 minutes SN is XLGR Discard SD |
| Deposition | Vacuum filtration, PES1 1 film per centrifugation step in batches 1 & 3 2 films per centrifugation step in batch 2 | |

Table 6.16: Preparation protocol “Compare Simulation and Experiment”

Films used for the analysis of the GO-content-dependent conductivity shown in Figure 4.4.2 (b) and discussed in section 4.4

The homogeneous films are prepared in a similar way as explained in section 6.7.2.4 with the difference that the GO-content, the filter membranes, and the dispersion volume are varied. Furthermore, no heating is performed.

The inhomogeneous films are also prepared in a similar way as in section 6.7.2.4, but the GO dispersion #2 is not sonicated before the mixing.

Bibliography

- [1] K. S. Novoselov, A. K. Geim, S. V. Morozov, D. Jiang, Y. Zhang, S. V. Dubonos, I. V. Grigorieva, and A. A. Firsov: *Electric Field Effect in Atomically Thin Carbon Films*, Science 306 (2004), 666–669. Cited on pp. 13 and 17
- [2] A. K. Geim, and K. S. Novoselov: *The rise of graphene*, Nature Materials 6 (2007), 183–191. Cited on pp. 13, 17, and 21
- [3] R. Murali, Y. Yang, K. Brenner, T. Beck, and J. D. Meindl: *Breakdown current density of graphene nanoribbons*, Applied Physics Letters 94 (2009), 243114. Cited on p. 13
- [4] A. K. Geim: *Graphene: Status and Prospects*, Science 324 (2009), 1530–1534. Cited on pp. 13 and 18
- [5] R. Peierls: *Quelques propriétés typiques des corps solides*, Annales de l’institut Henri Poincaré 5 (1935), 177–222. Cited on p. 13
- [6] L. D. Landau: *Zur Theorie der Phasenumwandlungen II*, Phys. Z. Sowjetunion 11 (1937), 26–35. Cited on p. 13
- [7] N. D. Mermin: *Crystalline Order in Two Dimensions*, Phys. Rev. 176 (1968), 250–254. Cited on p. 13
- [8] M. Lemme: *Current Status of Graphene Transistors*, Solid State Phenomena 156-158 (2009), 499–509. Cited on p. 13
- [9] A. Nag, A. Mitra, and S. C. Mukhopadhyay: *Graphene and its sensor-based applications: A review*, Sensors and Actuators A: Physical 270 (2018), 177–194. Cited on p. 13
- [10] I. H. Son, J. H. Park, S. Park, K. Park, S. Han, J. Shin, S.-G. Doo, Y. Hwang, H. Chang, and J. W. Choi: *Graphene balls for lithium*

- rechargeable batteries with fast charging and high volumetric energy densities*, Nature Communications 8 (2017), 1561. Cited on pp. 13, 17, and 25
- [11] Patent assigned to Huawei Technologies Co Ltd, Cambridge Enterprise Ltd. Y. Xu, Y. Lin, S. Hodge, and A. C. Ferrari: *Functionalized graphene, preparation method thereof, and polyorganosiloxane* (2019), US20190233702A1. Cited on pp. 13, 17, and 28
- [12] Z. Xu, and C. Gao: *Graphene chiral liquid crystals and macroscopic assembled fibres*, Nature Communications 2 (2011), 571. Cited on pp. 13, 14, 29, and 133
- [13] Y. Liu, M. Yang, K. Pang, F. Wang, Z. Xu, W. Gao, and C. Gao: *Environmentally stable macroscopic graphene film with specific electrical conductivity exceeding metals*, Carbon 156 (2020), 205–211. Cited on pp. 14, 27, 28, 33, 109, 115, 116, and 121
- [14] R. A. Matula: *Electrical resistivity of copper, gold, palladium, and silver*, Journal of Physical and Chemical Reference Data 8 (1979), 1147–1298. Cited on pp. 14, 20, and 33
- [15] P. D. Desai, H. M. James, and C. Y. Ho: *Electrical Resistivity of Aluminum and Manganese*, Journal of Physical and Chemical Reference Data 13 (1984), 1131–1172. Cited on pp. 14 and 33
- [16] K. S. Novoselov, V. I. Fal’ko, L. Colombo, P. R. Gellert, M. G. Schwab, and K. Kim: *A roadmap for graphene*, Nature 490 (2012), 192–200. Cited on pp. 17, 21, 22, and 23
- [17] Y. Hernandez, V. Nicolosi, M. Lotya, F. M. Blighe, Z. Sun, S. De, I. T. McGovern, B. Holland, M. Byrne, Y. K. Gun’ko, J. J. Boland, P. Niraj, G. Duesberg, S. Krishnamurthy, R. Goodhue, J. Hutchison, V. Scardaci, A. C. Ferrari, and J. N. Coleman: *High-yield production of graphene by liquid-phase exfoliation of graphite*, Nature Nanotechnology 3 (2008), 563–568. Cited on pp. 17 and 22
- [18] E. P. Randviir, D. A. Brownson, and C. E. Banks: *A decade of graphene research: production, applications and outlook*, Materials Today 17 (2014), 426–432. Cited on p. 17
- [19] C. Lee, X. Wei, J. W. Kysar, and J. Hone: *Measurement of the Elastic Properties and Intrinsic Strength of Monolayer Graphene*, Science 321 (2008), 385–388. Cited on p. 18

- [20] M. I. Katsnelson, K. S. Novoselov, and A. K. Geim: *Chiral tunnelling and the Klein paradox in graphene*, Nature Physics 2 (2006), 620–625. Cited on p. 19
- [21] A. H. Castro Neto, F. Guinea, N. M. R. Peres, K. S. Novoselov, and A. K. Geim: *The electronic properties of graphene*, Reviews of Modern Physics 81 (2009), 109–162. Cited on p. 19
- [22] J.-H. Chen, C. Jang, S. Xiao, M. Ishigami, and M. S. Fuhrer: *Intrinsic and extrinsic performance limits of graphene devices on SiO₂*, Nature Nanotechnology 3 (2008), 206–209. Cited on pp. 20, 30, and 63
- [23] E. H. Hwang, and S. Das Sarma: *Acoustic phonon scattering limited carrier mobility in two-dimensional extrinsic graphene*, Physical Review B 77 (2008), 115449. Cited on pp. 20, 30, and 63
- [24] B. Partoens, and F. M. Peeters: *From graphene to graphite: Electronic structure around the K point*, Physical Review B 74 (2006), 075404. Cited on p. 20
- [25] A. Luican, G. Li, A. Reina, J. Kong, R. R. Nair, K. S. Novoselov, A. K. Geim, and E. Y. Andrei: *Single-Layer Behavior and Its Breakdown in Twisted Graphene Layers*, Physical Review Letters 106 (2011), 126802. Cited on p. 20
- [26] Y. Cao, V. Fatemi, S. Fang, K. Watanabe, T. Taniguchi, E. Kaxiras, and P. Jarillo-Herrero: *Unconventional superconductivity in magic-angle graphene superlattices*, Nature 556 (2018), 43–50. Cited on p. 20
- [27] C. J. Tabert, and E. J. Nicol: *Optical conductivity of twisted bilayer graphene*, Physical Review B 87 (2013), 121402. Cited on p. 20
- [28] X.-Y. Fang, X.-X. Yu, H.-M. Zheng, H.-B. Jin, L. Wang, and M.-S. Cao: *Temperature- and thickness-dependent electrical conductivity of few-layer graphene and graphene nanosheets*, Physics Letters A 379 (2015), 2245–2251. Cited on pp. 20, 23, and 91
- [29] P. N. Nirmalraj, T. Lutz, S. Kumar, G. S. Duesberg, and J. J. Boland: *Nanoscale Mapping of Electrical Resistivity and Connectivity in Graphene Strips and Networks*, Nano Letters 11 (2011), 16–22. Cited on pp. 20 and 92

- [30] E. Koren, I. Leven, E. Lörtscher, A. Knoll, O. Hod, and U. Duerig: *Coherent commensurate electronic states at the interface between mis-oriented graphene layers*, Nature Nanotechnology 11 (2016), 752–757. Cited on pp. 21, 66, 84, and 92
- [31] A. A. Balandin: *In-plane and cross-plane thermal conductivity of graphene: applications in thermal interface materials*, in: D. Pribat, Y.-H. Lee, and M. Razeghi (Eds.), *Carbon Nanotubes, Graphene, and Associated Devices IV*, SPIE, 2011, pp. 7 – 14. Cited on p. 21
- [32] M. Han: *Cross-plane thermal transport in graphene-based structures*, PhD thesis, Iowa State University, 2018. Cited on p. 21
- [33] L. Banszerus, M. Schmitz, S. Engels, J. Dauber, M. Oellers, F. Haupt, K. Watanabe, T. Taniguchi, B. Beschoten, and C. Stampfer: *Ultrahigh-mobility graphene devices from chemical vapor deposition on reusable copper*, Science Advances 1 (2015), e1500222. Cited on p. 22
- [34] Y. Zhu, Z. Sun, Z. Yan, Z. Jin, and J. M. Tour: *Rational Design of Hybrid Graphene Films for High-Performance Transparent Electrodes*, ACS Nano 5 (2011), 6472–6479. Cited on p. 22
- [35] M. Segal: *Selling graphene by the ton*, Nature Nanotechnology 4 (2009), 612–614. Cited on p. 22
- [36] Y. Xu, H. Cao, Y. Xue, B. Li, and W. Cai: *Liquid-Phase Exfoliation of Graphene: An Overview on Exfoliation Media, Techniques, and Challenges*, Nanomaterials 8 (2018), 942. Cited on p. 22
- [37] K. R. Paton, E. Varrla, C. Backes, R. J. Smith, U. Khan, A. O’Neill, C. Boland, M. Lotya, O. M. Istrate, P. King, T. Higgins, S. Barwich, P. May, P. Puczkarski, I. Ahmed, M. Moebius, H. Pettersson, E. Long, J. Coelho, S. E. O’Brien, E. K. McGuire, B. M. Sanchez, G. S. Duesberg, N. McEvoy, T. J. Pennycook, C. Downing, A. Crossley, V. Nicolosi, and J. N. Coleman: *Scalable production of large quantities of defect-free few-layer graphene by shear exfoliation in liquids*, Nature Materials 13 (2014), 624–630. Cited on p. 22
- [38] S. Yang, M. R. Lohe, K. Müllen, and X. Feng: *New-Generation Graphene from Electrochemical Approaches: Production and Applications*, Advanced Materials 28 (2016), 6213–6221. Cited on p. 22

- [39] W. Wu, M. Liu, Y. Gu, B. Guo, H. Ma, P. Wang, X. Wang, and R. Zhang: *Fast chemical exfoliation of graphite to few-layer graphene with high quality and large size via a two-step microwave-assisted process*, Chemical Engineering Journal 381 (2020), 122592. Cited on pp. 22 and 133
- [40] Z. Xu, and C. Gao: *Aqueous Liquid Crystals of Graphene Oxide*, ACS Nano 5 (2011), 2908–2915. Cited on p. 22
- [41] Y. Liu, Z. Xu, W. Gao, Z. Cheng, and C. Gao: *Graphene and Other 2D Colloids: Liquid Crystals and Macroscopic Fibers*, Advanced Materials 29 (2017), 1606794. Cited on pp. 22, 29, and 30
- [42] Y. Zhu, H. Ji, H.-M. Cheng, and R. S. Ruoff: *Mass production and industrial applications of graphene materials*, National Science Review 5 (2018), 90–101. Cited on p. 23
- [43] US Geological Survey, 2019, *Mineral Commodity Summaries 2019*, 73. Cited on p. 23
- [44] W. Primak: *C -Axis Electrical Conductivity of Graphite*, Physical Review 103 (1956), 544–546. Cited on p. 23
- [45] L. C. F. Blackman, and A. R. Ubbelohde: *Stress recrystallization of graphite*, Proceedings of the Royal Society of London. Series A. Mathematical and Physical Sciences 266 (1962), 20–32. Cited on p. 24
- [46] M. S. Dresselhaus, and G. Dresselhaus: *Intercalation compounds of graphite*, Advances in Physics 51 (2002), 1–186. Cited on pp. 24, 26, 27, 32, 81, 94, and 95
- [47] D. E. Tsentalovich, R. J. Headrick, F. Mirri, J. Hao, N. Behabtu, C. C. Young, and M. Pasquali: *Influence of Carbon Nanotube Characteristics on Macroscopic Fiber Properties*, ACS Applied Materials & Interfaces 9 (2017), 36189–36198. Cited on pp. 24 and 25
- [48] G. Chen, D. N. Futaba, S. Sakurai, M. Yumura, and K. Hata: *Interplay of wall number and diameter on the electrical conductivity of carbon nanotube thin films*, Carbon 67 (2014), 318–325. Cited on p. 24
- [49] S. Ilani, and P. L. McEuen: *Electron Transport in Carbon Nanotubes*, Annual Review of Condensed Matter Physics 1 (2010), 1–25. Cited on p. 24

- [50] S. Iijima: *Helical microtubules of graphitic carbon*, Nature 354 (1991), 56–58. Cited on p. 25
- [51] T. W. Ebbesen, and P. M. Ajayan: *Large-scale synthesis of carbon nanotubes*, Nature 358 (1992), 220–222. Cited on p. 25
- [52] T. Guo, P. Nikolaev, A. Thess, D. Colbert, and R. Smalley: *Catalytic growth of single-walled nanotubes by laser vaporization*, Chemical Physics Letters 243 (1995), 49–54. Cited on p. 25
- [53] S. M. Jafarpour, M. Kini, S. E. Schulz, and S. Hermann: *Effects of catalyst configurations and process conditions on the formation of catalyst nanoparticles and growth of single-walled carbon nanotubes*, Microelectronic Engineering 167 (2017), 95–104. Cited on p. 25
- [54] S. M. Jafarpour, S. E. Schulz, and S. Hermann: *Tuning of diameter and electronic type of CCVD grown SWCNTs: A comparative study on Co-Mo and Co-Ru bimetallic catalyst systems*, Diamond and Related Materials 89 (2018), 18–27. Cited on p. 25
- [55] G. Rahman, Z. Najaf, A. Mehmood, S. Bilal, A. Shah, S. Mian, and G. Ali: *An Overview of the Recent Progress in the Synthesis and Applications of Carbon Nanotubes*, C 5 (2019), 3. Cited on p. 25
- [56] A. Venkataraman, E. V. Amadi, Y. Chen, and C. Papadopoulos: *Carbon Nanotube Assembly and Integration for Applications*, Nanoscale Research Letters 14 (2019), 220. Cited on p. 25
- [57] H. Zhang, L. Xiang, Y. Yang, M. Xiao, J. Han, L. Ding, Z. Zhang, Y. Hu, and L.-M. Peng: *High-Performance Carbon Nanotube Complementary Electronics and Integrated Sensor Systems on Ultrathin Plastic Foil*, ACS Nano 12 (2018), 2773–2779. Cited on p. 25
- [58] C. Wagner, T. Blaudeck, P. Meszmer, S. Böttger, F. Fuchs, S. Hermann, J. Schuster, B. Wunderle, and S. E. Schulz: *Carbon Nanotubes for Mechanical Sensor Applications*, physica status solidi (a) 216 (2019), 1900584. Cited on p. 25
- [59] W. G. Reis, R. T. Weitz, M. Kettner, A. Kraus, M. G. Schwab, e. Tomović, R. Krupke, and J. Mikhael: *Highly Efficient and Scalable Separation of Semiconducting Carbon Nanotubes via Weak Field Centrifugation*, Scientific Reports 6 (2016), 26259. Cited on p. 25

- [60] H. Sun, Z. Xu, and C. Gao: *Multifunctional, Ultra-Flyweight, Synergistically Assembled Carbon Aerogels*, *Advanced Materials* 25 (2013), 2554–2560. Cited on p. 25
- [61] G. Foley, C. Zeller, E. Falardeau, and F. Vogel: *Room temperature electrical conductivity of a highly two dimensional synthetic metal: AsF₅-graphite*, *Solid State Communications* 24 (1977), 371–375. Cited on p. 26
- [62] F. L. Vogel: *The electrical conductivity of graphite intercalated with superacid fluorides: experiments with antimony pentafluoride*, *Journal of Materials Science* 12 (1977), 982–986. Cited on p. 26
- [63] J. Shioya, H. Matsubara, and S. Murakami: *Properties of AsF₅-intercalated vapor-grown graphite*, *Synthetic Metals* 14 (1986), 113–123. Cited on pp. 26, 33, and 95
- [64] E. R. Falardeau, G. M. T. Foley, C. Zeller, and F. L. Vogel: *Very high electrical conductivity in AsF₅-graphite intercalation compounds*, *J. Chem. Soc., Chem. Commun.* (1977), 389–390. Cited on p. 26
- [65] E. Zhou, J. Xi, Y. Liu, Z. Xu, Y. Guo, L. Peng, W. Gao, J. Ying, Z. Chen, and C. Gao: *Large-area potassium-doped highly conductive graphene films for electromagnetic interference shielding*, *Nanoscale* 9 (2017), 18613–18618. Cited on pp. 27, 28, 29, 32, 36, 81, 95, 104, 107, 113, 121, and 122
- [66] D. A. Dikin, S. Stankovich, E. J. Zimney, R. D. Piner, G. H. B. Dommett, G. Evmenenko, S. T. Nguyen, and R. S. Ruoff: *Preparation and characterization of graphene oxide paper*, *Nature* 448 (2007), 457–460. Cited on p. 27
- [67] G. Eda, G. Fanchini, and M. Chhowalla: *Large-area ultrathin films of reduced graphene oxide as a transparent and flexible electronic material*, *Nature Nanotechnology* 3 (2008), 270–274. Cited on pp. 27, 28, and 107
- [68] H. A. Becerril, J. Mao, Z. Liu, R. M. Stoltenberg, Z. Bao, and Y. Chen: *Evaluation of Solution-Processed Reduced Graphene Oxide Films as Transparent Conductors*, *ACS Nano* 2 (2008), 463–470. Cited on p. 27
- [69] H. Chen, M. B. Müller, K. J. Gilmore, G. G. Wallace, and D. Li: *Mechanically Strong, Electrically Conductive, and Biocompatible Graphene Paper*, *Advanced Materials* 20 (2008), 3557–3561. Cited on p. 27

- [70] D. Li, M. B. Müller, S. Gilje, R. B. Kaner, and G. G. Wallace: *Processable aqueous dispersions of graphene nanosheets*, Nature Nanotechnology 3 (2008), 101–105. Cited on p. 27
- [71] N. Wang, M. K. Samani, H. Li, L. Dong, Z. Zhang, P. Su, S. Chen, J. Chen, S. Huang, G. Yuan, X. Xu, B. Li, K. Leifer, L. Ye, and J. Liu: *Tailoring the Thermal and Mechanical Properties of Graphene Film by Structural Engineering*, Small 14 (2018), 1801346. Cited on pp. 27, 28, 115, and 116
- [72] S. Lin, S. Ju, J. Zhang, G. Shi, Y. He, and D. Jiang: *Ultrathin flexible graphene films with high thermal conductivity and excellent EMI shielding performance using large-sized graphene oxide flakes*, RSC Advances 9 (2019), 1419–1427. Cited on pp. 27, 29, 41, 82, 83, 95, 102, and 104
- [73] L. Peng, Z. Xu, Z. Liu, Y. Guo, P. Li, and C. Gao: *Ultrahigh Thermal Conductive yet Superflexible Graphene Films*, Advanced Materials 29 (2017), 1700589. Cited on pp. 27, 28, 33, 46, 81, 95, 109, 110, 115, 116, and 122
- [74] A. Celzard, S. Schneider, and J. Maréché: *Densification of expanded graphite*, Carbon 40 (2002), 2185–2191. Cited on p. 28
- [75] X. Chen, X. Deng, N. Y. Kim, Y. Wang, Y. Huang, L. Peng, M. Huang, X. Zhang, X. Chen, D. Luo, B. Wang, X. Wu, Y. Ma, Z. Lee, and R. S. Ruoff: *Graphitization of graphene oxide films under pressure*, Carbon 132 (2018), 294–303. Cited on pp. 28 and 116
- [76] W. Kong, H. Kum, S.-H. Bae, J. Shim, H. Kim, L. Kong, Y. Meng, K. Wang, C. Kim, and J. Kim: *Path towards graphene commercialization from lab to market*, Nature Nanotechnology 14 (2019), 927–938. Cited on p. 28
- [77] B. Zhang, J. Zhang, C. Liu, Z. Wu, and D. He: *Equivalent Resonant Circuit Modeling of a Graphene-Based Bowtie Antenna*, Electronics 7 (2018), 285. Cited on pp. 28 and 133
- [78] R. Song, Q. Wang, B. Mao, Z. Wang, D. Tang, B. Zhang, J. Zhang, C. Liu, D. He, Z. Wu, and S. Mu: *Flexible graphite films with high conductivity for radio-frequency antennas*, Carbon 130 (2018), 164–169. Cited on pp. 28 and 133
- [79] W. Zhou, C. Liu, R. Song, X. Zeng, B.-W. Li, W. Xia, J. Zhang, G.-L. Huang, Z. P. Wu, and D. He: *Flexible radiofrequency filters based on*

highly conductive graphene assembly films, Applied Physics Letters 114 (2019), 113503. Cited on pp. 28, 122, and 133

- [80] Y.-J. Wan, P.-L. Zhu, S.-H. Yu, R. Sun, C.-P. Wong, and W.-H. Liao: *Graphene paper for exceptional EMI shielding performance using large-sized graphene oxide sheets and doping strategy*, Carbon 122 (2017), 74–81. Cited on pp. 28, 41, 82, 83, and 102
- [81] G. Eda, Y.-Y. Lin, S. Miller, C.-W. Chen, W.-F. Su, and M. Chhowalla: *Transparent and conducting electrodes for organic electronics from reduced graphene oxide*, Applied Physics Letters 92 (2008), 233305. Cited on p. 28
- [82] D. S. Hecht, L. Hu, and G. Irvin: *Emerging Transparent Electrodes Based on Thin Films of Carbon Nanotubes, Graphene, and Metallic Nanostructures*, Advanced Materials 23 (2011), 1482–1513. Cited on p. 28
- [83] G. Xin, H. Sun, T. Hu, H. R. Fard, X. Sun, N. Koratkar, T. Borca-Tasciuc, and J. Lian: *Large-Area Freestanding Graphene Paper for Superior Thermal Management*, Advanced Materials 26 (2014), 4521–4526. Cited on pp. 28, 95, 109, and 113
- [84] Z. Wang, B. Mao, Q. Wang, J. Yu, J. Dai, R. Song, Z. Pu, D. He, Z. Wu, and S. Mu: *Ultrahigh Conductive Copper/Large Flake Size Graphene Heterostructure Thin-Film with Remarkable Electromagnetic Interference Shielding Effectiveness*, Small 14 (2018), 1704332. Cited on pp. 28, 95, and 113
- [85] J.-X. Yan, Y.-C. Leng, Y.-N. Guo, G.-Q. Wang, H. Gong, P.-Z. Guo, P.-H. Tan, Y.-Z. Long, X.-L. Liu, and W.-P. Han: *Highly Conductive Graphene Paper with Vertically Aligned Reduced Graphene Oxide Sheets Fabricated by Improved Electrospray Deposition Technique*, ACS Applied Materials & Interfaces 11 (2019), 10810–10817. Cited on pp. 28 and 113
- [86] R. A. Nistor, D. M. Newns, and G. J. Martyna: *The Role of Chemistry in Graphene Doping for Carbon-Based Electronics*, ACS Nano 5 (2011), 3096–3103. Cited on p. 28
- [87] Q. Tang, Z. Zhou, and Z. Chen: *Graphene-related nanomaterials: tuning properties by functionalization*, Nanoscale 5 (2013), 4541. Cited on p. 28
- [88] Y. Gotoh, K. Tamada, N. Akuzawa, M. Fujishige, K. Takeuchi, M. Endo, R. Matsumoto, Y. Soneda, and T. Takeichi: *Preparation of air-stable*

and highly conductive potassium-intercalated graphite sheet, *Journal of Physics and Chemistry of Solids* 74 (2013), 1482–1486. Cited on p. 28

- [89] J. J. Murray, and A. R. Ubbelohde: *Electronic Properties of Some Synthetic Metals Derived from Graphite*, *Proceedings of the Royal Society A: Mathematical, Physical and Engineering Sciences* 312 (1969), 371–380. Cited on pp. 28 and 81
- [90] A. Rinzler, J. Liu, H. Dai, P. Nikolaev, C. Huffman, F. Rodríguez-Macías, P. Boul, A. Lu, D. Heymann, D. Colbert, R. Lee, J. Fischer, A. Rao, P. Eklund, and R. Smalley: *Large-scale purification of single-wall carbon nanotubes: process, product, and characterization*, *Applied Physics A: Materials Science & Processing* 67 (1998), 29–37. Cited on p. 29
- [91] Z. Xu, and C. Gao: *Graphene fiber: a new trend in carbon fibers*, *Materials Today* 18 (2015), 480–492. Cited on pp. 29, 30, and 32
- [92] Z. Xu, Y. Liu, X. Zhao, L. Peng, H. Sun, Y. Xu, X. Ren, C. Jin, P. Xu, M. Wang, and C. Gao: *Ultrastiff and Strong Graphene Fibers via Full-Scale Synergetic Defect Engineering*, *Advanced Materials* 28 (2016), 6449–6456. Cited on pp. 29, 30, and 109
- [93] H. Cheng, C. Hu, Y. Zhao, and L. Qu: *Graphene fiber: a new material platform for unique applications*, *NPG Asia Materials* 6 (2014), e113–e113. Cited on p. 29
- [94] G. Xin, T. Yao, H. Sun, S. M. Scott, D. Shao, G. Wang, and J. Lian: *Highly thermally conductive and mechanically strong graphene fibers*, *Science* 349 (2015), 1083–1087. Cited on pp. 29, 30, 109, 121, and 126
- [95] I. H. Kim, T. Yun, J.-E. Kim, H. Yu, S. P. Sasikala, K. E. Lee, S. H. Koo, H. Hwang, H. J. Jung, J. Y. Park, H. S. Jeong, and S. O. Kim: *Mussel-Inspired Defect Engineering of Graphene Liquid Crystalline Fibers for Synergistic Enhancement of Mechanical Strength and Electrical Conductivity*, *Advanced Materials* 30 (2018), 1803267. Cited on p. 29
- [96] N. Uçar, M. Ölmez, B. K. Kayaoğlu, A. Önen, N. Karatepe Yavuz, and O. Eksik: *Structural properties of graphene oxide fibers: from graphene oxide dispersion until continuous graphene oxide fiber*, *The Journal of The Textile Institute* 109 (2018), 1642–1652. Cited on p. 29

- [97] Z. Xu, L. Peng, Y. Liu, Z. Liu, H. Sun, W. Gao, and C. Gao: *Experimental Guidance to Graphene Macroscopic Wet-Spun Fibers, Continuous Papers, and Ultralightweight Aerogels*, Chemistry of Materials 29 (2017), 319–330. Cited on p. 30
- [98] G. Xin, W. Zhu, Y. Deng, J. Cheng, L. T. Zhang, A. J. Chung, S. De, and J. Lian: *Microfluidics-enabled orientation and microstructure control of macroscopic graphene fibres*, Nature Nanotechnology 14 (2019), 168–175. Cited on pp. 30, 33, 47, 94, and 95
- [99] C. Xiang, C. C. Young, X. Wang, Z. Yan, C.-C. Hwang, G. Ceriotti, J. Lin, J. Kono, M. Pasquali, and J. M. Tour: *Large Flake Graphene Oxide Fibers with Unconventional 100% Knot Efficiency and Highly Aligned Small Flake Graphene Oxide Fibers*, Advanced Materials 25 (2013), 4592–4597. Cited on p. 30
- [100] Y. Liu, Z. Xu, J. Zhan, P. Li, and C. Gao: *Superb Electrically Conductive Graphene Fibers via Doping Strategy*, Advanced Materials 28 (2016), 7941–7947. Cited on pp. 30, 31, 32, 33, 36, 95, and 121
- [101] Z. Xu, Z. Liu, H. Sun, and C. Gao: *Highly Electrically Conductive Ag-Doped Graphene Fibers as Stretchable Conductors*, Advanced Materials 25 (2013), 3249–3253. Cited on p. 30
- [102] B. Fang, J. Xi, Y. Liu, F. Guo, Z. Xu, W. Gao, D. Guo, P. Li, and C. Gao: *Wrinkle-stabilized metal-graphene hybrid fibers with zero temperature coefficient of resistance*, Nanoscale 9 (2017), 12178–12188. Cited on pp. 30, 31, and 33
- [103] Y. Liu, H. Liang, Z. Xu, J. Xi, G. Chen, W. Gao, M. Xue, and C. Gao: *Superconducting Continuous Graphene Fibers via Calcium Intercalation*, ACS Nano 11 (2017), 4301–4306. Cited on p. 31
- [104] B. Ozipek, and H. Karakas: *Wet spinning of synthetic polymer fibers in Advances in Filament Yarn Spinning of Textiles and Polymers*, 2014, 174–186, Woodhead Publishing. Cited on p. 31
- [105] B. Vigolo: *Macroscopic Fibers and Ribbons of Oriented Carbon Nanotubes*, Science 290 (2000), 1331–1334. Cited on p. 31
- [106] Y.-L. Li: *Direct Spinning of Carbon Nanotube Fibers from Chemical Vapor Deposition Synthesis*, Science 304 (2004), 276–278. Cited on p. 31

- [107] Y. Zhao, J. Wei, R. Vajtai, P. M. Ajayan, and E. V. Barrera: *Iodine doped carbon nanotube cables exceeding specific electrical conductivity of metals*, Scientific Reports 1 (2011), 83. Cited on pp. 31 and 33
- [108] F. Smail, A. Boies, and A. Windle: *Direct spinning of CNT fibres: Past, present and future scale up*, Carbon 152 (2019), 218–232. Cited on p. 31
- [109] B. Predel: *Ac-Ag ... Au-Zr* 2006, Springer-Verlag. Cited on pp. 31 and 33
- [110] H. Vogler: *Glühlampen und Chemiefasern: Zum 100. Todestag von Joseph Wilson Swan*, Chemie in unserer Zeit 48 (2014), 309–311. Cited on p. 31
- [111] H. G. Chae, B. A. Newcomb, P. V. Gulgunje, Y. Liu, K. K. Gupta, M. G. Kamath, K. M. Lyons, S. Ghoshal, C. Pramanik, L. Giannuzzi, K. Şahin, I. Chasiotis, and S. Kumar: *High strength and high modulus carbon fibers*, Carbon 93 (2015), 81–87. Cited on p. 32
- [112] A. Dümke, K. Lampe, W. Machon, and W. Friedrich: *Friedrich Tabellenbuch Elektrotechnik/Elektronik* 2017, Westermann. Cited on p. 33
- [113] L. Rizzi, A. Zienert, J. Schuster, M. Köhne, and S. E. Schulz: *Electrical Conductivity Modeling of Graphene-based Conductor Materials*, ACS Applied Materials & Interfaces 10 (2018), 43088–43094. Cited on pp. 35, 37, 63, 75, 78, and 138
- [114] L. Rizzi, A. Zienert, J. Schuster, M. Köhne, and S. E. Schulz: *Computationally efficient simulation method for conductivity modeling of 2D-based conductors*, Computational Materials Science 161 (2019), 364–370. Cited on pp. 35, 45, 46, 55, 63, 65, 66, 69, 70, 71, 135, 136, and 137
- [115] I. Lifshitz: *Self-Averaging* 2011, Crypt Publishing. Cited on p. 37
- [116] X. Lin, X. Shen, Q. Zheng, N. Yousefi, L. Ye, Y.-W. Mai, and J.-K. Kim: *Fabrication of Highly-Aligned, Conductive, and Strong Graphene Papers Using Ultralarge Graphene Oxide Sheets*, ACS Nano 6 (2012), 10708–10719. Cited on pp. 41, 82, 83, 102, and 103
- [117] J. Chen, Y. Li, L. Huang, N. Jia, C. Li, and G. Shi: *Size Fractionation of Graphene Oxide Sheets via Filtration through Track-Etched Membranes*, Advanced Materials 27 (2015), 3654–3660. Cited on pp. 41, 82, 83, 102, 107, and 113

- [118] J. N. Reddy: *An introduction to the finite element method* 2005, 3rd ed., McGraw-Hill. Cited on p. 44
- [119] M. Jung, and U. Langer: *Methode der finiten Elemente für Ingenieure* 2013, Springer Fachmedien Wiesbaden. Cited on p. 44
- [120] X. Qi, T. Zhou, S. Deng, G. Zong, X. Yao, and Q. Fu: *Size-specified graphene oxide sheets: ultrasonication assisted preparation and characterization*, Journal of Materials Science 49 (2014), 1785–1793. Cited on pp. 46, 95, and 101
- [121] J. E. Guyer, D. Wheeler, and J. A. Warren: *FiPy: Partial Differential Equations with Python*, Computing in Science & Engineering 11 (2009), 6–15. Cited on p. 57
- [122] D. A. G. Bruggeman: *Berechnung verschiedener physikalischer Konstanten von heterogenen Substanzen. I. Dielektrizitätskonstanten und Leitfähigkeiten der Mischkörper aus isotropen Substanzen*, Annalen der Physik 416 (1935), 636–664. Cited on p. 63
- [123] D. S. McLachlan, M. Blaszkiewicz, and R. E. Newnham: *Electrical Resistivity of Composites*, Journal of the American Ceramic Society 73 (1990), 2187–2203. Cited on pp. 63, 78, 79, and 130
- [124] J. Helsing, and A. Helte: *Effective conductivity of aggregates of anisotropic grains*, Journal of Applied Physics 69 (1991), 3583–3588. Cited on p. 63
- [125] K. Jagannadham: *Electrical conductivity of copper-graphene composite films synthesized by electrochemical deposition with exfoliated graphene platelets*, Journal of Vacuum Science & Technology B, Nanotechnology and Microelectronics: Materials, Processing, Measurement, and Phenomena 30 (2012), 03D109. Cited on p. 63
- [126] K. Jagannadham: *Volume Fraction of Graphene Platelets in Copper-Graphene Composites*, Metallurgical and Materials Transactions A 44 (2013), 552–559. Cited on p. 63
- [127] S. Kirkpatrick: *Percolation and Conduction*, Reviews of Modern Physics 45 (1973), 574–588. Cited on p. 63
- [128] J. Bernasconi: *Conduction in anisotropic disordered systems: Effective-medium theory*, Physical Review B 9 (1974), 4575–4579. Cited on p. 63

- [129] C. O’Callaghan, C. Gomes da Rocha, H. G. Manning, J. J. Boland, and M. S. Ferreira: *Effective medium theory for the conductivity of disordered metallic nanowire networks*, Physical Chemistry Chemical Physics 18 (2016), 27564–27571. Cited on pp. 64 and 66
- [130] A. V. Melnikov, M. Shuba, and P. Lambin: *Modeling the electrical properties of three-dimensional printed meshes with the theory of resistor lattices*, Physical Review E 97 (2018), 043307. Cited on p. 64
- [131] F. Liu, C. Wang, and Q. Tang: *Conductivity Maximum in 3D Graphene Foams*, Small 14 (2018), 1801458. Cited on p. 64
- [132] H. O. Pierson: *Handbook of carbon, graphite, diamond, and fullerenes: properties, processing, and applications* 1993, Noyes Publications. Cited on p. 65
- [133] V. Perebeinos, J. Tersoff, and P. Avouris: *Phonon-Mediated Interlayer Conductance in Twisted Graphene Bilayers*, Physical Review Letters 109 (2012), 236604. Cited on pp. 66, 84, and 92
- [134] F. Dalmas, R. Dendievel, L. Chazeau, J.-Y. Cavaillé, and C. Gauthier: *Carbon nanotube-filled polymer composites. Numerical simulation of electrical conductivity in three-dimensional entangled fibrous networks*, Acta Materialia 54 (2006), 2923–2931. Cited on p. 66
- [135] L. Dalcín, R. Paz, and M. Storti: *MPI for Python*, Journal of Parallel and Distributed Computing 65 (2005), 1108–1115. Cited on p. 73
- [136] H.-B. Zhang, W.-G. Zheng, Q. Yan, Y. Yang, J.-W. Wang, Z.-H. Lu, G.-Y. Ji, and Z.-Z. Yu: *Electrically conductive polyethylene terephthalate/graphene nanocomposites prepared by melt compounding*, Polymer 51 (2010), 1191–1196. Cited on p. 79
- [137] E. Tkalya, M. Ghislandi, R. Otten, M. Lotya, A. Alekseev, P. van der Schoot, J. Coleman, G. de With, and C. Koning: *Experimental and Theoretical Study of the Influence of the State of Dispersion of Graphene on the Percolation Threshold of Conductive Graphene/Polystyrene Nanocomposites*, ACS Applied Materials & Interfaces 6 (2014), 15113–15121. Cited on p. 79
- [138] H. Pang, T. Chen, G. Zhang, B. Zeng, and Z.-M. Li: *An electrically conducting polymer/graphene composite with a very low percolation threshold*, Materials Letters 64 (2010), 2226–2229. Cited on p. 79

- [139] I. Miccoli, F. Edler, H. Pfnür, and C. Tegenkamp: *The 100th anniversary of the four-point probe technique: the role of probe geometries in isotropic and anisotropic systems*, Journal of Physics: Condensed Matter 27 (2015), 223201. Cited on pp. 85, 88, 118, 141, and 142
- [140] I. Shiraki, F. Tanabe, R. Hobara, T. Nagao, and S. Hasegawa: *Independently driven four-tip probes for conductivity measurements in ultrahigh vacuum*, Surface Science 493 (2001), 633–643. Cited on p. 88
- [141] L. Valdes: *Resistivity Measurements on Germanium for Transistors*, Proceedings of the IRE 42 (1954), 420–427. Cited on p. 90
- [142] F. M. Smits: *Measurement of Sheet Resistivities with the Four-Point Probe*, Bell System Technical Journal 37 (1958), 711–718. Cited on p. 90
- [143] E. J. Zimney, G. H. B. Dommett, R. S. Ruoff, and D. A. Dikin: *Correction factors for 4-probe electrical measurements with finite size electrodes and material anisotropy: a finite element study*, Measurement Science and Technology 18 (2007), 2067–2073. Cited on p. 90
- [144] U. Khan, A. O’Neill, H. Porwal, P. May, K. Nawaz, and J. N. Coleman: *Size selection of dispersed, exfoliated graphene flakes by controlled centrifugation*, Carbon 50 (2011), 470–475. Cited on pp. 91 and 101
- [145] M. Lotya, A. Rakovich, J. F. Donegan, and J. N. Coleman: *Measuring the lateral size of liquid-exfoliated nanosheets with dynamic light scattering*, Nanotechnology 24 (2013), 265703. Cited on pp. 91, 102, and 126
- [146] T. Thompson, E. McCarron, and N. Bartlett: *The electrical conductivity of graphite-AsF₅ intercalation compounds and their relationship to other graphite-MF₆ salts*, Synthetic Metals 3 (1980), 255–267. Cited on p. 95
- [147] A. Govorov, D. Wentzel, S. Miller, A. Kanaan, and I. Sevostianov: *Electrical conductivity of epoxy-graphene and epoxy-carbon nanofibers composites subjected to compressive loading*, International Journal of Engineering Science 123 (2018), 174–180. Cited on p. 96
- [148] A. J. Marsden, D. G. Papageorgiou, C. Vallés, A. Liscio, V. Palermo, M. A. Bissett, R. J. Young, and I. A. Kinloch: *Electrical percolation in graphene-polymer composites*, 2D Materials 5 (2018), 032003. Cited on p. 96

- [149] J.-J. Huang, and Y. J. Yuan: *A sedimentation study of graphene oxide in aqueous solution using gradient differential centrifugation*, Physical Chemistry Chemical Physics 18 (2016), 12312–12322. Cited on p. 101
- [150] S. P. Ogilvie, M. J. Large, M. A. O’Mara, P. J. Lynch, C. L. Lee, A. A. K. King, C. Backes, and A. B. Dalton: *Size selection of liquid-exfoliated 2D nanosheets*, 2D Materials 6 (2019), 031002. Cited on p. 101
- [151] G. G. Stokes: *On the effect of internal friction of fluids on the motion of pendulums*, Mathematical and Physical Papers 3 (1851), 8–106. Cited on p. 101
- [152] C. Backes, B. M. Szydłowska, A. Harvey, S. Yuan, V. Vega-Mayoral, B. R. Davies, P.-l. Zhao, D. Hanlon, E. J. G. Santos, M. I. Katsnelson, W. J. Blau, C. Gadermaier, and J. N. Coleman: *Production of Highly Monolayer Enriched Dispersions of Liquid-Exfoliated Nanosheets by Liquid Cascade Centrifugation*, ACS Nano 10 (2016), 1589–1601. Cited on p. 101
- [153] C. Backes, D. Hanlon, B. M. Szydłowska, A. Harvey, R. J. Smith, T. M. Higgins, and J. N. Coleman: *Preparation of Liquid-exfoliated Transition Metal Dichalcogenide Nanosheets with Controlled Size and Thickness: A State of the Art Protocol*, Journal of Visualized Experiments 118 (2016), e54806. Cited on p. 101
- [154] S. Fujime, and K. Kubota: *Dynamic light scattering from dilute suspensions of thin discs and thin rods as limiting forms of cylinder, ellipsoid and ellipsoidal shell of revolution*, Biophysical Chemistry 23 (1985), 1–13. Cited on p. 102
- [155] F. Babick: *Characterisation of Colloidal Suspensions in Suspensions of Colloidal Particles and Aggregates*, 2016, 7–74, Springer International Publishing. Cited on p. 102
- [156] R. D. Deegan, O. Bakajin, T. F. Dupont, G. Huber, S. R. Nagel, and T. A. Witten: *Capillary flow as the cause of ring stains from dried liquid drops*, Nature 389 (1997), 827–829. Cited on p. 102
- [157] C. Teng, D. Xie, J. Wang, Z. Yang, G. Ren, and Y. Zhu: *Ultrahigh Conductive Graphene Paper Based on Ball-Milling Exfoliated Graphene*, Advanced Functional Materials 27 (2017), 1700240. Cited on p. 104

- [158] B. Shen, W. Zhai, and W. Zheng: *Ultrathin Flexible Graphene Film: An Excellent Thermal Conducting Material with Efficient EMI Shielding*, Advanced Functional Materials 24 (2014), 4542–4548. Cited on pp. 105 and 116
- [159] K. W. Putz, O. C. Compton, C. Segar, Z. An, S. T. Nguyen, and L. C. Brinson: *Evolution of Order During Vacuum-Assisted Self-Assembly of Graphene Oxide Paper and Associated Polymer Nanocomposites*, ACS Nano 5 (2011), 6601–6609. Cited on p. 106
- [160] S. Stankovich, D. A. Dikin, R. D. Piner, K. A. Kohlhaas, A. Kleinhammes, Y. Jia, Y. Wu, S. T. Nguyen, and R. S. Ruoff: *Synthesis of graphene-based nanosheets via chemical reduction of exfoliated graphite oxide*, Carbon 45 (2007), 1558–1565. Cited on p. 107
- [161] V. C. Tung, M. J. Allen, Y. Yang, and R. B. Kaner: *High-throughput solution processing of large-scale graphene*, Nature Nanotechnology 4 (2009), 25–29. Cited on p. 107
- [162] S. Pei, J. Zhao, J. Du, W. Ren, and H.-M. Cheng: *Direct reduction of graphene oxide films into highly conductive and flexible graphene films by hydrohalic acids*, Carbon 48 (2010), 4466–4474. Cited on pp. 107 and 109
- [163] Y. Wen, M. Wu, M. Zhang, C. Li, and G. Shi: *Topological Design of Ultrastrong and Highly Conductive Graphene Films*, Advanced Materials 29 (2017), 1702831. Cited on p. 107
- [164] S. Wan, Y. Chen, Y. Wang, G. Li, G. Wang, L. Liu, J. Zhang, Y. Liu, Z. Xu, A. P. Tomsia, L. Jiang, and Q. Cheng: *Ultrastrong Graphene Films via Long-Chain Pi-Bridging*, Matter 1 (2019), 389–401. Cited on pp. 107, 113, and 133
- [165] J. Zhu, and D. Shi: *A possible self-healing mechanism in damaged graphene by heat treatment*, Computational Materials Science 68 (2013), 391–395. Cited on p. 109
- [166] L. Song, F. Khoerunnisa, W. Gao, W. Dou, T. Hayashi, K. Kaneko, M. Endo, and P. M. Ajayan: *Effect of high-temperature thermal treatment on the structure and adsorption properties of reduced graphene oxide*, Carbon 52 (2013), 608–612. Cited on pp. 109, 110, and 115
- [167] N.-J. Song, C.-X. Lu, C.-M. Chen, C.-L. Ma, and Q.-Q. Kong: *Effect of annealing temperature on the mechanical properties of flexible graphene*

- films*, New Carbon Materials 32 (2017), 221–226. Cited on pp. 109 and 115
- [168] C. Botas, P. Álvarez, C. Blanco, R. Santamaría, M. Granda, M. D. Gutiérrez, F. Rodríguez-Reinoso, and R. Menéndez: *Critical temperatures in the synthesis of graphene-like materials by thermal exfoliation–reduction of graphite oxide*, Carbon 52 (2013), 476–485. Cited on pp. 109 and 110
- [169] H. Wu, and L. T. Drzal: *Graphene nanoplatelet paper as a light-weight composite with excellent electrical and thermal conductivity and good gas barrier properties*, Carbon 50 (2012), 1135–1145. Cited on p. 113
- [170] A. C. Ferrari, J. C. Meyer, V. Scardaci, C. Casiraghi, M. Lazzeri, F. Mauri, S. Piscanec, D. Jiang, K. S. Novoselov, S. Roth, and A. K. Geim: *Raman Spectrum of Graphene and Graphene Layers*, Physical Review Letters 97 (2006), 187401. Cited on p. 114
- [171] P. Poncharal, A. Ayari, T. Michel, and J.-L. Sauvajol: *Raman spectra of misoriented bilayer graphene*, Physical Review B 78 (2008), 113407. Cited on p. 114
- [172] L. Malard, M. Pimenta, G. Dresselhaus, and M. Dresselhaus: *Raman spectroscopy in graphene*, Physics Reports 473 (2009), 51–87. Cited on pp. 114 and 116
- [173] J.-B. Wu, M.-L. Lin, X. Cong, H.-N. Liu, and P.-H. Tan: *Raman spectroscopy of graphene-based materials and its applications in related devices*, Chemical Society Reviews 47 (2018), 1822–1873. Cited on p. 114
- [174] A. Jorio, L. G. Cançado, and L. M. Malard: *Vibrations in Graphene in 2D Materials*, 2017, 71–89, Cambridge University Press. Cited on p. 115
- [175] L. G. Cançado, K. Takai, T. Enoki, M. Endo, Y. A. Kim, H. Mizusaki, A. Jorio, L. N. Coelho, R. Magalhães-Paniago, and M. A. Pimenta: *General equation for the determination of the crystallite size L_a of nanographite by Raman spectroscopy*, Applied Physics Letters 88 (2006), 163106. Cited on p. 115
- [176] M. Bernal, M. Tortello, S. Colonna, G. Saracco, and A. Fina: *Thermally and Electrically Conductive Nanopapers from Reduced Graphene Oxide: Effect of Nanoflakes Thermal Annealing on the Film Structure and Properties*, Nanomaterials 7 (2017), 428. Cited on p. 115

- [177] L. Cançado, K. Takai, T. Enoki, M. Endo, Y. Kim, H. Mizusaki, N. Speziali, A. Jorio, and M. Pimenta: *Measuring the degree of stacking order in graphite by Raman spectroscopy*, Carbon 46 (2008), 272–275. Cited on pp. 115 and 116
- [178] H. Heuer, S. Hillmann, M. Klein, and N. Meyendorf: *Subsurface material characterization using high frequency eddy current spectroscopy*, in: K. J. Peters, W. Ecke, and T. E. Matikas (Eds.), *Smart Sensor Phenomena, Technology, Networks, and Systems 2010*, SPIE, 2010, pp. 254 – 259. Cited on p. 118
- [179] S. A. Awan, B. Li, G. Pan, N. Jamil, and L. M. Al Taan: *Radio-frequency transport Electromagnetic Properties of chemical vapour deposition graphene from direct current to 110 MHz*, IET Circuits, Devices & Systems 9 (2015), 46–51. Cited on p. 118
- [180] S. Hillmann, M. Klein, and H. Heuer: *In-Line Thin Film Characterization Using Eddy Current Techniques*, Studies in Applied Electromagnetics and Mechanics 35 (2011), 330–338. Cited on p. 118
- [181] H. Heuer, M. Schulze, and N. Meyendorf: *Non-destructive evaluation (NDE) of composites: eddy current techniques* in *Non-Destructive Evaluation (NDE) of Polymer Matrix Composites*, 2013, 33–55, Woodhead Publishing. Cited on p. 118
- [182] J. Aprojanz, B. Dreyer, M. Wehr, J. Wiegand, J. Baringhaus, J. Koch, F. Renz, R. Sindelar, and C. Tegenkamp: *Highly anisotropic electric conductivity in PAN-based carbon nanofibers*, Journal of Physics: Condensed Matter 29 (2017), 494002. Cited on p. 124
- [183] N. Komatsu, M. Nakamura, S. Ghosh, D. Kim, H. Chen, A. Katagiri, Y. Yomogida, W. Gao, K. Yanagi, and J. Kono: *Groove-Assisted Global Spontaneous Alignment of Carbon Nanotubes in Vacuum Filtration*, Nano Letters 20 (2020), 2332–2338. Cited on p. 124
- [184] T. C. Achee, W. Sun, J. T. Hope, S. G. Quitzau, C. B. Sweeney, S. A. Shah, T. Habib, and M. J. Green: *High-yield scalable graphene nanosheet production from compressed graphite using electrochemical exfoliation*, Scientific Reports 8 (2018), 14525. Cited on p. 133
- [185] T. M. D. Alharbi, A. R. M. Alghamdi, K. Vimalanathan, and C. L. Raston: *Continuous flow photolytic reduction of graphene oxide*, Chemical Communications 55 (2019), 11438–11441. Cited on p. 133

- [186] D. Voiry, J. Yang, J. Kupferberg, R. Fullon, C. Lee, H. Y. Jeong, H. S. Shin, and M. Chhowalla: *High-quality graphene via microwave reduction of solution-exfoliated graphene oxide*, Science 353 (2016), 1413–1416. Cited on p. 133
- [187] Y. Zhao, and J. He: *Novel template-assisted microwave conversion of graphene oxide to graphene patterns: A reduction transfer mechanism*, Carbon 148 (2019), 159–163. Cited on p. 133
- [188] S. Tang, S. Jin, R. Zhang, Y. Liu, J. Wang, Z. Hu, W. Lu, S. Yang, W. Qiao, L. Ling, and M. Jin: *Effective reduction of graphene oxide via a hybrid microwave heating method by using mildly reduced graphene oxide as a susceptor*, Applied Surface Science 473 (2019), 222–229. Cited on p. 133
- [189] Y. Wang, Y. Chen, S. D. Lacey, L. Xu, H. Xie, T. Li, V. A. Danner, and L. Hu: *Reduced graphene oxide film with record-high conductivity and mobility*, Materials Today 21 (2018), 186–192. Cited on p. 133
- [190] Y. Liu, P. Li, F. Wang, W. Fang, Z. Xu, W. Gao, and C. Gao: *Rapid roll-to-roll production of graphene film using intensive Joule heating*, Carbon 155 (2019), 462–468. Cited on p. 133

List of Figures

| | | |
|--------|--|----|
| 2.1.1 | Structure of graphene | 18 |
| 2.1.2 | Electronic band structure of graphene | 20 |
| 2.1.3 | Stacked graphene layers | 21 |
| 2.1.4 | Graphite stacking | 23 |
| 2.1.5 | Carbon nanotubes | 24 |
| 2.2.1 | Graphite intercalation compounds | 26 |
| 2.2.2 | Wet-spinning of graphene fibers | 30 |
| 3.2.1 | Geometry of the analytically modeled GCM | 37 |
| 3.2.2 | GCM conductivity as a function of out-of-plane conductivity | 40 |
| 3.2.3 | GCM conductivity as a function of lateral flake size | 41 |
| 3.2.4 | GCM conductivity as a function of in-plane conductivity and packing density | 42 |
| 3.3.1 | Images of graphene flakes | 45 |
| 3.3.2 | Geometry algorithm | 46 |
| 3.3.3 | 3D geometry of a GCM | 47 |
| 3.3.4 | GCM conductivity and voltage drop from FEA | 50 |
| 3.3.5 | Comparison of FEM and the analytical model | 51 |
| 3.3.6 | Anisotropic flake orientation modeled with FEM | 52 |
| 3.3.7 | GCM conductivity for anisotropic flake orientation | 53 |
| 3.3.8 | Structural homogeneity of GCM geometries | 54 |
| 3.3.9 | GCM conductivity for different degrees of structural homo- geneity | 55 |
| 3.3.10 | Current density distribution in a GCM | 56 |
| 3.3.11 | Meshing and contacts in FEM | 58 |
| 3.3.12 | Surface current effect | 59 |
| 3.3.13 | Buffer layer between graphene flakes | 60 |
| 3.3.14 | Effect of buffer layers on GCM conductivity | 61 |
| 3.4.1 | Network generation | 65 |
| 3.4.2 | In-plane conductance trapezoid | 66 |

| | | |
|--------|--|-----|
| 3.4.3 | Current injection and voltage measurement in the network model | 69 |
| 3.4.4 | Evaluation of the conductivity limit | 70 |
| 3.4.5 | Empirical parameter k as a function of packing density . . . | 71 |
| 3.4.6 | Run-time analysis | 73 |
| 3.4.7 | GCM conductivity curves computed with the network model | 75 |
| 3.4.8 | GCM conductivity for statistically varying in- and out-of-plane conductivities | 78 |
| 3.4.9 | GCM conductivity when non-conductive flakes are incorporated | 79 |
| 3.4.10 | Comparison of literature values and simulated conductivities as a function of flake size | 83 |
| 3.4.11 | Out-of-plane conductivities and flake sizes found in the literature | 85 |
| 3.4.12 | Current propagation in GCMs with top contacts | 86 |
| 3.4.13 | Simulated 2D/3D transition in a four-point measurement of a GCM | 89 |
| 3.4.14 | Total conductivities of GCMs produced from different base materials | 92 |
| 4.2.1 | Process flow for graphene film synthesis | 100 |
| 4.2.2 | Liquid cascade centrifugation | 102 |
| 4.2.3 | Graphene visualization | 103 |
| 4.2.4 | Flake sizes obtained from liquid cascade centrifugation . . . | 104 |
| 4.2.5 | Blade coating | 105 |
| 4.2.6 | Vacuum filtration | 106 |
| 4.2.7 | Effects of HI-treatment | 108 |
| 4.2.8 | Film morphology after heating and after pressing | 110 |
| 4.2.9 | Effects of mechanical pressing | 112 |
| 4.3.1 | SEM micrographs of graphene films | 113 |
| 4.3.2 | Raman spectroscopy | 114 |
| 4.3.3 | Electrical conductivity measurement | 117 |
| 4.3.4 | Conductivity of GO/graphene mixtures and efficacy of HI-treatment | 120 |
| 4.3.5 | Conductivities of graphene films after post-treatment | 122 |
| 4.3.6 | Measurement of the TCR | 123 |
| 4.4.1 | Conductivity of graphene films as a function of mean flake size compared to the simulation | 125 |
| 4.4.2 | Graphene film conductivity as a function of the share of non-conducting flakes | 127 |

| | | |
|-------|--|-----|
| 6.1.1 | Overview of variable dimensions and parameters | 135 |
| 6.1.2 | Variation of GCM width | 136 |
| 6.1.3 | Variation of GCM length | 136 |
| 6.1.4 | Variation of the GCM layer number | 137 |
| 6.2.1 | Different simulated flake size distributions | 138 |
| 6.4.1 | Schematics of collinear four-point probe setup for the derivation of R_{2D} and R_{3D} | 140 |

List of Tables

| | | |
|------|--|-----|
| 2.1 | Overview of important properties of GCMs and selected metals | 33 |
| 3.1 | Comparison of literature values and simulated conductivities | 81 |
| 3.2 | Relation of layer number, flake diameter, and in-plane conductivity for an exemplary study | 91 |
| 4.1 | Raman data | 115 |
| 4.2 | Highest electrical conductivities | 119 |
| 6.1 | Meshing parameters | 139 |
| 6.2 | Solver settings | 139 |
| 6.3 | Dispersion parameters | 143 |
| 6.4 | Fitting parameters for the comparison of simulation and experiment | 144 |
| 6.5 | Preparation protocol “SEM” | 146 |
| 6.6 | Preparation protocol “Raman” | 146 |
| 6.7 | Preparation protocol “Best Sixonia films” | 147 |
| 6.8 | Preparation protocol “Best Graphenea films” | 147 |
| 6.9 | Preparation protocol “Best Gaoxitech films” | 148 |
| 6.10 | Preparation protocol “Best Ossila films” | 148 |
| 6.11 | Preparation protocol “Best Sigma-Aldrich films” | 148 |
| 6.12 | Preparation protocol “Best TimesNano films” | 148 |
| 6.13 | Preparation protocol “GO-portion” | 149 |
| 6.14 | Preparation protocol “HI-treatment” | 149 |
| 6.15 | Preparation protocol “TCR” | 150 |
| 6.16 | Preparation protocol “Compare Simulation and Experiment” | 150 |

Versicherung

Hiermit versichere ich, dass ich die vorliegende Arbeit ohne unzulässige Hilfe Dritter und ohne Benutzung anderer als der angegebenen Hilfsmittel angefertigt habe; die aus fremden Quellen direkt oder indirekt übernommenen Gedanken sind als solche kenntlich gemacht.

Bei der Auswahl und Auswertung des Materials sowie bei der Herstellung des Manuskripts habe ich Unterstützungsleistungen von folgenden Personen erhalten:

- keine -

Weitere Personen waren an der Abfassung der vorliegenden Arbeit nicht beteiligt. Die Hilfe eines Promotionsberaters habe ich nicht in Anspruch genommen. Weitere Personen haben von mir keine geldwerten Leistungen für Arbeiten erhalten, die im Zusammenhang mit dem Inhalt der vorgelegten Dissertation stehen.

Die Arbeit wurde bisher weder im Inland noch im Ausland in gleicher oder ähnlicher Form einer anderen Prüfungsbehörde vorgelegt.

Ort, Datum

Unterschrift

Theses

of the dissertation

Graphene-Based Conductor Materials: Assessment of the Electrical Conductivity

for the attainment of the title “Dr.-Ing.” at Technische Universität Chemnitz,
Faculty of Electrical Engineering and Information Technology

presented by M.Sc. Leo Rizzi
Chemnitz, 2020

1. Graphene-based conductor materials (GCMs) have the potential to replace metals in conductor applications. They are produced from the inexpensive and readily available raw material graphite. GCMs combine desirable thermal and mechanical properties, but the macroscopic electrical conductivity needs to be improved for the material to be competitive. The potential of GCMs can be exploited through systematic material optimization.
2. The macroscopic electrical conductivity of a GCM is a function of the average graphene flake size, the in-plane and out-of-plane conductivities of the individual flakes, the overall packing density, and the structural homogeneity of the macro-material.
3. The most suitable simulation method for GCM conductivity modeling is a random resistor network approach. It requires an initial calibration with the finite element method and can subsequently model large systems efficiently.
4. The graphene flake out-of-plane conductivity and the flake size can fully compensate each other regarding the effect on GCM conductivity. Increasing the average lateral flake dimensions in a GCM by a factor f has the same effect as increasing the average out-of-plane conductivity by the factor f^2 and vice versa.
5. The theoretical upper limit of the GCM conductivity is given by the product of the packing density and the graphene flake in-plane conductivity. Structural inhomogeneities can reduce this limit.
6. Highly conductive flake-to-flake connections dominate the out-of-plane transport. Consequently, wide statistical distributions of the graphene flake out-of-plane conductivity benefit the GCM conductivity.
7. The statistical distribution of graphene flake in-plane conductivities always decreases the GCM conductivity. The wider the distribution of in-plane conductivities, the lower the GCM conductivity.

8. The conductivity of a GCM drops significantly when 10% or more of the constituent building blocks are non-conductive.
9. Statistical distributions of graphene flake sizes have a negligible effect on the GCM conductivity. The average flake size is decisive.
10. Randomly shaped and oriented graphene flakes can form a GCM that achieves the theoretical upper limit of the conductivity if the flakes are spatially homogeneously distributed.
11. If graphene flakes are arranged with their long edges in the current direction, the GCM conductivity increases. If the short edges are in line with the current direction, the GCM conductivity decreases.
12. The network model can be easily extended to include multiphysical phenomena, different material building blocks, or various contacting scenarios.
13. Thin films are a suitable test system for the study of GCM structure-property relations. They can be prepared quickly and cost-efficiently based on graphene or graphene oxide (GO) flakes in a liquid dispersion.
14. The highest thin-film conductivity in this work, 0.55 MSm^{-1} , is achieved with a mixture of 80% GO and 20% graphene as base materials.
15. GO flakes offer the advantage of a high monolayer share, stability in water, and large flake sizes, but they require reduction and defect-healing to achieve the maximum electrical conductivity. Graphene flakes feature smaller flake sizes and agglomerate in water over time, but produce a conductive macro-material without a reduction step.
16. With a proper reduction and a defect healing process, GO forms more conductive GCMs than graphene. In absence of sufficient defect healing, graphene flakes outperform GO, even after GO reduction.
17. Hydriodic acid (HI) is an effective reducing agent for GO. It further acts as a dopant by incorporating iodine in a GCM.
18. Thermal reduction is a viable alternative to chemical reduction with HI. When high-temperature thermal treatment is performed, a previous treatment with HI is ineffective.
19. Apart from the graphene flake in-plane conductivity, the material parameters of GCMs are sufficiently developed for the material to outperform metals. GCMs will be competitive when an air-stable dopant is identified that can sustain elevated temperatures and preserve the favorable mechanical properties of a GCM, while bringing the conductivity to metallic levels.

Curriculum vitae

Name: Leo Rizzi
Date of birth: September 14, 1991
Place of birth: Solingen, Germany
Nationality: German
Marital status: Married, one child

Professional experience

since Development engineer MEMS technology
03/2020 at Robert Bosch Automotive Electronics,
 Reutlingen, Germany
03/2017 - Robert Bosch PhD program:
02/2020 Associate at Bosch Corporate Research in Renningen,
 PhD student at Chemnitz University of Technology

Academic education

10/2014 - M.Sc. Physics at RWTH Aachen University
9/2016 Final grade: 1.0
 Master's thesis: "Towards reconfigurable contacts based on
 Graphene/Silicon heterostructures"
10/2011 - B.Sc. Physics at RWTH Aachen University
9/2014 Final grade: 1.3
 Bachelor's thesis: "Local photo-induced doping of graphene-
 hBN heterostructures"

Alternative civilian service

08/2010 - Development aid in Thiès, Senegal
7/2011 Förderverein Freundschaft mit Thiès im Senegal e.V.

School education

08/2001 - Abitur, Gymnasium Schwertstraße Solingen
6/2010 Grade: 1.0

List of publications

The following publications have been authored or coauthored by Leo Rizzi during the course of this thesis.

Peer-reviewed journal publications

1. L. Rizzi, A. Zienert, J. Schuster, M. Köhne, and S. E. Schulz: *Electrical Conductivity Modeling of Graphene-based Conductor Materials*, ACS Applied Materials & Interfaces 10 (2018), 43088–4309
2. L. Rizzi, A. Zienert, J. Schuster, M. Köhne, and S. E. Schulz: *Computationally efficient simulation method for conductivity modeling of 2D-based conductors*, Computational Materials Science 161 (2019), 364–370

Contributions to conferences

1. L. Rizzi, A. Zienert, J. Schuster, and M. Köhne: *Resistor network simulation method for graphene-based conductive fibers*, Joint meeting of the DPG and EPS Condensed Matter Divisions, Talk, Berlin, 11-16 March 2018
2. L. Rizzi, A. Zienert, J. Schuster, M. Köhne, and S. E. Schulz: *Efficient resistor network simulation method for graphene-based conductor materials*, Graphene Conference, Poster presentation, Dresden, 26-29 June 2018
3. L. Rizzi, A. Zienert, J. Schuster, M. Köhne, and S. E. Schulz: *Modeling of Graphene-Based Conductors*, 20th International Conference on the Science and Application of Nanotubes and Low-Dimensional Materials, Poster presentation, Würzburg, 26-29 July 2019

Danksagung

Diese Arbeit entstand im Rahmen einer Kooperation zwischen dem Zentrum für Mikrotechnologien (ZfM) der TU Chemnitz, dem Fraunhofer ENAS und der Robert Bosch GmbH. Ich bedanke mich bei allen Menschen, die zum Gelingen dieser Arbeit beigetragen haben. Dabei gilt mein besonderer Dank den folgenden Personen:

Herrn Prof. Dr. Stefan E. Schulz für die wissenschaftliche Betreuung und die Begutachtung dieser Arbeit sowie für die Möglichkeit, in der Simulationsgruppe der Abteilung BEoL des Fraunhofer ENAS zu arbeiten.

Herrn Prof. Dr. Christoph Tegenkamp für die Übernahme des Zweitgutachtens.

Herrn Dr. Jörg Schuster für die angenehme Arbeitsatmosphäre in der Simulationsgruppe des Fraunhofer ENAS sowie die organisatorische Unterstützung während meiner Zeit als Doktorand an der TU Chemnitz. Vielen Dank für unzählige fachliche Diskussionen, das Korrekturlesen meiner Manuskripte sowie für die vielen kulturellen, kulinarischen und sonstigen Tipps & Tricks für einen Neuankömmling in Chemnitz und an der TU.

Herrn Dr. Andreas Zienert, Herrn Dr. Fabian Teichert und der gesamten Simulationsgruppe des Fraunhofer ENAS für regelmäßige fachliche Diskussionen, Anregungen und kritische Fragen zu meiner Arbeit.

Herrn M. Sc. Erik E. Lorenz für die Unterstützung mit dem Rechen-Cluster und die stets beeindruckend schnelle Beseitigung technischer Probleme.

Herrn Dr. Sascha Hermann und Herrn Martin Hartmann für den Austausch zu Graphenfilmen und für die Messungen des temperaturabhängigen elektrischen Widerstands meiner Proben.

Den Ko-Autoren meiner Veröffentlichungen Prof. Dr. Stefan E. Schulz, Dr. Jörg Schuster, Dr. Andreas Zienert und Dipl.-Ing. Martin Köhne für die Zusammenarbeit und das Korrekturlesen der Manuskripte.

Fabian und Erik für das humorvolle Miteinander, die Trainingseinheiten in der Boulderlounge und die Konzertbesuche in der Philharmonie.

Herrn Dr. Jürgen Rapp und Herrn Dr. Witold Pieper für die Möglichkeit, als Doktorand in der ARM3 zu arbeiten, für exzellente Arbeitsbedingungen und tatkräftige organisatorische Unterstützung.

Herrn Martin Köhne für die Betreuung meiner Arbeit seitens der Robert Bosch GmbH. Vielen Dank für den kollegialen Umgang, den regelmäßigen fachlichen und persönlichen Austausch sowie die Berücksichtigung meiner Arbeit im Projekt.

Meinen Praktikanten Amaliya Fardiyani Wijaya und Logeshwaran Vellingiramy Palanisamy, die hoch motiviert und durch clevere Laborarbeit zu dieser Arbeit beigetragen haben.

Herrn Torsten Reinhardt und Frau Lisa Wilke für die stets schnelle und unkomplizierte Unterstützung bei Elektronenmikroskopie und Ramanspektroskopie.

Den Doktoranden, die sich im Bosch Doktoranden-Programm engagieren, sich für unsere Arbeitsbedingungen einsetzen und ein starkes Netzwerk bilden. Insbesondere vielen Dank an Uli, Senja, Jonas, Tobi und Andreas für die gemeinsam verbrachte Freizeit.

Meinen Freunden danke ich für echte Freundschaft, zu jeder Zeit und ungeachtet räumlicher Distanzen.

Meinen Eltern und meiner Schwester, die großartige Voraussetzungen für meinen Lebensweg geschaffen haben, danke ich für die konsequente Unterstützung all meiner persönlichen und beruflichen Vorhaben.

Besonderer Dank gilt meiner Frau, die mich mehr als einmal zu meinem Glück gezwungen hat, für liebevolle Hilfe und kluge Beratung in den wichtigen Fragen des Lebens.